

Effect of mining and geology on induced seismicity – A case study

Heba Khalil

Department of Mining and Materials Engineering

McGill University, Montreal, QC, Canada



April 2023

Thesis submitted to McGill University in partial fulfillment of the requirements of the degree of

Master of Science

© Heba Khalil 2023

Abstract

High in-situ stresses are expected to induce stronger micro-seismicity as mining production advances to deeper levels. Strong seismic events could cause rockmass and support system damage in drifts and stopes resulting in production delays. Mining-induced seismicity is influenced by a wide range of mining and geology parameters, most notably, stope dimensions, mining sequence, production rate, and geological structures in the vicinity of the work areas. Analyzing the root causes of strong seismic activities can help better understand the influences of such parameters. It could also prove useful for mine planning to mitigate the occurrence of strong seismic events and to provide a safer work environment.

This thesis reports the results of a case study of Young-Davidson (YD) mine of Alamos Gold Inc. in northern Ontario, a gold mining operation using sublevel stoping method. The goal of the research is to conduct a comprehensive study of the microseismic database to discern the root causes of large micro-seismic events. Seismic events of magnitude $M_n 2.0+$ have been observed at mining depths of only 600 m to 800 m below surface, while strong seismic activities are normally expected to be associated with deep excavations. The occurrence of such large events at shallow depth is the key issue of the first part of the study. Statistical methods are utilized to analyze seismic data and relate it to mining activity. Variation in b-value, derived from the microseismic event magnitude-frequency distribution, is used to identify the rock unstable zones. It is used to differentiate between high and low stress zones and to examine the effect of geological structures, specifically the diabase dykes in the mining area. Furthermore, moment tensor inversion is carried out with MATLAB to analyze micro-seismicity, discern the mechanisms of rock failure.

In the second part of the study, analysis of seismic events of magnitude $M_n 2.0+$, that were observed in the lower-mine zone, is conducted. Moment tensor inversion of these large events is carried out to identify the rock failure mechanisms using ESG HSS-Advanced seismic analysis software. In-situ stress measurements previously conducted at the YD mine are analyzed and used to generate a 3D numerical model with finite difference software FLAC3D taking into consideration the intersecting dykes. Mine-wide modelling aims to simulate mining-induced stress distribution per the mine plan of primary and secondary stope extraction sequence. Assessment of

stress distribution, brittle shear ratio, and strain energy, as well as comparison with seismic source location, magnitude, and mechanism are discussed. Although the findings from this study are specific to the YD mine, they can also be used to elucidate the causes of seismicity in other mines with similar conditions.

Résumé

On s'attend à ce que des contraintes élevées in situ induisent une micro-sismicité plus forte à mesure que la production minière progresse vers des niveaux plus profonds. De forts événements sismiques pourraient causer des dommages à la masse rocheuse et au système de soutènement dans les galeries et les chantiers, entraînant des retards de production. La sismicité induite par l'exploitation minière est influencée par un large éventail de paramètres miniers et géologiques, notamment les dimensions des chantiers, la séquence d'exploitation, le taux de production et les structures géologiques à proximité des zones de travail. L'analyse des causes profondes des fortes activités sismiques peut aider à mieux comprendre les influences de ces paramètres. Il pourrait également s'avérer utile pour la planification minière afin d'atténuer la survenue d'événements sismiques forts et de fournir un environnement de travail plus sûr.

Cette thèse rapporte les résultats d'une étude de cas de la mine Young-Davidson (YD) d'Alamos Gold Inc. dans le nord de l'Ontario, une opération minière aurifère utilisant la méthode d'abattage par sous-niveaux. L'objectif du projet est de mener une étude approfondie de la base de données microsismique pour discerner les causes profondes des grands événements microsismiques. Des événements sismiques de magnitude $M_n 2,0+$ ont été observés à des profondeurs d'extraction de seulement 600 m à 800 m sous la surface. L'occurrence d'événements aussi importants à faible profondeur est la question clé de la première partie de ce projet de recherche. Des méthodes statistiques sont utilisées pour analyser les données sismiques de la mine YD et les relier à l'activité minière. La variation de la valeur b , dérivée de la distribution magnitude-fréquence des événements microsismiques, a été utilisée pour identifier les zones instables de la roche. Elle est utilisée pour différencier les zones de contraintes élevées et faibles et pour examiner l'effet des structures géologiques, en particulier les dykes de diabase dans la zone minière. De plus, une inversion du tenseur des moments est réalisée avec MATLAB pour analyser la micro-sismicité et discerner les mécanismes de rupture de la roche.

Dans la deuxième partie de cette étude, la zone minière plus profonde, des événements sismiques de magnitude $M_n 2,0+$ ont également été observés. L'inversion du tenseur des moments de ces grands événements est effectuée pour identifier les mécanismes de rupture de la roche à l'aide du logiciel d'analyse sismique HSS-Advanced. Les mesures de contraintes in-situ précédemment

effectuées à la mine YD sont analysées et utilisées pour générer un modèle numérique 3D avec le logiciel de différences finies FLAC3D en tenant compte des structures géologiques. La modélisation à l'échelle de la mine vise à simuler la distribution des contraintes induites par l'exploitation minière selon le plan minier d'extraction des chantiers primaires et secondaires. L'évaluation de la distribution des contraintes, du rapport de cisaillement fragile et de l'énergie de déformation, ainsi que la comparaison avec l'emplacement, la magnitude et le mécanisme de la source sismique sont discutées. Bien que les résultats de cette étude soient spécifiques à la mine YD, ils peuvent également être utilisés pour élucider les causes de la sismicité dans d'autres mines présentant des conditions similaires.

Acknowledgment

I would like to express my deepest appreciation to my supervisor Professor Hani Mitri for his invaluable support. I could not have done that work without his professional guidance and continuous encouragement. His immense knowledge and great experience have supported me all the time during my study at McGill. I am deeply indebted to him for giving me the chance to be engaged in the mining industry.

The thesis is financially supported by research grants from the Natural Sciences and Engineering Research Council of Canada (NSERC) and Alamos Gold Inc. through MITACS. Their support is gratefully acknowledged. I would like to extend my sincere thanks to Young-Davidson Mine of Alamos Gold Inc. most notably Travis Blake, Jacob Francoeur, Linas Jankunas, and Yu-Hang Xu for their time devoted to this project, and for providing the data, reports, and receiving us for site visits. It was a pleasure to collaborate with them through the MITACS project.

I am also grateful to all my colleagues in the Mine Design Lab, Isaac Vennes, Yizhuo Li, Kelly Habib, Elif Yapici Tanyeri and Dr. Shahe Shnorhokian, for their help and moral support. I must express my gratitude to Tuo Chen for his guidance, support, and motivation. His support remains crucial on any given day working on the project.

Finally, I dedicate this thesis to my family for providing me with unfailing support, care, patience, and encouragement throughout every step in my life. I am forever grateful to them, especially my husband, Mina for his love, understanding, and relentless support during my study. Special thanks are due to my lovely children Bavly and Marina; the time I spent working on the project really belonged to them.

Contributions of Authors

Chapters 1, 2, 4, and 5 are contributions of the author in their entirety. Chapter 3 is a jointly published journal paper of which the thesis author is the first author.

- Khalil, H., Chen, T., Xu, Y. H., & Mitri, H. (2022). Effect of mining and geology on mining-induced seismicity—A case study. *Journal of Sustainable Mining*, 21(3), 200-215.

The specific contributions of each co-author to the abovementioned paper are as follows.

- Khalil: Conceptualization, methodology, analysis, visualization, and production of the first draft.
- Chen: Data collection from the mine.
- Xu: Review for confidential information and publication release from the perspective of the industry partner.
- Mitri: Supervision, funding, final review

Table of Contents

Abstract	I
Résumé.....	III
Acknowledgment.....	V
Contributions of Authors.....	VI
Table of Contents.....	VII
List of Figures.....	X
List of Tables.....	XIV
List of Abbreviations.....	XV
Chapter 1 - Introduction.....	1
1.1 Mining Induced seismicity.....	1
1.2 Scope and objectives.....	2
1.3 Thesis outline	3
Chapter 2 - Literature review.....	4
2.1 Introduction	4
2.2 Rock burst mechanisms.....	6
2.2.1 Modes of fracture propagation	6
2.2.2 Rockburst classification	7
2.3 Monitoring of microseismicity.....	9
2.3.1 Microseismic monitoring systems.....	10
2.4 Seismic source parameters.....	13
2.4.1 Event Location	13
2.4.2 Event Time	14
2.4.3 Radiated energy.....	14
2.4.4 Seismic moment.....	15
2.5 Manipulation of Independent Source Parameters to analyze microseismicity.....	15
2.5.1 Moment magnitude.....	15
2.5.1.1 Magnitude general form	15
2.5.1.2 Richter scale.....	16
2.5.1.3 Moment magnitude scale.....	17
2.5.2 Frequency-Magnitude Relation.....	18
2.5.3 Magnitude-Time History Charts	21
2.6 Moment tensor decomposition and solution	22
2.6.1 First motion analysis.....	23
2.6.2 Moment tensor inversion.....	24

2.6.3	Moment tensor decomposition.....	26
2.6.4	Physical characteristics of the decomposition	29
2.7	Summary.....	30
	Bridging text between manuscripts.....	31
	Chapter 3 - Effect of Mining and Geology on Mining-Induced Seismicity – A Case Study.....	33
3.1.	Introduction.....	33
3.2.	Microseismic analysis in underground mines	35
3.2.1	Frequency-magnitude distribution.....	35
3.2.2	Moment tensor decomposition and solution.....	36
3.3.	Case study - Young-Davidson Mine.....	39
3.3.1	Mine location	39
3.3.2	Mine geology	40
3.3.3	Site ESG seismicity monitoring system.....	40
3.3.4	YD large events.....	42
3.4.	Correlation between induced seismicity and mining production rate	43
3.5.	b-value analysis	44
3.5.1	Variation in b-value with blasting distance from the dykes	44
3.5.2	Discussion of b-value results	44
3.6.	Moment tensor inversion	45
3.6.1	Moment tensor inversion method.....	45
3.6.2	Moment tensor inversion results	46
3.7.	Effect of stoping sequence on the studied seismicity.....	49
3.8.	Conclusions.....	50
	Bridging text between manuscripts.....	57
	Chapter 4 – Analysis of Seismicity in Lower Mine Zone.....	60
4.1	Introduction.....	60
4.2	Numerical modelling.....	60
4.3.1	Methodology.....	60
4.3.2	Mining Sequence.....	62
4.3.3	Rockmass properties	63
4.3.4	In-situ Stress	65
4.3.5	Results and Discussion.....	68
4.2.5.1	Maximum compressive stress	69
4.2.5.2	Brittle shear ratio	71
4.2.5.3	Burst Potential Index.....	74
4.2.5.4	Correlation between induced seismicity and instability indicators.....	77

4.3	Moment tensor inversion	79
4.3.1	Methodology.....	80
4.3.2	Results and discussion	81
4.4	Conclusion	83
Chapter 5 – Conclusion.....		86
5.1	Summary of conclusions.....	86
5.2	Suggestions for future research.....	89
References.....		90
Appendix A.....		106
A.1	Magnitude measures at YD mine.....	106
A.2	3DVM of Young Davidson mine.....	106
A.3	Seismic moment and seismic energy	106
A.4	Analysis of b-value	107
A.5	Moment tensor inversion	109

List of Figures

Figure 2-1. An example for mine development from a deep Canadian mine that employs open stope mining method. A single production stope, divided into two blast volumes, and two mine development drifts connected by a raise (Brown and Hudyma, 2017).....	4
Figure 2-2. Spalling driven by stress raisers in the corner of an excavation (Moss and Kaiser, 2021).	5
Figure 2-3. An example of shearing along structure generating seismic damage (Heal et al., 2006).	5
Figure 2-4. Three modes of fracture propagation (modified from Gibowicz and Kijko, 1994).	6
Figure 2-5. Schematic diagram of six possible ways in which mine-induced tremors can occur. Solid arrows indicate mining-induced force directions on host rock during induced seismic event. Dashed arrows in part (e) denote ambient tectonic stress directions (after Horner and Hasegawa, 1978).....	7
Figure 2-6. Typical local rockmass failure mechanisms that potentially cause seismic events: (a) fault movement; (b) stress change causing rockmass fracturing near excavations; (c) stope overbreak; (d) contrast in rockmass material properties causing strain-bursting; (e) crushing of mine pillars; and (f) stress increase causing rockmass deformation (Hudyma, 2008).....	9
Figure 2-7. Frequency bandwidth covered by different types of sensors (Urbancic et al., 2013).....	11
Figure 2-8. General schematic showing typical data flow for a network of Paladin stations (Hudyma et al., 2010).	12
Figure 2-9. A typical Gutenberg-Richter frequency-magnitude relation for a large population of data (Hudyma, 2008).	18
Figure 2-10. Frequency distribution with moment magnitude of seismic events at (a) Creighton and (b) Kidd Mine sites. According to the maximum frequency windows of magnitude, the magnitude of completeness at Creighton Mine should exceed -1.6 and for Kidd Mine, it should be larger than -1.9 (Ma et al., 2018).	19
Figure 2-11. Magnitude-Time History chart for a group of seismic events at Mount Charlotte mine. The black line at the top represents the blasting period. It is obvious the increase of the event rate with mining activity. However, numerous events occurred before blasting start (Hudyma, 2008).	22
Figure 2-12. The system of force couples representing the components of a Cartesian moment tensor. Diagonal elements represent linear vector dipoles, while off diagonal elements represent force couples with moment (Dahm and Krüger, 2014).	23
Figure 2-13. First motion analysis for focal mechanism solution (FMS) (after Stein and Wyssession, 2009).	24
Figure 2-14. Graphical representation of the positive (explosion) and negative (implosion) meaning of the isotropic component (after Eaton, 2008).	28

Figure 2-15. Graphical representation of a mixed source event (pillar burst under compression) has Iso and CLVD components (after Eaton, 2008).	28
Figure 2-16. Example of moment tensor decomposition (Krieger and Heimann, 2012).	29
Figure B1-1. Magnitude-Time chart of YD large seismic events recorded by the CNSN from April 2018 to March 2021 (Alamos Gold Inc., 2021). 32	
Figure B1-2. <i>Mw</i> 2.0+ events recorded by ESG system in YD mine in 2020 and 2021 with respect to YD mine layout in section view.	32
Figure B1-3. <i>Mw</i> 1.0+ seismic events recorded by ESC monitoring network at YD mine in 2020 with the calculated source parameters in the microseismic system.....	32
Figure 3-1. Frequency-magnitude charts for two different groups of events [18].	36
Figure 3-2. First motion analysis. (a) Beach ball diagram of strike-slip faulting with two auxiliary planes. (b) Direction of the first motion at the instant of the event. (c) P-wave polarity (after [23]).	37
Figure 3-3. Hudson chart (after [37]).	39
Figure 3-4. Location map of Young-Davidson Mine.	40
Figure 3-5. Local geology of the Young-Davidson Property [38].	41
Figure 3-6. Three main geological domains in YD mine: Timiskaming sediments (host rock), diabase and syenite (ore) [39].	41
Figure 3-7. Relation between mining production rate and recorded seismicity throughout 2020. (a) Total blasting volume. (b) Accumulated seismic moment. (c) Accumulated seismic energy.....	43
Figure 3-8. Plan view of level 9470 showing four largest events in 2020 between levels 9400 and 9600. 44	
Figure 3-9. b-value results. (a) West of dyke A. (b) East of dyke B. (c) Between dyke A and dyke B.	45
Figure 3-10. Generated beachballs from focal mechanism solution of the event (1). (a) DC component. (b) Deviatoric component. (c) Full tensor.	47
Figure 3-11. Generated beachballs from the focal mechanism solution of the event (2). (a) DC component. (b) Deviatoric component. (c) Full tensor.	48
Figure 3-12. Generated beachballs from focal mechanism solution of the event (4). (a) DC component. (b) Deviatoric component. (c) Full tensor.	48
Figure 3-13. Hudson source-type plot of the three events 1, 2, and 4.	49
Figure 3-14. Planned stoping progression for the 9590 breakthrough [43].	50
Figure 3-15. Mining sequence and large seismic events through levels 9400 to 9600 between October and December 2020. Note: Orange circles represent large events. (a) October 21 to 30 [event (4)]. (b) October 30 to November 02 [event (1)]. (c) November 02 to 30. (d) November 30 to December 11 [event (2)]. ...	50
Figure B2-1. Result of the bootstrap resampling test for event (1) showing the uncertainty of the solution. (a) DC component. (b) Deviatoric component. (c) Full tensor.	58

Figure B2-2. Result of the bootstrap resampling test for event (2) showing the uncertainty of the solution. (a) DC component. (b) Deviatoric component. (c) Full tensor.....	58
Figure B2-3. Result of the bootstrap resampling test for event (4) showing the uncertainty of the solution. (a) DC component. (b) Deviatoric component. (c) Full tensor.....	58
Figure 4-1. 3D volumetric mesh generated using Griddle2.0 for FLAC3D7.0. All excavations and dykes mesh are fixed, merged, and refined with the appropriate size.....	61
Figure 4-2. FLAC3D Model Layout.	62
Figure 4-3. The general sequence in YD mine includes the three critical zones, stoping blocks below 9440, west mining zone 9590-9800, and the 9440-9590 central/eastern stoping blocks.	63
Figure 4-4. Stress conditions at YD Mine (MD Eng., 2017- b) after Hoek and Brown 1980).	67
Figure 4-5. Principal stress axes from Cadillac Fault mine database (McKinnon and Lebric, 2006).	68
Figure 4-6. In-situ stress orientation in YD mine where a) and b) represent the measurements' averaged and adjusted orientations respectively.....	68
Figure 4-7. Plan view at level 9360 including the maximum compressive stress values around excavations mined out at stages 9, 16, 22, 33, 36, 47, 51, 60, and 73.	69
Figure 4-8. Relationship between major and minor principal stresses for Hoek-Brown. The dashed line represents $\sigma_1 = \sigma_3$ (After Hoek, 1983).	70
Figure 4-9. Safety factor values around the excavations 9, 16, 22, 33, 36, 47, 51, 60, and 73.	71
Figure 4-10. BSR contours on level 9360. a) to j) Plan views show BSR values at mining stages 9, 16, 22, 33, 36, 47, 51, 60, 73, and 76 respectively. l) The mining sequence through the level and the red point X is used to monitor the change in BSR value with mining advance.....	73
Figure 4-11. Change in BSR values at point X with mining sequence between stages 9, 16, 22, 33, 36, 47, 51, 60, 73, and 76 at level 9360.....	73
Figure 4-12. BSR contours around the pillar on level 9440. a) to d) Cross sections showing BSR values at mining stages 14, 43, 56, and 78 respectively. f) The mining sequence through the pillar and the red point X is used to monitor the change in BSR value with mining sequence.	74
Figure 4-13. Change in BSR values at point X with mining sequence between stages 14, 43, 56, and 78 through the pillar at level 9440.....	74
Figure 4-14. BPI contours on level 9360. a) to j) Plan views show BPI values around excavations 9, 16, 22, 33, 36, 47, 51, 60, 73, and 76 respectively. l) The mining sequence through the level.	76
Figure 4-15. BPI contours around the pillar on level 9440. a) to d) Cross sections show BPI values around excavations 14, 43, 56, and 78 respectively. f) The mining sequence through the pillar.....	77
Figure 4-16. Seismic events of magnitude M_w 2.0+ in the lower-mine zone.	77

Figure 4-17. Instability indicators values at the locations of four large events. a) to l) Plan views show the SF, BSR, and BPI values at the location of the large events of May 06, 21, Jun. 30, 21, Jul. 18, 21, and Feb. 10, 22 respectively. m) to p) The large events locations with respect to the mining sequence and the grey star represents the last excavation before the triggered event.....79

Figure 4-18. Example of the spectral analysis graph of a selected waveform at sensor 16 recording event of Mar 03, 2021. Ω_0 represents the low-frequency displacement spectrum level, f_c is the corner frequency, and Q is the attenuation factor.81

Figure 4-19. Focal mechanism solutions' beach balls of the analyzed events, representing the ISO, DC, and CLVD tensors respectively.....82

Figure A-1. (a) Accumulated seismic moment and (b) accumulated energy in Oct 2020 at YD mine. ... 107

Figure A-2. Example of b-value estimation steps for the seismic cluster induced by a blast on Aug 29. (a) Blasting information table. (b) The induced seismic events in a two-day window following the blast of Aug 29. (c) Cluster of the microseismic events at the location of the blast. (d) Magnitude distribution graph. 108

Figure A-3. Frequency distribution with moment magnitude of seismic events at the location of the blast. 109

Figure A-4. Example of one waveform for the event Oct 21 that is converted from acceleration to displacement domain. (a) The waveform in acceleration-time domain. (b) The waveform in displacement time domain. 110

List of Tables

Table 2-1. Five mechanisms of damaging rockbursts proposed by Ortlepp (1992).....	8
Table 2-2. A qualitative relation between how an event feels in a mine and the Richter magnitude of the event (Hudyma, 2008).....	17
Table 3-1. YD large events recorded by CNSN (2018.05-2021.03) [39].	42
Table 3-2. Moment tensor decompositions and source mechanisms reported for the three events.	47
Table 3-3. Fault plane solutions for the three events and corresponding fault types.	47
Table B2-1. RMSERROR values of Dec 09, Oct 30, and Oct 21 seismic events.....	57
Table 4-1. Summary of the RQD observed at Young-Davidson, joint sets number, joint condition (Alamos Gold Inc., 2020), and the calculated Q index and GSI.....	64
Table 4-2. Summary of Rock Unit Properties (Alamos Gold Inc., 2020), and the calculated rockmass parameters using RSDData software by RocScience.	65
Table 4-3. The average rock material properties (after MDEng report, 2017).	65
Table 4-4. Stress measurements at Young-Davidson Mine (after Mine Design Engineering, 2017).....	67
Table 4-5. Level of rockmass damage based on BSR (after Castro et al., 2012).	72
Table 4-6. large events in the lower mine zone with the corresponding SF, BSR, and BPI.....	78
Table 4-7. Moment tensor decompositions and source mechanisms reported for five events of magnitude M_w 2.0+ in the lower-mine zone.	82
Table 4-8. RMSERROR and CN values of the resultant solution for the five studied events.	83
Table A-1. 3DVM of Young Davidson Mine (Alamos Gold Inc., 2020).	106
Table A-2. Number of events used to estimate b-value after each blast.	109
Table A-3. The input ASCII file of event Dec 09.	111
Table A-4. The input ASCII file of event Oct 30.	111
Table A-5. The input ASCII file of event Oct 21.	111

List of Abbreviations

BPI: Burst Potential Index

BSR: Brittle Shear Ratio

CLVD: Compensated Linear Vector Dipole component of the moment tensor

CN: Condition Number

CNSN: Canadian National Seismograph Network

DC: Double-Couple component of the moment tensor

DCDT: Diametrical Core Deformation Technique

ESG: Engineering Seismology Group

ESR: Energy Storage Rate of the rock

FLAC3D: Fast Lagrangian Analysis of Continua in 3 Dimensions

FMS: Focal Mechanism Solution

FS: Factor of Safety

GSI: Geological Strength Index

ISO: Isotropic component of the moment tensor

MT: Seismic Moment Tensor

Q-index: Rock Quality Index

RMR: Rock Mass Rating

RMS: Root Mean Square

RQD: Rock Quality Designation index

SGM: Strong Ground Motion

SMTI: Seismic Moment Tensor Inversion Package

SRF: Stress Reduction Factor

UCS: Uniaxial Compressive Strength

Chapter 1 - Introduction

1.1 Mining Induced seismicity

Fracture initiation, propagation, and rockmass movement along the pre-existing fracture planes can occur when large volumes of rock are excavated. This process is usually accompanied by the generation of seismic waves and known as mining-induced seismicity. As the demand for mineral resources is high and mining operations are digging deeper, mining-induced seismic hazards are likely to become more prevalent. Mining-induced seismicity has been recorded in underground mining and civil tunnelling projects worldwide, for nearly all underground operations and in a variety of rock types; hard brittle rocks such as granite, and soft rocks such as coal (Li et al., 2007).

Mining induced seismic events take place due to the interaction of tectonic stresses and mining-induced stresses. Those events correspond to sudden release of elastic strain energy in the rockmass and can be represented by the movements caused by sudden failure of rock masses due to stress concentration in the mining area (Zhou et al., 2011). Mining activity and ore extraction in underground mines provide a high stress environment that may lead to drastic rock failure, generally known as rockburst.

Induced seismicity can result in production delays in underground mines, equipment damage, drifts, and stopes collapse, and, in the worst-case scenario, loss of lives. It is now considered as a human-induced engineering and geological hazard (Li et al., 2007). Large seismic events with high-energy radiation can endanger the safety of the mining operation as they are the direct cause of underground rockbursts. According to Blake and Hedley (2003), a 3-magnitude seismic event could cause significant damage to the rockmass, as well as instability of underground openings, such as triggering rock falls within a 100-meter radius of the source. Strong and shallow seismic events can result in the collapse of a mine roof, which for miners working in the vicinity of the event poses a direct threat to their lives (Ilieva et al., 2020).

The risk associated with rockbursts must be investigated to ensure the safety of the workers and minimize production delays. Statistical methods for parameterizing seismic data and predicting seismic hazard have advanced significantly in the last 30 years, with encouraging results.

However, due to the complex nature of mining-induced seismicity, the prediction accuracy of high-energy seismic events is like earthquake prediction, a challenge (Si et al., 2020). Seismicity in mines is affected by depth, production rate, excavation size and geometry, geological discontinuities such as dykes, faults, and other geological features, as well as the ambient tectonic stress zone. In any given case, one or a combination of these factors may play a significant role in mining seismicity (Gibowicz and Kijko, 1994; Holub, 1997; Brown, 2018).

Significant efforts have been made in developing methods to analyze microseismicity in underground mines. Manipulations of seismic source parameters are used to get more information about seismic source and describe the resulting events. Instability indicators have been developed in order to analyze large seismicity in underground mines and understand the reasons behind them. The case study presented in this thesis adopted some of the commonly used methods to discern the root causes for the unusually strong seismic activities recorded in an underground mine.

1.2 Scope and objectives

The thesis presents a case study of Young-Davidson mine, where seismic events of magnitude M_n 2.0+ have been observed at different mining zones. The main concern of this research is the occurrence of such significant events. A comprehensive study of the microseismic database has been conducted to discern the causes for the strong seismic activities recorded at the mine. The effects of mining and geological parameters on the seismic response are considered. The research involves mining, geologic, geotechnical, and seismic data collection and analysis as well as extensive, 3D mine-wide numerical modelling studies. More specifically, the objectives of this thesis are as follows.

1. Rock mass classification and delineation of nearby geological structures.
2. Rock mass properties for orebody and host rock.
3. Characterization of geological structures.
4. Establish in-situ stress regime for mine wide FLAC3D model.
5. Analysis of seismic database.
6. Mine wide model development using FLAC3D, Rhino, and Griddle.
7. Moment tensor inversion with HSS Advanced software and MATLAB.

1.3 Thesis outline

Chapter 2 is a literature review on rockburst mechanisms and manipulation of independent source parameters to analyze microseismicity. Chapter 3 is a journal article entitled “Effect of mining and geology on mining-induced seismicity – A case study”. Analyzing the unusually strong seismic activities recorded at shallow depths in the case study mine has been discussed in this article using variation in b-value derived from the magnitude-frequency distribution and moment tensor inversion methods. Chapter 4 describes the development of a 3D mine-wide model with FLAC3D software. It aims to correlate seismicity in the lower mine zone with the output of 3D numerical modeling and moment tensor inversion methods. The conclusion of this study is reported in chapter 5 along with suggestions for future research.

Chapter 2 - Literature review

2.1 Introduction

Mining-induced seismicity can be defined as the response of the rockmass to deformations or failure of the underground structures due to stress redistribution in the mining area (Li et al., 2007). It represents the change in stress brought on by mining activities. Figure 2-1 shows an example of mine development from a deep Canadian mine that employs open stope mining method. Stope mining is the process of blasting large volumes of ore from sub-vertical panels, with each blast containing thousands of tons of ore. The production stope shown in Figure 2-1 is subdivided into two blasts. When a blast is launched, the resulting fragmented rock expands by 120 to 140 percent in volume. There is a limited space available for the expansion of the broken rock when the first blast (A) is fired, but when the fragmented rock is mucked from the stope, free space is created for the second blast to swell. The production stope is accessed by two development drifts on the top and bottom to provide access for drilling and blasting from the top and mucking the fragmented ore from the bottom. Drifts are blasted in short rounds of 3 to 4 meters per blast. Micro-seismicity in this case is the effect of stress change and opening geometry change, which depend on the blast size, due to mine development or blasting (Brown and Hudyma, 2017).

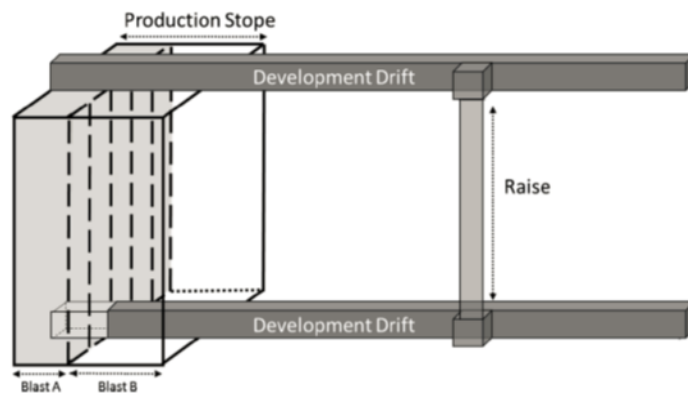


Figure 2-1. An example for mine development from a deep Canadian mine that employs open stope mining method. A single production stope, divided into two blast volumes, and two mine development drifts connected by a raise (Brown and Hudyma, 2017).

Underground mining operations create a high stress environment that could lead to violent rock failure or rockburst in drifts, ramps, or pillars. Production setbacks, equipment damage, stope collapse are all possible consequences of these induced events in underground mines. Figure 2-2 shows an example of spalling driven by stress raisers in the corner of an excavation (Moss and Kaiser, 2021). It has been observed that most of these damaging events are induced at the geological discontinuity in the mining area (Guha, 2000). Despite the varying magnitude of rockbursts with the source mechanism (Blake and Hedley, 2003), $M_L > 2.0$ rockbursts can occur when pre-existing faults are reactivated or when shear rupture spreads violently through an intact rockmass (Sainoki et al., 2016). Figure 2-3 shows an example of the shearing along a major structure which generated a seismic event resulting in severe damage to the drive (Heal et al., 2006).



Figure 2-2. Spalling driven by stress raisers in the corner of an excavation (Moss and Kaiser, 2021).



Figure 2-3. An example of shearing along structure generating seismic damage (Heal et al., 2006).

To assure the safety of mining operations and reduce production losses, the risk associated with rockbursts needs to be investigated. Many factors related to mining and geology have an impact on induced seismicity. Tracking and analyzing the underlying causes of seismic occurrences brought on by mining will help understand the impacts of these characteristics. Seismic events can be described through microseismic source parameters like the event location, time, size, radiated energy, stress drop, and moment tensor (Mendecki et al., 1999). Thus, a seismic analysis needs to start with understanding these parameters and their relation to the significant events in the work area. In this chapter, the microseismic source parameters and their relationship to different rockburst mechanisms are discussed. Manipulation of independent source parameters to analyze microseismicity in the underground mines is also covered.

2.2 Rock burst mechanisms

2.2.1 Modes of fracture propagation

Modes of fracture refer to the decomposition of crack tip stresses into three modes. Figure 2-4 shows the three main modes of fracture processes that cause microseismicity including tensile opening of a fracture, where the displacement is normal to the fracture plane, or slip on a pre-existing fracture surface. This slip may be in-plane shear, where the displacement is along the fracture plane and normal to its edge, or anti-plane shear, where the displacement is along the fracture plane but parallel to the edge (Eaton and Forouhideh, 2010). However, these modes represent ideal cases with zero fracture thickness that simulate the actual condition where microseismic events can be considered as the combination of different types of fractures.

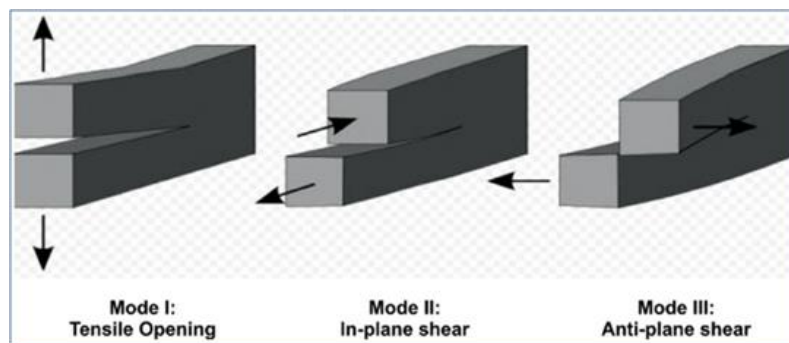


Figure 2-4. Three modes of fracture propagation (modified from Gibowicz and Kijko, 1994).

2.2.2 Rockburst classification

Hasegawa et al (1989) proposed six mechanisms for rockbursts (Figure 2-5). A cavity collapse (a) represents either a rockburst in a mine roof with violent rock mass ejection downwards, or a large mass of rock loosened by mining and possibly falling under the effect of gravity. Pillar burst (b) is due to a combination of forces related to stope face advancement (elastic) and time-dependent after-effects (inelastic process) as stress accumulating in the pillar until it bursts at certain point. Tensile failure (c) of competent rock above a mine may occur in the middle of a wide excavation where roof subsidence is maximum. However, edge dislocations and comminuted faults, which occur at the stope face and are caused by a combination of blasting and volume closure, are the most common types of fracturing and faulting (McGarr, 1971). Comminuted faults (d) are generally normal faults and occur in intact rock and are referred to as strain energy burst. Thrust faulting (e) below or above a mine could occur for the case where the maximum principal stress is horizontal and the induced stress is large enough either to initiate slip in the intact medium, or to trigger faulting along a pre-existing fault at greater depths (Smith et al., 1974). Shallow-thrust faulting (f) could occur between near-horizontal layers that become unclamped or experience shearing motion because of bending in the mine roof (Hasegawa et al., 1989).

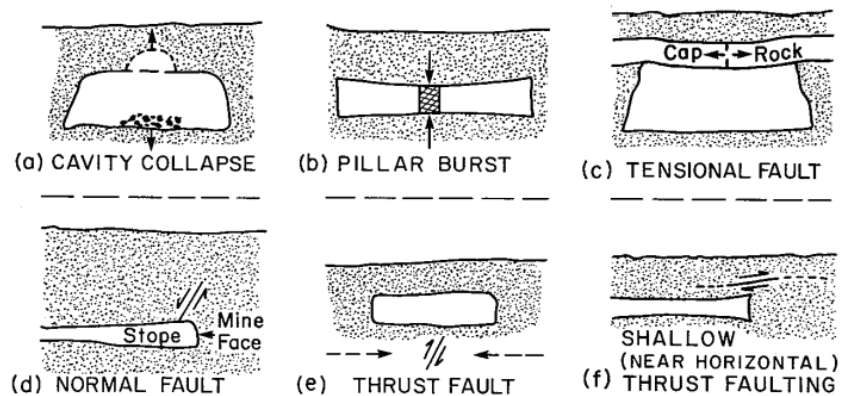


Figure 2-5. Schematic diagram of six possible ways in which mine-induced tremors can occur. Solid arrows indicate mining-induced force directions on host rock during induced seismic event. Dashed arrows in part (e) denote ambient tectonic stress directions (after Horner and Hasegawa, 1978).

Gibowicz (1990) classified rockbursts into two mechanisms. The first mechanism is induced seismicity that is directly connected to mining operations and occurs around the openings and so it is proportional to the mining scale and opening sizes. The second mechanism is triggered

seismicity which is associated with the movement along major geological discontinuities due to change in stresses after mining and it may occur at certain distance from the opening. In contrast to induced seismicity, triggered seismic events are spatially and temporally independent of mining-induced stress change. Ortlepp (1992) proposed five mechanisms in Table 2-1. They are listed in ascending order of energy output.

Table 2-1. Five mechanisms of damaging rockbursts proposed by Ortlepp (1992).

Seismic event	Postulated source mechanism	First motion from seismic records	Richter magnitude M_L
Strain-burst	Superficial spalling with violent ejection of fragments	Usually undetected, could be implosive	-0.2 to 0
Buckling	Outward expulsion of large slabs pre-existing parallel to surface of opening	Implosive	0 to 1.5
Face crush / pillar burst	Violent expulsion of rock from stope face or pillar sides	Mostly implosive, complex	1.0 to 2.5
Shear rupture	Violent propagation of shear fracture through intact rockmass	Double – couple shear	2.0 to 3.5
Fault-slip	Violent renewed movement on existing fault or dyke contact	Double – couple shear	2.5 to 5.0

In mines, there are a variety of seismic source mechanisms that may happen relatively close to each other and create seismic events. Figure 2-6 depicts a schematic open stope mining block with images of some of the most prevalent rockmass failure mechanisms. The size and nature of the seismic event at each seismic source will depend on the local rockmass failure mechanisms (fault movement, stress change, stope overbreak, contrast in rockmass material properties or crushing of mine pillars) (Hudyma, 2008). Kaiser (2009) proposed a classification summarizing the rockbursts into three main types, strainburst, fault-slip burst, and pillar burst. The most dangerous one is the fault-slip when sudden movement occurs along a fault due to change in the stress field. The second type is pillar burst when stress accumulates until it exceeds the strength in the pillar. The failure can be full for the entire pillar or partially with pillar skin peeling. The third type is strainburst when the stresses exceed strength in the walls of the opening and failed rock is ejected violently from the walls into the opening.

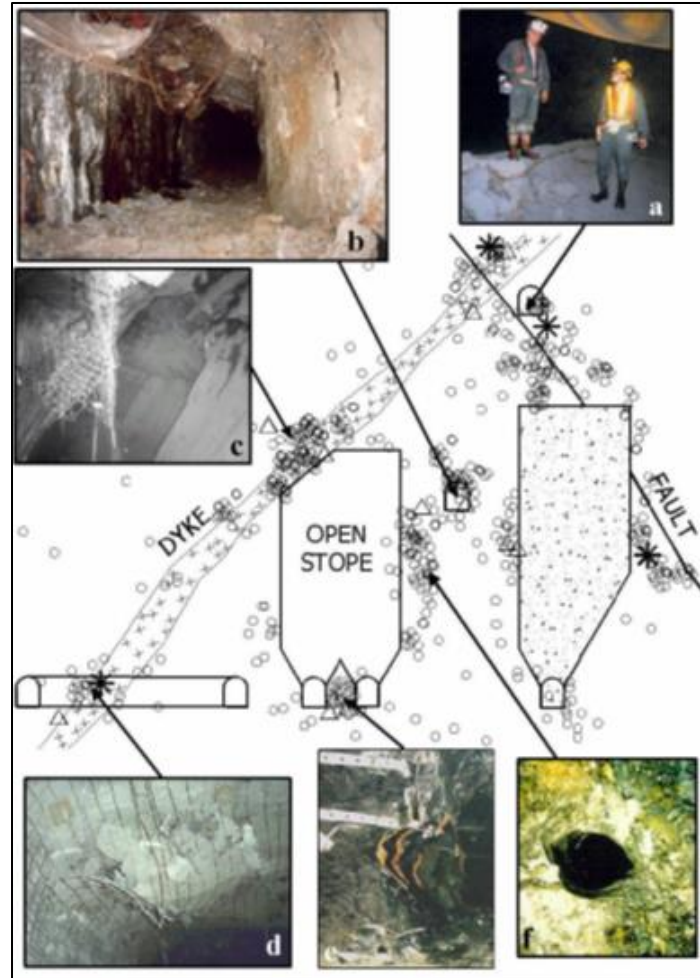


Figure 2-6. Typical local rockmass failure mechanisms that potentially cause seismic events: (a) fault movement; (b) stress change causing rockmass fracturing near excavations; (c) stope overbreak; (d) contrast in rockmass material properties causing strain-bursting; (e) crushing of mine pillars; and (f) stress increase causing rockmass deformation (Hudyma, 2008).

2.3 Monitoring of microseismicity

Brittle fracturing of rock is associated with seismic activity that can be detected using vibration monitoring systems which include networks of geophones and/or accelerometers installed in the mine (Owen et al., 2002). A microseismic event occurs when a rock under a critical state of stress cracks and releases a short-duration, low-amplitude energy wave (Ma et al., 2020). These events are too small to be felt on the ground surface, but geophones and accelerometers can detect and measure such events. As mining progresses to greater depths and at higher production rates, the intensity and frequency of the mine-induced tremors have increased. The most feasible and realistic way to detect these tremors at the present time is to deploy a network of seismometers

underground and on surface (Hasegawa et al., 1989). Information on the location, size and other characteristics of the seismic event can then be obtained for the analysis of the potential hazard. The main aim of monitoring is to track these events over time to identify trends and correlations between them and production activities as this monitoring will provide real-time results, giving insight into what's going on underground and at what time exactly (Ge, 2005). Monitoring mining-induced microseismic events is often used to indicate potential instability and changing stress conditions in underground mines and to evaluate the behavior of the surrounding rockmass, which is very important for mine safety considerations and operation (Ma et al., 2020). Understanding how mining activities disrupt in-situ conditions and how those changing conditions impact the project is critical (Leake et al., 2017).

2.3.1 Microseismic monitoring systems

Mining operations use seismic monitoring systems which are a combination of hardware and software components to detect and evaluate the seismic response to the mining activity. The main components of the seismic monitoring system are sensors that continuously record ground motion, communication networks, digitizers, analysis software, and data storage (Brown, 2018). There are four types of sensors: uniaxial and triaxial geophones and accelerometers and the arrangement of the sensor array should be chosen properly in the most effective way for better monitoring quality in terms of the sensors' density and locations. Uniaxial sensors record the ground motion in one direction, and they are cheaper and easier to install. To achieve adequate location accuracy, many uniaxial sensors are often utilized to surround the area of interest (Brown, 2018). Triaxial sensors record the ground motion in three directions. They are expensive and difficult to install, however, they provide high accuracy when calculating seismic source parameters and are essential for source mechanism analysis (Collins and Hosseini, 2013; Brown, 2018). Mine seismic arrays typically use a combination of uniaxial and triaxial sensors to obtain accurate locations and source characteristics for the recorded events (Brown, 2018).

According to Brown and Hudyma (2018) piezoelectric accelerometer is one of the most used sensors in microseismic monitoring systems in Canadian mines. Pressure from ground motion is converted into an electrical signal proportional to ground acceleration (the rate of change of velocity) (Brown, 2018). Accelerometers are more sensitive to higher frequencies than

geophones and identify efficiently the low-magnitude events as the accelerometers have a high upper frequency limit of 15,000 Hz (Collins and Hosseini, 2013; Brown, 2018). Geophones are commonly used and installed to measure ground velocity. They cover a lower frequency range relative to accelerometers (Brown, 2018).

Depending on the magnitude of a seismic event, different frequencies are generated. High frequency events have a smaller magnitude than low frequency events. The range of frequencies and magnitudes that the microseismic system can detect is determined by the type of sensor used. Figure 2-7 shows the monitoring ranges for seismic systems (Urbancic et al., 2013). The 4.5 Hz geophones are likely the strong ground motion sensors used in seismic monitoring systems (Brown, 2018).

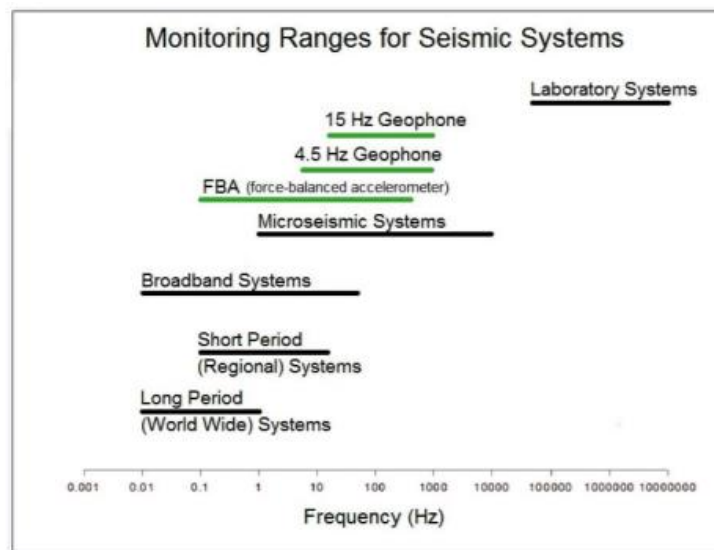


Figure 2-7. Frequency bandwidth covered by different types of sensors (Urbancic et al., 2013).

The data acquisition network is a local area network which may be wired or wireless. ESG (Engineering Seismology Group) microseismic monitoring network consists of sensors that record the ground motion due to rock mass failure and Paladin stations (digital seismic recorders) to where the electrical signal is transferred. Then, the data will be digitized and organized at the acquisition computer at a central engineering office and then real time results are analyzed using the analysis software (Figure 2-8) (Brown, 2018; Hudyma et al., 2010). Years of seismic data can be stored and archived, making back analysis easier (Brown, 2018).

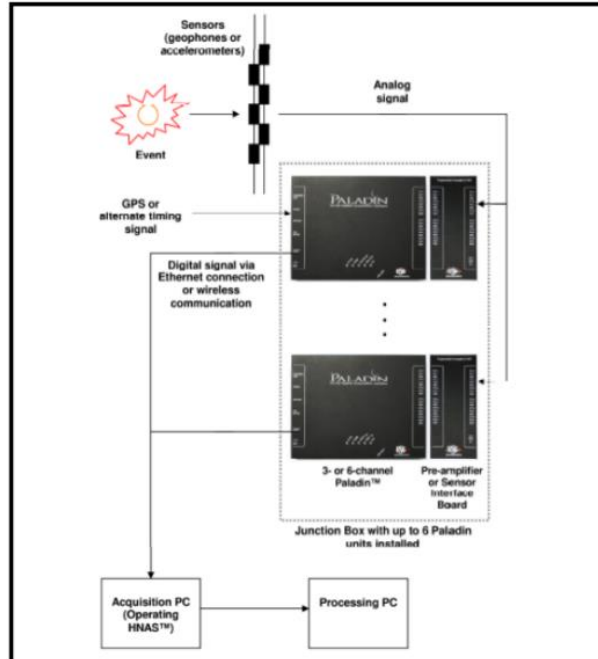


Figure 2-8. General schematic showing typical data flow for a network of Paladin stations (Hudyma et al., 2010).

The case study of this thesis is Young Davidson (YD) mine owned by Alamos Gold Inc. The mine uses the ESG seismic monitoring system which will be discussed in Section 3.3.3. To ascertain the consistency of the recorded large events magnitude, the mine uses the Canadian National Seismograph Network (CNSN) data for comparison. Appendix A lists the different relations used by YD mine to convert between magnitude measures. According to YD mine, while the local large and small seismic events can be recorded by the ESG network, it is challenging sometimes to distinguish a major occurrence from a series of smaller ones. For example, the P-wave arrivals of some small events resulting from blasting could cover up the waveforms of the large event. The CNSN is much less sensitive to blast firing small events and its accuracy is relatively constant compared to ESG monitoring system that needs to be upgraded sometimes. The downside of this procedure is the time it takes to receive the CNSN results making it difficult for the mine to make timely decisions regarding induced seismicity, which is crucial for the safety of the mining operation. For example, on December 9, 2020, a large event was recorded by the automatic processor of ESG network with a magnitude of less than 1.0 which is not large enough to trigger YD seismic re-entry protocol. A few minutes later, the event was processed by the ESG team and had a magnitude M_w of 2.03. About 30 minutes later, it was recorded as $M_n = 2.3$ by the CNSN (Alamos Gold Inc., 2021).

2.4 Seismic source parameters

Seismic source parameters derived from the recorded waveforms are used to quantitatively describe the source of a seismic event. To provide relevant description of a seismic event, the parameters including event location, time, size, radiated energy, seismic moment and moment tensor are required (Mendecki et al., 1999).

2.4.1 Event Location

Many seismic source parameters depend on the distance from the seismic source to the seismic sensors. Determining the seismic events locations with respect to active mining faces, pillars, and the geological features, can often give an idea about the source mechanism. While attempting to understand seismicity in mines, spatial representation of event locations can be very informative. Poor locations can be a problem when analyzing seismicity in mines (Hudyma, 2008). As mentioned earlier, with enough sensors in the monitoring system, very accurate source location estimation is possible.

Geiger developed the first algorithm for locating seismic events in 1910 by reducing the least-squares error between observed and theoretical P-wave travel times (Geiger, 1912). Most techniques used subsequently for locating seismic events adopted this algorithm as they attempt to minimize the time residual or the difference between the measured arrival time at the station and the theoretical arrival time. The latter is determined by using the location of the event and the wave velocity model. The difference represents an error value (in distance) for the event location (Gibowicz and Kijko, 1994; Mosher and Audet, 2020).

Event locations can be determined following point location techniques or zonal techniques. The first approach estimates the exact coordinates of the event, while the latter determines the zones of activity. Point location techniques can be classified into direct methods, such as least squares fitting of time residuals, or indirect methods, such as iterative techniques which arbitrarily test locations and converge to reach the minimum error. The main point of these techniques is to minimize the errors between the observed and calculated arrival times and converge to a solution. According to ESG User Guide, Geiger and Simplex iterative methods (Nelder and Mead 1965) are

used in the ESG Microseismic event location program. A 3-D velocity model is used for YD mine which improves the source location accuracy by 20% (16 m vs. 20 m) when locating blasts using this model instead of the traditional 1-D model (Alamos Gold Inc., 2021); refer to Appendix A for YD velocity model.

2.4.2 Event Time

The event time shows when a seismic event occurs. With the epicentral distance of the seismic event, the time needed for the seismic wave to reach the seismic station can be determined and in turn information about when the event happened can be obtained. Seismicity timing is very important in analyzing the risks associated with mining activity. For example, if large events follow closely significant blasts, creating temporary exclusion zones in the vicinity of those blasts will be a very effective way of mitigating the risk (Hudyma, 2008). Another example is given by Urbancic and Trifu (1995) who studied the seismicity at Strathcona mine where a large blast triggered immediately a large seismic event next to the opening. Then, in the following 75 hours, nine more large seismic events occurred in mine pillars up to 200 m from the mine blast. A complex combination of stress migration and the influence of mine faults were considered the main reasons for this series of large seismic events. In YD mine, analyzing the occurrence time of microseismic events with respect to mining sequence could provide insights into the causes of specific large events. This will be discussed later in the thesis.

2.4.3 Radiated energy

Seismicity generates a variety of energy forms, including kinetic energy, gravitational energy, and elastic strain energy. When seismicity occurs, the potential energy stored inside the rockmass (mainly gravitational and elastic strain energy) is released and part of it is radiated as seismic waves (Dahlen, 1977). This radiated energy represents the size of the event and can be calculated from the spectra of seismic waves as follows (Gibowicz and Kijko, 1994; Urbancic et al., 1996).

$$E_R = 4 \pi \rho C R^2 \frac{J_c}{F_c^2} \quad [2-1]$$

Where E_R is the released energy, ρ is the rock density, C is the wave velocity in rock, R is the distance from the seismic source, J_c is the integral of the square of the ground velocity, and F_c is an empirical radiation pattern coefficient.

2.4.4 Seismic moment

Seismic moment (M_o) represents the amount of energy released by an earthquake. It describes the size of the event as well, and it can be used to calculate the moment magnitude. The seismic moment can be estimated using the following equation (Gibowicz and Kijko, 1994; Urbancic et al., 1996).

$$M_o = 4 \pi \rho R C^3 \frac{\Omega_0}{F_c} \quad [2-2]$$

Where ρ is the rock density, R is the distance from the seismic source, C is the wave velocity in rock, Ω_0 is the low frequency plateau of the frequency spectrum of a seismic waveform, and F_c accounts for the radiation pattern of the seismic waves.

2.5 Manipulation of Independent Source Parameters to analyze microseismicity

Significant efforts have been made in developing methods to analyze microseismicity in underground mines. As discussed earlier seismic source parameters are used to describe the seismic source and here are some of the manipulations of those parameters to have more information about the seismic source and better description for the resulted events.

2.5.1 Moment magnitude

2.5.1.1 Magnitude general form

The magnitude (M) of an event is a numerical value that describes the proportional size or amount of elastic energy released by this event. The amplitude of the seismic wave (the maximum ground motion recorded by the monitoring system) is used to determine the earthquake size once it is adjusted for amplitude decay with distance from the epicentre due to geometric dispersion and attenuation during wave propagation. Event magnitude can be described by the general form of all magnitude scales based on measurements of ground displacement amplitudes A and periods T (Giles D., 2013).

$$M = \log\left(\frac{A}{T}\right) + F(\Delta, h) + C_S + C_R \quad [2-3]$$

Where A is the amplitude of the signal recorded on the seismogram, T is the dominant period of the signal recorded on the seismogram, F (Δ , h) is a calibration function used for the correction of the variation of amplitude with the earthquakes depth (h) and distance (Δ) from the epicentre to the seismometer recording station, C_R is a correction factor for the region where that earthquake happened, and C_S is a correction factor for the seismic station that is used to monitor the seismic event.

Since magnitude scales are logarithmic, an increase of one unit of magnitude on the magnitude scale is equivalent to an increase of 10 times the amplitude recorded by a seismograph and 32 times the accompanied seismic energy. To identify the sizes of local or distant events, different scales have been created (Giles D., 2013).

2.5.1.2 Richter scale

Richter scale is the earliest scale that was originally developed in 1935 by Charles Richter to represent the strength of medium sized earthquakes (events with magnitudes between 3.0 and 7.0) in California. Richter scale is also called the local magnitude M_L which is generally used for describing microseismic events magnitudes that are calculated from the seismic wave amplitude measured by a specific seismograph, the Wood Anderson Torsion Instrument (Giles D., 2013).

$$M_L = \log A_{max} - \log A_0 \quad [2-4]$$

Where A_{max} is the amplitude of the seismic wave and A_0 is a correction factor which is a function of distance.

However, Richter scale has some drawbacks such as the fact that it can only be used to measure shallow earthquakes within 600 kilometres. Gutenberg developed Richter's scale in 1945 to cover seismic occurrences of any epicentral distance and for deeper focal depths. It is independent of the seismograph used to record the events. This early study led to the development of two more magnitude scales, one for surface waves (M_S) and the other for body waves (M_B) (Giles D., 2013). Table 2-2 describes how the seismicity is felt qualitatively at the mine for different Richter

magnitudes, based on data from various mines in Australia and Canada (Hudyma, 2008). Richter scale can only describe the maximum wave amplitude and does not reflect the total energy that is released by the event.

Table 2-2. A qualitative relation between how an event feels in a mine and the Richter magnitude of the event (Hudyma, 2008).

RICHTER MAGNITUDE	QUALITATIVE DESCRIPTION
-3.0	<ul style="list-style-type: none"> ▪ Small bangs or bumps felt nearby. Typically only heard relatively close to the source of the event. ▪ This level of seismic noise is normal following development blasts in stressed ground. ▪ Event may be audible but vibration likely too small to be felt. ▪ Undetectable by a microseismic monitoring system.
-2.0	<ul style="list-style-type: none"> ▪ Significant ground shaking. ▪ Felt as good thumps or rumbles. May be felt more remote from the source of the event (i.e. more than 100 m away). ▪ May be detectable by a microseismic monitoring system.
-1.0	<ul style="list-style-type: none"> ▪ Often felt by many workers throughout the mine. ▪ Major ground shaking. ▪ Similar vibration to a distant underground secondary blast. ▪ Should be detectable by a microseismic monitoring system.
0.0	<ul style="list-style-type: none"> ▪ Vibration felt and heard throughout the mine. ▪ Bump commonly felt on surface (hundreds of metres away), but may not be audible on surface. ▪ Vibration felt on surface similar to those generated by a development round.
1.0	<ul style="list-style-type: none"> ▪ Felt and heard very clearly on the surface. ▪ Vibrations felt on the surface similar to a major production blast. ▪ Can be detected by regional seismological sensors located hundreds of kilometres away.
2.0	<ul style="list-style-type: none"> ▪ Vibration felt on the surface is greater than large production blasts.
3.0	<ul style="list-style-type: none"> ▪ The largest mining-induced seismic events recorded in Australia registered about Richter 3 to Richter 4

2.5.1.3 Moment magnitude scale

Moment magnitude (M_w) was introduced in 1979 by Hanks and Kanamori and has since become the most accurate method used of describing the size of the events. It more precisely ties the magnitude of an earthquake to its tectonic effect (Giles D., 2013). It measures the size of events in terms of the released energy and relates to the amount of movement by rock along the fracture and the area of the fracture surface (Rafferty J. P., 2020). The moment magnitude is defined as:

$$M_w = \frac{2}{3} \log M_0 - 10.7 \quad [2-5]$$

Where M_0 is the seismic moment measured in dyne·cm and the constant of 10.7 in the above formula will become 6.0 if the seismic moment is in N·m.

2.5.2 Frequency-Magnitude Relation

The frequency-magnitude distribution represents the relation between the magnitude M and the occurrence rate (Equation [2-6]) (Gutenberg and Richter, 1944). It is a commonly used technique in seismic hazard analysis in earthquake seismology. Mining induced seismicity follows the same magnitude-frequency distribution as crustal earthquakes (Boettcher et al., 2009).

$$\text{Log } N = a - bM \quad [2-6]$$

Where N is the cumulative number of microseismic events above magnitude M and a and b are constants.

Figure 2-9 depicts a graphical representation of the power law relation, introduced by Gutenberg and Richter (Equation [2-6]). For a large population of data, the event magnitudes are plotted on the x-axis, and the cumulative number of events with this or larger magnitude on the y-axis. The slope of the line is the b-value. When the seismic data line reaches the horizontal line at the top of the chart, the corresponding magnitude represents the seismic system sensitivity or the completeness of the data record. The intersection of the Frequency-Magnitude relation with the x-axis is (a/b) represents the largest feasible event magnitude. This value is commonly used to measure long-term seismic hazard (Brown, 2018).

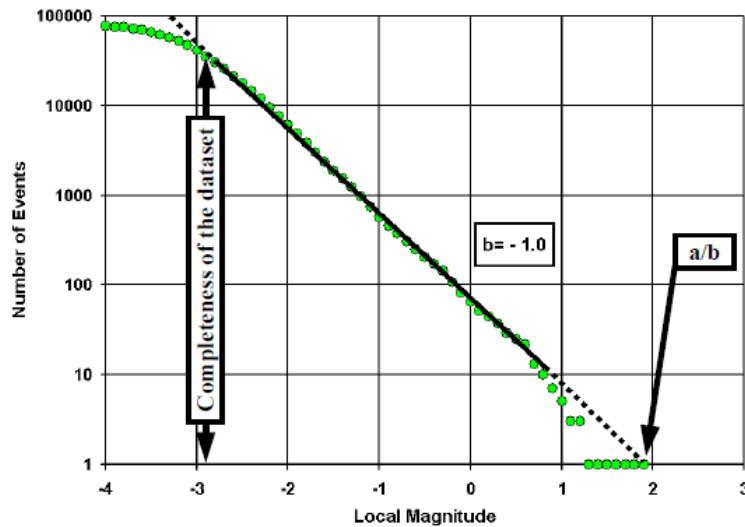


Figure 2-9. A typical Gutenberg-Richter frequency-magnitude relation for a large population of data (Hudyma, 2008).

The magnitude of completeness is considered the minimum magnitude at which 100% of the events are detected (Woessner and Wiemer, 2005). That means the seismic monitoring system has recorded all events equal to or greater than this magnitude (Figure 2-10). Thus, it is a crucial parameter to define for any seismicity analysis. Underestimating the value of magnitude of completeness results in incorrect seismicity analysis by utilising incomplete data, while overestimating it results in eliminating acceptable data (Wiemer and Wyss, 2000; Mignan and Woessner, 2012; Ma et al., 2018).

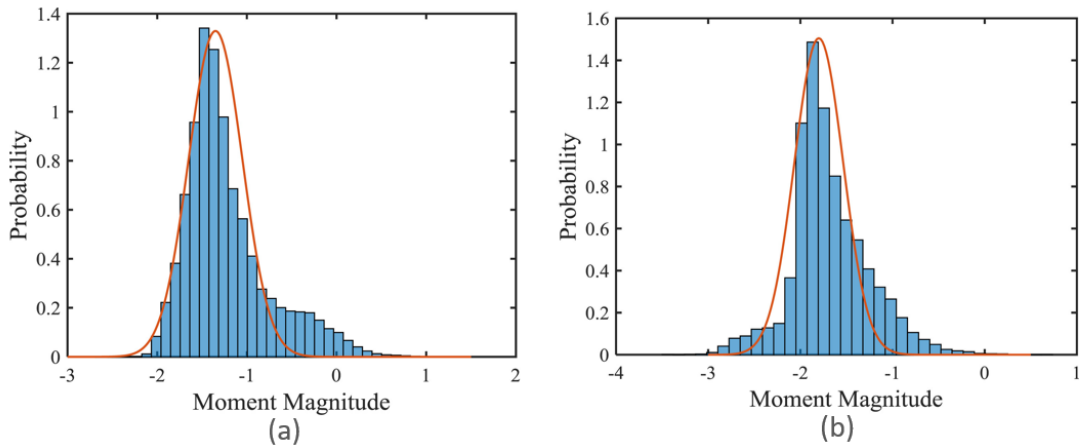


Figure 2-10. Frequency distribution with moment magnitude of seismic events at (a) Creighton and (b) Kidd Mine sites. According to the maximum frequency windows of magnitude, the magnitude of completeness at Creighton Mine should exceed -1.6 and for Kidd Mine, it should be larger than -1.9 (Ma et al., 2018).

The relative numbers of small and large events is measured by the parameter b which is usually calculated using the maximum likelihood method (Aki, 1965).

$$b = \frac{\log_{10} e}{\bar{M} - \left(M_o - \frac{\Delta M}{2}\right)} \quad [2-7]$$

Where \bar{M} is the mean magnitude of the sample and M_o is the minimum magnitude. The magnitudes are usually rounded up to the first decimal place, so that the methods used to evaluate b experimentally usually work with data grouped in classes with $\Delta M=0.1$. This final term has been added to Aki's formula for more precise estimation of the b -value (Utsu 1965; Godano et al., 2014).

b-value is considered an effective measure of seismic hazard since it is commonly used to define the relative numbers of small and large earthquakes in certain area as mentioned earlier. High b-value means small number of large magnitude events, whereas low b-value indicates an increase of large events and in turn the stability of the rock mass begins to deteriorate (Yu et al., 2022).

b-value can be used to distinguish between the high and low stressed areas as it is also related to the strength and stress of the medium (Xu et al., 2014). Scholz in 1968 studied the relation between physical parameters such as stress and confining pressure and b-value. Uniaxial compression was used to fracture various rocks with different physical properties, and magnitude-frequency curves at various stress levels were plotted. In unconfined experiments, brittle rocks showed high b-values at low stress, indicating a prevalence of small events, while b-values fall between 1 and 0 by increasing the stress which implies that, events become statistically larger. Frictional sliding on pre-existing cracks was thought to be the cause of the micro-fracturing activity in the first case and in the latter micro-fracturing was attributed to propagation of new cracks. In the triaxial experiments, low b values are observed when confining pressure keeps cracks tightly closed and restricts sliding. Amitrano (2003) has also reported the inverse relation between b-value and the confining pressure in his experiments. Verdecchia et al. (2022) analyzed the variation in b-values with depth in the Charlevoix Seismic Zone in North America. b-values of the entire catalog decreased with depth until around 12 km (the upper-middle crust boundary) which agrees with Scholz (1968) and Amitrano (2003) observations. On the other hand, b-values of the events within the impact structure increased between 10 and 13 km which indicates an upper crust that is locally fractured and weak according to Yu, et al. (2016).

Studies have found that a sudden decrease in the b-value may precede larger events (Kanamori, 1981). Urbancic and Trifu (2000) studied the variation in b-value in Strathcona mine, Sudbury, Canada at depth below 600 m for 1 month before and 1 month after 2.9 moment magnitude seismic event. They noted that b-value decreased from 1.2-1.4 to 0.6-0.8 before the large event by 2-3 days. The decrease in b-value before the occurrence of a large magnitude earthquake is probably related to a relative increase in the effective stress (Trifu and Urbancic, 1996). In 2018, Ma et al. presented the change of b-value associated with mining-induced seismicity sequences at two different mines (Creighton Mine and Kidd mine). A uniform pattern of b-value change was noticed

before the mainshocks occurrence. b-value initially dropped before the mainshocks and then went up within mainshocks' timeframe.

Moreover, b-value may vary according to the seismic mechanism (Legge and Spottiswoode, 1987). The b-value of seismicity generated by fault slip is often small (less than 0.8), whereas seismicity caused by stress change from mine blasting has a b-value in the range of 1.2 to 1.5. Examples will be discussed in Chapter 3. Wang et al. (2020) studied the relation between M_w 4.6 event and hydraulic fracturing activity in British Columbia. The event magnitude appears to be larger than the one anticipated based on the injected volume, indicating that the event most probably occurred on a pre-existing fault. This was confirmed by the estimated low b-value of 0.78. Schorlemmer et al. (2005) and Gulia and Wiemer (2010) noted that b-value depends on the faulting style. Gulia and Wiemer (2010) built a model consisting of 10 tectonic zones, each has specific faulting style, and calculated the b-value for each zone. The reverse zones have the lowest b-values (0.75–0.81) while the highest values were recorded for the normal zones (1.09), followed by the strike-slips (0.9–0.92). These results agree with the inverse relation between b-value and stress.

Using different simple techniques combined, including b-value, based on the available microseismic data, can give indication to the failure process at the source. For instance, if the source location is close to a specific structure and b-value is low, this may point to a slipping structure. On other hand, if the ratio of radiated energy from the shear wave compared to the compressional wave is small (non-shear) and b-value is high, volumetric stress change is most likely the cause of failure especially if the events correlate with blasting time and the source location is close to mine developments or stopes (Hudyma and Potvin, 2010). Although the b-value is used in seismic hazard assessment at various scales, providing a simple index of the b-value is insufficient. Limitations and uncertainties in seismicity predictions may result in inaccurate conclusions (Ma et al., 2018).

2.5.3 Magnitude-Time History Charts

As mining is a dynamic activity, seismic analysis should include the rockmass response to mining over time. Magnitude-Time History chart shows events in order with date/time on the x-axis, and magnitude on the y-axis and the cumulative number of events over time represented through a line

corresponding to the y-axis (Figure 2-11). Constant slope in the relation reflects a constant rate of events, while a curved line with different slopes indicates variable seismicity that may be related to mining activity in the corresponding time (Hudyma, 2008).

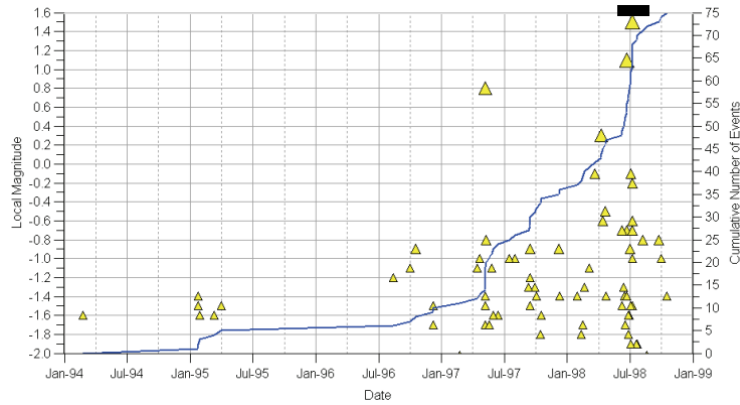


Figure 2-11. Magnitude-Time History chart for a group of seismic events at Mount Charlotte mine. The black line at the top represents the blasting period. It is obvious the increase of the event rate with mining activity. However, numerous events occurred before blasting start (Hudyma, 2008).

2.6 Moment tensor decomposition and solution

Understanding the failure mechanisms of microseismic events in underground mines is critical for hazard assessment. Moment tensor inversion is the commonly used method to understand the source mechanisms. A focal mechanism solution is derived from analyzing the waveforms generated by seismic activity, thus, it is considered a direct way to analyze rockbursts (Cronin, 2004). Source parameters such as the scalar moment, moment amplitude, full moment tensor, and fault plane solutions can be resolved for a seismic sequence in fault zones (Ma et al., 2019).

The moment tensor describes the deformation at the source location based on generalised force couples arranged in a 3 x 3 symmetric matrix (Dahm and Krüger, 2014; Eyre and Van Der Baan, 2015). It represents the strength of a seismic source in terms of its seismic moment and the seismic waves radiation pattern. The moment tensor description is not restricted only to earthquake sources but can also represent other types of seismic sources such as explosions, implosions, and rock falls. The diagonal elements in the moment tensor are called linear vector dipoles. The off-diagonal elements are moments defined by force couples that are equal and opposite in direction (Figure 2-12) (Dahm and Krüger, 2014).

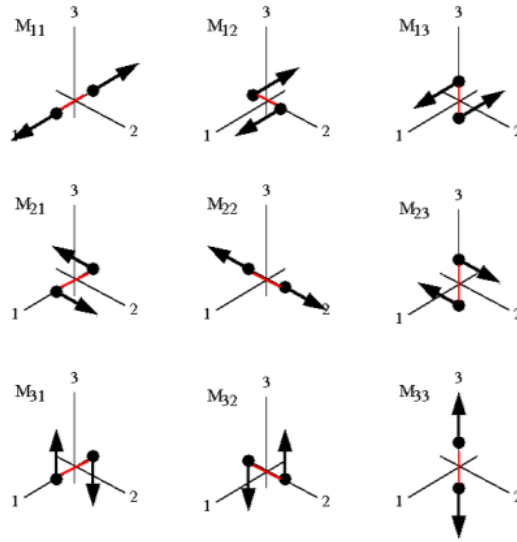


Figure 2-12. The system of force couples representing the components of a Cartesian moment tensor. Diagonal elements represent linear vector dipoles, while off diagonal elements represent force couples with moment (Dahm and Krüger, 2014).

2.6.1 First motion analysis

The direction of the force couples, parallel to the failure plane and a perpendicular auxiliary plane (the nodal planes), corresponds to the force at the source and defines if the polarity of P wave first motion will be positive or negative (Wamboldt, 2012). Moment tensors are frequently displayed as beach balls since it is difficult to interpret a matrix of numbers. The moment tensor defines the amount and direction of the first motion for each point on the surface of the beach ball. The beachball diagrams are stereographic projections that separate the area around the fault into four quadrants, two black and two white, divided by great-circle arcs orientated 90 degrees apart representing the two nodal planes. The motion of P-wave in the medium around the source made the particles in the black quadrants to move away from the source (P-wave first motion is upward on a seismograph), while the particles in the white quadrants move toward the source (P-wave first motion is downward) (Figure 2-13). The slip direction will be from the white to the black quadrant along the fault surface. For the location of the pressure (P) and tension (T) axes, the tension axis is in the middle of the compressional (black) quadrant and vice versa (Cronin, 2004).

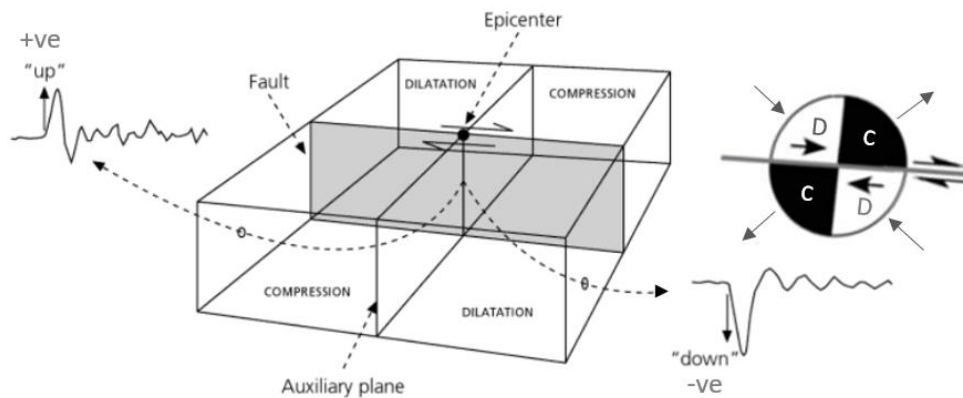


Figure 2-13. First motion analysis for focal mechanism solution (FMS) (after Stein and Wysession, 2009).

2.6.2 Moment tensor inversion

First-arrival polarity method, amplitude methods, and the full-waveform method are the three basic techniques used in moment tensor inversion. First-arrival polarity method is the simplest and easiest technique to calculate the moment tensor. This method usually assumes that the mechanism is a double couple. The radiation pattern at the source can be represented using the polarities of the first arrivals at each sensor (Figure 2-13). Sensor distribution is crucial using this technique; besides it is difficult sometimes to identify P-wave. For complex mechanisms (not basic DC or explosion/implosion mechanisms), it might be hard to solve using this method. Another drawback is that it can provide a wide range of results that all equally fit the data (Eyre and van der Baan, 2015).

Amplitude methods use P and S wave amplitudes to better constrain the orientation of the radiation patterns. In contrast to S-wave amplitudes, P-wave amplitudes are larger close to the pressure (P) and tension (T) axes and smaller close to the nodal planes. In addition to the radiation pattern, the amplitudes might be affected by other factors that should be considered such as attenuation or station site effects. Using S/P amplitude ratios can result in optimal solutions (Julian et al., 1998). There is also a potential difficulty in picking the P and S arrivals when using this method (Eyre and van der Baan, 2015).

According to Eyre and van der Baan (2015), the full waveform method is considered more accurate since the full waveform measured by the acquisition system is inverted to calculate the moment

tensor. This approach is computationally expensive. The data recorded at the stations have both the source effect and propagation effect combined. Propagation effect between source and receivers (attenuation, scattering, and local site effects) can be modelled (using Green's functions, G) and removed. For low frequency data, the full waveform technique performs better. It could become unstable at higher frequencies. In this case, the inversion using only the amplitudes of P and S waves from the recorded data and Green's functions is performed (Eyre and van der Baan, 2015).

Green function computes the ground displacement recorded by the seismic sensor and describes all wave propagation effects including the elastostatic response of the Earth. The ground motion response $u(t)$ at a station depends on $G(t)$ (Dahm and Krüger, 2014; Tierney, 2019). Thus, the moment tensor inversion is based on the following expression:

$$U = G M \quad [2-8]$$

Where M is the moment vector composed of six independent components of moment tensor ($M=[M_{11}, M_{22}, M_{33}, M_{23}, M_{13}, M_{12}]^T$), U is a vector representing observed amplitudes at sensors ($n \times 1$) where n is the number of observed amplitudes for a given event, and G is the $n \times 6$ Green's function derivative matrix, which represents the response of the medium from the source to the sensor (Ren et al., 2021).

$$G = \begin{matrix} G_1^{(1)} & G_2^{(1)} & G_3^{(1)} & G_4^{(1)} & G_5^{(1)} & G_6^{(1)} \\ G_1^{(2)} & G_2^{(2)} & G_3^{(2)} & G_4^{(2)} & G_5^{(2)} & G_6^{(2)} \\ \dots & \dots & \dots & \dots & \dots & \dots \\ G_1^{(n)} & G_2^{(n)} & G_3^{(n)} & G_4^{(n)} & G_5^{(n)} & G_6^{(n)} \end{matrix} \quad [2-9]$$

Where $G_k^{(i)}$ is the k^{th} element of the Green's function matrix of the i^{th} sensor.

$$G_1^{(i)}=G_{1,1}^{(i)}, G_2^{(i)}=G_{2,2}^{(i)}, G_3^{(i)}=G_{3,3}^{(i)},$$

$$G_4^{(i)}=G_{2,3}^{(i)}+G_{3,2}^{(i)}, G_5^{(i)}=G_{1,3}^{(i)}+G_{3,1}^{(i)}, G_6^{(i)}=G_{2,1}^{(i)}+G_{1,2}^{(i)}$$

Where $G_{p,m}^{(i)}$: is the amplitude measured along the m^{th} -axis produced by a point force directed along the p^{th} -axis.

When solving the expression $U = G M$, the least-square method is often used for calculating the moment tensor (Ren et al., 2021).

$$M = (G^T G)^{-1} G^T U \quad [2-10]$$

ESG Solutions uses SMTI package to simulate the radiation pattern of body waves using the amplitudes of the low frequency spectral plateaus of the Brune source model (1970, 1971) and first motion polarities. According to Andrew (1986), the low-frequency spectral levels of wave amplitudes and corner frequency, which is the frequency corresponding to the intersection of the low-frequency spectral level and high-frequency decay in the displacement amplitude spectra, can be determined as follows.

$$\Omega = \frac{2S_{D2}^{3/4}}{S_{V2}^{1/4}} \quad [2-11]$$

$$f_c = \frac{1}{2\pi} \sqrt{S_{V2}/S_{D2}} \quad [2-12]$$

Where Ω is the low frequency spectral amplitude of Brune's (1970) seismic source displacement spectrum model, f_c is the corner frequency, $S_{D2} = \int_{t_1}^{t_2} D^2(t)dt$, $S_{v2} = \int_{t_1}^{t_2} V^2(t)dt$, and D and V are the displacement and velocity time series (Urbancic et al., 1996). Ω is evaluated for different phases (P, S_H , and S_V) at the available sensors. The limits of the integrals t_1 and t_2 represent the time window which samples P or S phases (Wamboldt, 2012).

2.6.3 Moment tensor decomposition

Double-couple (DC) source is the most common type of moment tensor, especially in tectonic earthquakes, and it represents pure shear failure along planar fault surfaces. Research in the source mechanisms of induced seismicity has shown similarity between mining induced seismic events and natural earthquakes (McGarr, 1971). However, additional analysis shows that seismic sources usually display more general moment tensors with substantial non-double-couple components (Julian et al., 1998). Zhang et al. (2016) analyzed eight induced earthquakes in the Western Canadian Sedimentary Basin where induced seismicity was attributed to fluid injection during hydraulic fracturing activity. Significant ISO and CLVD components were reported for the induced seismic events (This will be discussed later). The ISO component reached 40% in one event and in another it reached 70% combined with CLVD component. In underground mines, it

is crucial to determine the non-DC source components of moment tensors to assure the safety of mining operation as these processes are often accompanied by tunnel damage (Caputa et al., 2021). As mentioned earlier in Section 2.2.2, Hasegawa et al. (1989) proposed different types of failures, which can occur in underground mines. Examples are roof collapse, pillar burst, tensile failure, and volumetric deformation.

McGarr (1992) studied ten large, induced events in two mining districts in South Africa; volumetric reduction with shear deformation observed in seven of them. Šílený and Milev (2008) processed five seismic events recorded at Driefontein gold mine. Three of the events experienced implosion deformation equivalent to burst of a pillar, according to their location, while the fourth one experienced tensile deformation, and the 5th event was mainly DC. Dreger et al. (2008) revealed predominant implosive deformation as well for magnitude 3.9 event in Utah. Lizurek and Wiejacz (2011) analyzed the source mechanism of fifty seismic events from Rudna Copper Mine, and significant number of events had some CLVD and ISO components involved. Stec and Drzewiecki (2012) studied the causes of rockbursts that occurred in the Rydułtowy-Anna Mine. They discovered that the events under analysis could be identified by either shearing or explosive mechanisms. Vavryčuk and Kühn (2012) revealed high and negative ISO component for the rockburst, while the DC component is minor which depicts the existence of a small shear deformation in a primarily implosive source. Ma et al. (2019) studied the focal mechanism of 20 induced events in Yongshaba mine in China. The events were classified into three groups according to their location with respect to the fault zones in the studied area. Shear-tensile failure mechanisms predominated in one group, while compressional failure mechanisms associated with rock collapse and tensional failure associated with crack opening were demonstrated in another one.

To decompose the moment tensor, it is transformed into a coordinate system with basis vectors corresponding to the orthonormal eigenvectors (Jost and Herrmann, 1989).

$$M = \{a_1 \quad a_2 \quad a_3\} m \begin{pmatrix} a_1^T \\ a_2^T \\ a_3^T \end{pmatrix} \quad [2-13]$$

$$M = \begin{Bmatrix} a_{1x} & a_{2x} & a_{3x} \\ a_{1y} & a_{2y} & a_{3y} \\ a_{1z} & a_{2z} & a_{3z} \end{Bmatrix} \begin{Bmatrix} m_1 & 0 & 0 \\ 0 & m_2 & 0 \\ 0 & 0 & m_3 \end{Bmatrix} \begin{Bmatrix} a_{1x} & a_{1y} & a_{1z} \\ a_{2x} & a_{2y} & a_{2z} \\ a_{3x} & a_{3y} & a_{3z} \end{Bmatrix} \quad [2-14]$$

Where a_i are the orthogonal eigenvectors, and m is a diagonal matrix of eigenvalues.

Knopoff and Randall (1970) decomposed the moment tensors into isotropic (ISO) and deviatoric components. The isotropic component represents a uniform volume change (expansion or contraction) (Figure 2-14) while the deviatoric component represents displacement with zero volume change (e.g., fault dislocation). The deviatoric component can be divided into the DC (pure shear) and compensated linear vector dipole CLVD (normal dislocation) components. The latter should be analyzed with caution since it could be explained with other possible mechanisms. For instance, pillar burst under compression (Figure 2-15) can be represented by the sum of an isotropic moment tensor and a compensated linear vector dipole (CLVD) moment tensor (Eaton, 2008). More details will be discussed in Chapter 3. Many different decompositions have been attempted, but Knopoff and Randall's decomposition was largely adopted since it proved useful for physical interpretations and can be used to determine which type of source is represented by the tensor (Vavryčuk, 2015). The relative proportions of the ISO, DC and CLVD components in the seismic source can be represented using Hudson chart (will be discussed in Chapter 3).

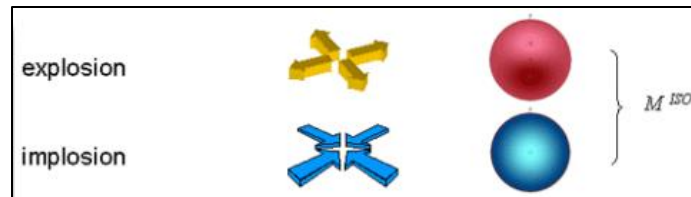


Figure 2-14. Graphical representation of the positive (explosion) and negative (implosion) meaning of the isotropic component (after Eaton, 2008).

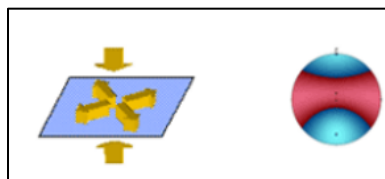


Figure 2-15. Graphical representation of a mixed source event (pillar burst under compression) has Iso and CLVD components (after Eaton, 2008).

2.6.4 Physical characteristics of the decomposition

According to Vavryčuk, 2015, the physical properties of the decomposition can be summarized as following:

- The explosion or implosion is an isotropic source, characterized by $C_{ISO} = \pm 1$ and zero C_{CLVD} and C_{DC} , where C values are relative scale factors and $|C_{ISO}| + |C_{CLVD}| + |C_{DC}| = 1$.
- Shear faulting is represented by the double-couple force and characterized by $C_{DC} = 1$ and by zero C_{ISO} and C_{CLVD} .
- Shear faulting on a non-planar fault is characterized by a non-zero C_{DC} and C_{CLVD} . The C_{ISO} is zero because there is no volumetric changes.
- Pure tensile or compressive faulting is free of shearing and thus characterized by zero C_{DC} . However, the non-DC components contain both ISO and CLVD components. Both have the same sign which is positive for tensile fracturing and negative for compressive fracturing.
- The shear-tensile source combines both shear and tensile faulting and characterized by non-zero ISO, DC, and CLVD components. The ratio between the non-DC and DC components defines the angle between the slip and the fault.

In contrast to these simple models, micro-seismic events could combine different mechanisms. Thus, it is critical to decompose a complex event into the common forms of ISO, DC, and CLVD components to understand the failure mechanism. Figure 2-16 shows an example of moment tensor decomposed into 13% of explosion, 55% of fault-slip, and 32% of tensile opening (Krieger and Heimann, 2012).

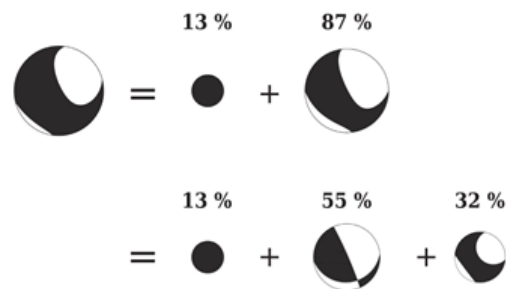


Figure 2-16. Example of moment tensor decomposition (Krieger and Heimann, 2012).

Uncertainty in focal mechanism solutions could be attributed to numerous factors including data noise, inaccurate velocity model, sensor coverage, and the inversion method itself (Scognamiglio et al., 2016; Zhang et al., 2016; Vavryčuk, 2015). In underground mines, limited network coverage due to mine development design (specified location and orientation) can affect the analysis performance and such problem cannot be easily solved. Data noise and/or inaccurate velocity model, which are prevalent issues in mining seismology, could be major sources of uncertainty in moment tensor solutions as well (Caputa et al., 2015).

2.7 Summary

A high stress environment brought on by underground mining activities could result in drastic rock failure. The risk associated with induced seismicity needs to be studied for the safety of mine operators and to minimize production losses. Induced seismicity is influenced by a variety of mining and geological parameters, and it is critical to analyze produced seismic events to comprehend the effects of these characteristics. Understanding the microseismic source parameters such as the event location, time, size, radiated energy, and moment tensor must come first in seismic analysis. Manipulation of independent source parameters (e.g., frequency-magnitude analysis) has been used to analyze microseismicity and have more information about the seismic source and how it relates to mining activity or geology conditions.

In mines, there is a variety of seismic source mechanisms that may occur relatively close to each other and create seismic events. It is essential to decompose a complex event into its isotropic and deviatoric components to better understand the failure mechanism. A focal mechanism solution is derived from analyzing the waveforms generated by seismic activity, thus, it is considered a direct way to analyze rockbursts or microseismicity for hazard evaluation. The rock fracturing process can be quantitatively determined from moment tensor inversion and decomposition of the full moment tensor.

Bridging text between manuscripts

The following chapter reports on a case study mine of Young-Davidson (YD) mine of Alamos Gold Inc. in northern Ontario, Canada. YD mine is experiencing more M_n 2.0+ events starting in 2020 (Figure B1-1). Most large events in 2020 and 2021 were recorded around levels 9590 (approximately at 700 m depth below surface) and 9440 (Figure B1-2). Large seismic events at shallow depths in YD mine is irrational compared to other Canadian Shield mines in Sudbury and Timmins. Thus, it is necessary to conduct seismic analysis and understand how the mining activity impacts the stress conditions and induced seismicity. The following chapter is a comprehensive study of the microseismic database to understand the reasons behind large seismic events. Statistical methods are used to analyze seismic data and relate it to mining operations. Variation of b-value, derived from the microseismic event magnitude-frequency distribution, is used along with moment tensor inversion in MATLAB to interpret the induced seismicity. The mine location, geology, monitoring system used as well as information about the induced seismicity are also presented. To carry out the analysis, the seismic catalog was shared by the industry partner including information on the location of seismic events as well as the calculated source parameters such as seismic moment, moment magnitude, seismic energy, apparent stress, and stress drop as shown in Figure B1-3. All data calculations were done in ESG microseismic monitoring system.

The following chapter is a published paper in the Journal of Sustainable Mining, 2022, Vol. 21: Iss. 3, Article 5. This research article is available at: <https://doi.org/10.46873/2300-3960.1361>

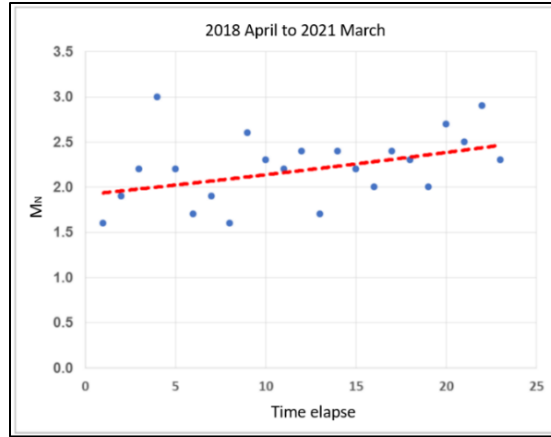


Figure B1-1. Magnitude-Time chart of YD large seismic events recorded by the CNSN from April 2018 to March 2021 (Alamos Gold Inc., 2021).

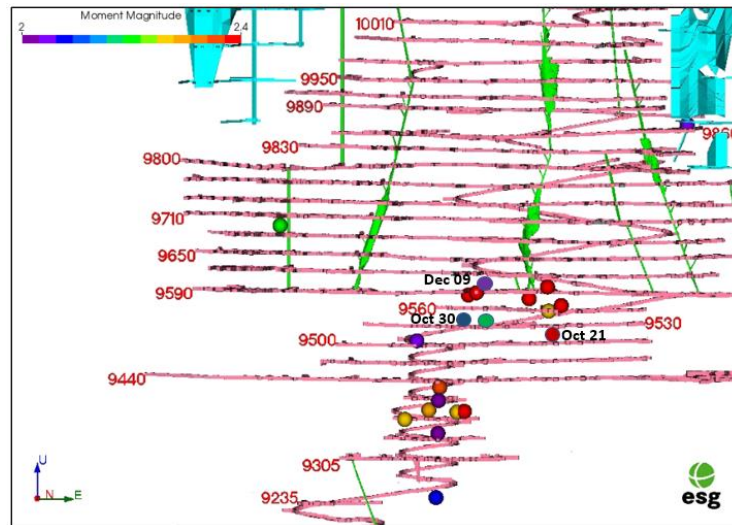


Figure B1-2. M_w 2.0+ events recorded by ESG system in YD mine in 2020 and 2021 with respect to YD mine layout in section view.

DateTime	Northi	Eastin	Depth	MomentMagnitud	SeiMoment	Energy	EsEp	StaticStressDrop	ApparentStress	DynamicStressDrop	LocalMagnitude
10-21-2020 17:52:07	10340.4	23441.4	9515.79	2.403776	4.03E+12	5.11E+07	3.843729	1.11E+07	4.56E+05	0.00E+00	2.579806
12-24-2020 10:58:48	10385.3	23320.2	9547.12	2.238379	2.28E+12	1.33E+07	8.866019	3.77E+06	2.09E+05	0.00E+00	2.274668
10-30-2020 13:44:03	10396.7	23286.5	9549.28	2.067595	1.26E+12	6.56E+06	3.468262	4.77E+06	1.87E+05	0.00E+00	2.172577
12-09-2020 13:03:12	10395	23325.6	9611.71	2.038032	1.14E+12	1.05E+07	7.328298	6.45E+06	3.31E+05	0.00E+00	2.415755
12-02-2020 17:38:25	10477	22907.4	9741.60	1.793212	4.90E+11	2.08E+06	11.22182	1.59E+06	1.20E+05	1.26E+07	1.112497
10-30-2020 13:45:17	10400.6	23325.6	9608.9	1.528484	1.96E+11	2.69E+05	3.917691	1.04E+06	4.93E+04	0.00E+00	1.355479
09-08-2020 17:39:18	10334.5	23330.8	9567.83	1.486951	1.70E+11	1.63E+05	10.00909	4.58E+05	3.45E+04	0.00E+00	1.27267
12-18-2020 9:16:26	10363.0	23430.3	9615.39	1.256554	7.67E+10	1.66E+05	5.870095	1.56E+06	7.79E+04	0.00E+00	1.159764
11-30-2020 1:12:11	10332.2	23253.3	9367	1.237502	7.18E+10	2.89E+05	2.469717	2.24E+06	1.14E+05	7.40E+06	0.4437315
08-13-2020 2:06:29	10370.5	23263.7	9297.15	1.193161	6.16E+10	2.52E+05	6.28892	2.65E+06	1.47E+05	0.00E+00	1.172964
12-29-2020 18:20:18	10393.5	23283.4	9573.56	1.169067	5.67E+10	6.38E+04	1.373697	1.19E+06	4.05E+04	0.00E+00	0.7130921
10-30-2020 22:28:44	10369.4	23324	9571.56	1.141325	5.15E+10	8.84E+04	3.322236	1.52E+06	6.17E+04	0.00E+00	0.6589472
12-31-2020 11:08:21	10409.8	23276.2	9573.28	1.135599	5.05E+10	7.21E+04	1.65482	1.47E+06	5.14E+04	0.00E+00	0.7924766
11-18-2020 17:48:44	10395	22954.7	9704.08	1.086804	4.27E+10	5.46E+04	6.556375	6.41E+05	3.63E+04	3.50E+06	0.0273241
12-31-2020 5:42:04	10390.7	23285.4	9577.59	1.014459	3.32E+10	1.40E+04	1.913866	3.56E+05	1.51E+04	0.00E+00	0.2683928
09-08-2020 18:26:54	10402.1	23277.4	9552.19	1.008293	3.25E+10	5.56E+04	4.172616	1.24E+06	6.15E+04	0.00E+00	0.7984612

Figure B1-3. M_w 1.0+ seismic events recorded by ESC monitoring network at YD mine in 2020 with the calculated source parameters in the microseismic system.

Chapter 3 - Effect of Mining and Geology on Mining-Induced Seismicity – A Case Study

Abstract

Mining-induced seismicity is a commonly occurring phenomenon in underground mines. This poses a greater challenge to the safety of the mining operation. This paper presents a case study of the Young-Davidson mine in northern Ontario, Canada, where seismic events of magnitude M_n 2.0+ have been observed at mining depths of 600-800 m below the surface. The occurrence of large seismic events at such shallow depths is the key issue of this study. A comprehensive study of the microseismic database has been conducted to discern the root causes for the unusually strong seismic activities recorded at shallow depths. The effects of mining activities in the vicinity of two dykes intersecting the orebody on the seismic response are investigated. Variation of the b-value derived from the magnitude-frequency distribution is examined, and moment tensor inversion for three large seismic events is carried out to determine the source mechanisms. It is shown from this investigation that the influence of the sill pillar is more critical, leading to high mining-induced stress and the occurrence of large events. While the findings from this research are specific to this case study, they could be used to shed light on the causes of induced seismicity at other mines with similar conditions.

Keywords: underground mining, mining-induced seismicity, moment tensor inversion, magnitude-frequency distribution.

3.1. Introduction

Fracture initiation, propagation, and rock mass movement along pre-existing fracture planes can occur when large volumes of rock are excavated. This process is usually accompanied by the generation of seismic waves known as mining-induced seismicity. As the orebody extends deeper and geologically complex structures are encountered, mining-induced seismic hazards are likely to become more prevalent. Induced seismicity has been recorded in underground mining and civil tunnelling projects worldwide for a wide variety of rock mass environments [1-4]. Mining-induced seismic events take place due to the interaction of tectonic and mining-induced stresses. Seismic

events correspond to the sudden release of elastic strain energy in the rock mass and can be represented by the movements caused by the sudden failure of rock masses due to stress concentration in the mining area [3,5]. Mine development activity and ore extraction in underground mines create a high-stress environment that may lead to drastic rock failure, generally known as rockburst. This could result in production losses, equipment damage, and even fatalities because of sudden rock mass failure in mine workings. According to Blake and Hedley [6], a 3.0 magnitude seismic event could cause significant damage to the rockmass, as well as the instability of underground openings, such as triggering rock falls within a 100-m radius of the seismic source. Strong and shallow seismic events can result in the collapse of a mine roof, and for miners working in the vicinity of the falling rock, this poses a direct threat to their lives [2,7]. To mitigate the risks associated with mining-induced seismicity and improve mine safety, many studies focused on forecasting mining-induced seismicity by analysing the microseismic data from microseismic monitoring systems [7-10]. Other researchers attempted to understand rockburst mechanisms to predict seismic hazard through numerical modelling methods [11,12]. This paper presents a case study of the Young-Davidson (YD) mine of Alamos Gold Inc. in northern Ontario, a gold mining operation using a sublevel stoping method with delayed paste fill. The average production of the mine is 8,000 tpd. While deep excavations are normally expected to be associated with strong seismic activities, seismic events of magnitude $M_n 2.0+$ have been observed at mining depths of only 600-800 m below the surface. The occurrence of large seismic events at such shallow depths is the main concern of this investigation. Thus, the aim of this study is to analyse the microseismic database to understand the mechanisms for the unusually strong seismic activities. Seismicity in mines could be affected by depth, production rate, mine geometry, geological structures such as dykes, faults, or any other geological features, as well as the ambient tectonic stress. In any given case, one or a combination of these factors may play a significant role in induced seismicity [13-15]. Tracking and analysing the causes of mining-induced seismic events would help better understand the influence of such parameters. It could also prove useful for both short and long term mine planning to control the occurrence of strong seismic events and provide a safer work environment throughout the life of a mine plan [16]. The effects of mining parameters and geological conditions on the seismic response in the YD mine are considered in this study. Statistical methods are utilized to characterize the seismic data and predict the trend of seismic hazards. The relation between blasting volume and induced seismicity is analysed, and frequency-

magnitude distribution is used for seismicity analysis. The influence of two regional dykes intersecting with the orebody is also examined to reveal the effect of the geological parameters. Furthermore, possible effects of the sill pillar and resulting higher stress regime are explored.

3.2. Microseismic analysis in underground mines

3.2.1 Frequency-magnitude distribution

Significant efforts have been made in developing methods to analyse microseismicity in underground mines. One of the most common manipulations of seismic source parameters to obtain more information about the seismic source and describe the event is the frequency-magnitude analysis. Gutenberg and Richter [17] proposed a power law between the event frequency and magnitude.

$$\text{Log } N(M) = a - bM \quad [3-1]$$

In the above $N(M)$ is the total number of microseismic events above magnitude M , and a and b are constants. Figure 3-1 shows a graphical representation of two different frequency-magnitude relations for two different datasets. The events are plotted with the magnitude on the x-axis and $N(M)$ on the y-axis. From this distribution, the b-value is an indicator of the seismic hazard as it describes the frequency of occurrence of large events versus small events in a certain area [18]. When the b-value is high (Figure 3-1b), the number of large magnitude events is less. If the b-value is low (Figure 3-1a), the number of large events is increased, and the stability of rock mass is deteriorated [19]. The b-value can be used to differentiate between the high and low-stressed areas as it is also related to the strength and stress of the medium [20]. In addition, the b-value differs from the seismic mechanism. If seismicity is caused by fault slip, the b-value is usually low (often less than 0.8), whereas when seismicity is due to blasting, the b-values are usually in the range of 1.2-1.5 [21,22]. Thus, the seismic source for the dataset in Figure 3-1a is interpreted as fault-slip since a low b-value of 0.5 is obtained. Both datasets in Figure 3-1 have nearly the same number of events with a magnitude equaling zero, however, the low b-value for the dataset in Figure 3-1a reflects the high proportion of large events, while the group in Figure 3-1b has almost no large events but many small events (represented by the high b-value). Thus, comparing the two cases, the seismic hazard is much higher for the group in Figure 3-1a [18].

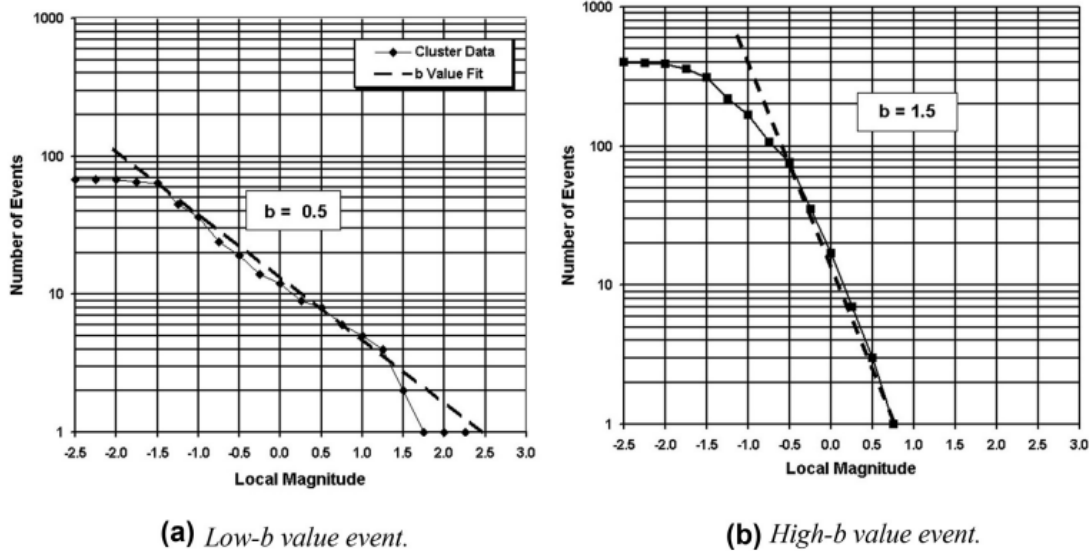


Figure 3-1. Frequency-magnitude charts for two different groups of events [18].

3.2.2 Moment tensor decomposition and solution

Understanding rock fracturing and failure mode for hazard evolution in underground mines necessitates research into focal mechanisms of induced seismicity. A focal mechanism solution is derived from analysing the waveforms generated by seismic activity and used to illustrate the mechanism of rock failure [23]. The orientation of rock fracturing and type of rupture are quantitatively determined from the moment tensor inversion method using full waveforms and decomposition of the full moment tensor [24]. The moment tensor M represents the source of a seismic event as it describes the deformation at the source location that generates seismic waves based on generalised force couples, arranged in a 3×3 symmetric matrix with six independent elements. The moment tensor description is not restricted only to earthquake sources but can also represent other types of seismic sources such as explosions, implosions, and rock falls. The diagonal elements in the moment tensor are called linear vector dipoles. The off-diagonal elements are moments defined by force couples that are equal and opposite in direction [25,26].

$$M = \begin{bmatrix} m_{11} & m_{12} & m_{13} \\ m_{21} & m_{22} & m_{23} \\ m_{31} & m_{32} & m_{33} \end{bmatrix} \quad [3-2]$$

Beach balls are the graphical representation of the moment tensor. Focal mechanism solution (FMS) beachball diagrams are stereographic projections that depict two black quadrants and two white quadrants divided by two great-circle arcs orientated 90° apart, as shown in Figure 3-2a. The

potential nodal planes are the great-circle arcs as one of them is parallel to the fault surface that caused the event. Figure 3-2b shows the direction of the first motion at the instant of the event, where the motion of the P-wave in the medium around the source made the particles in the black quadrants move away from the source whilst the particles in the white quadrants move toward the source. This results from either right-lateral slip in the east-west direction or left-lateral slip in north-south direction. Along the fault surface, the slip direction will be from the white to the black quadrant (black arrows). Figure 3-2c represents P-wave polarity. If the first motion of the P-wave is upward on a seismograph, the motion is away from the source and vice versa [23].

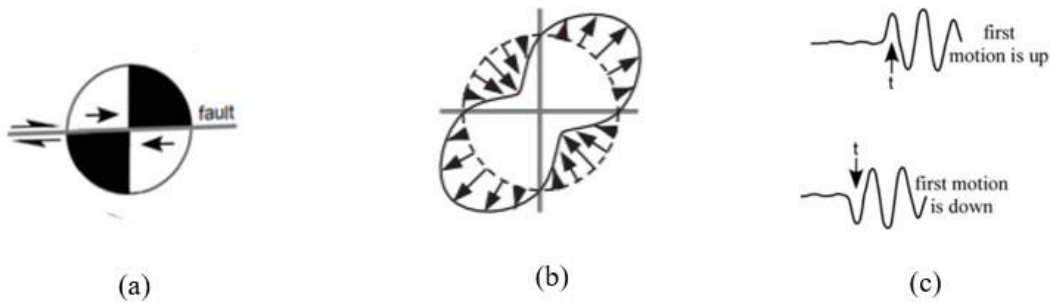


Figure 3-2. First motion analysis. (a) Beach ball diagram of strike-slip faulting with two auxiliary planes. (b) Direction of the first motion at the instant of the event. (c) P-wave polarity (after [23]).

The double-couple (DC) source, which reflects the force equivalent of shear faulting, is the most common type of moment tensor. However, some studies show that seismic sources often display more general moment tensors with significant non-double couple components [27]. An explosion, pillar burst or collapse of a cavity in mines are good examples of a non-DC source [28]. To identify which type of seismic source is represented by the moment tensor, Knopoff and Randall [29] decomposed the moment tensors into three elementary parts; the isotropic (ISO), DC, and compensated linear vector dipole (CLVD) components (Equation [3-3]). There are many other decompositions that have been proposed, but Knopoff and Randall decomposition proved to be useful for physical interpretations and became widely accepted [30]. To decompose the moment tensor, the matrix (Equation [3-2]) should be rotated to zero the off-diagonal elements. The rotation process creates three orthogonal vectors known as linear vector dipoles. Thus, every moment tensor can be written as three orthogonal linear vector dipoles rotated to a specific orientation (M_1 , M_2 , and M_3) [31].

$$\mathbf{M} = M_{\text{ISO}}\mathbf{E}_{\text{ISO}} + M_{\text{DC}}\mathbf{E}_{\text{DC}} + M_{\text{CLVD}}\mathbf{E}_{\text{CLVD}} \quad [3-3]$$

where E_{ISO} , E_{DC} , and E_{CLVD} are the ISO, DC, and CLVD elementary tensors, and M_{ISO} , M_{DC} , and M_{CLVD} are the ISO, DC, and CLVD components in the 3-D source-type space.

$$E_{ISO} = \begin{bmatrix} 1 & 0 & 0 \\ 0 & 1 & 0 \\ 0 & 0 & 1 \end{bmatrix}, E_{DC} = \begin{bmatrix} 1 & 0 & 0 \\ 0 & 0 & 0 \\ 0 & 0 & -1 \end{bmatrix}, E_{CLVD}^+ = \frac{1}{2} \begin{bmatrix} 2 & 0 & 0 \\ 0 & -1 & 0 \\ 0 & 0 & -1 \end{bmatrix}, E_{CLVD}^- = \frac{1}{2} \begin{bmatrix} 1 & 0 & 0 \\ 0 & 1 & 0 \\ 0 & 0 & -2 \end{bmatrix} \quad [3-4]$$

E_{CLVD} is positive when $M_1 + M_3 - 2M_2 \geq 0$ and negative when $M_1 + M_3 - 2M_2 < 0$.

$$M_{ISO} = \frac{1}{3} (M_1 + M_2 + M_3), M_{CLVD} = \frac{2}{3} (M_1 + M_3 - 2M_2), M_{DC} = \frac{1}{2} (M_1 - M_3 - |M_1 + M_3 - 2M_2|) \quad [3-5]$$

The isotropic component, M_{ISO} is the portion of the tensor that represents a uniform volume change. A positive M_{ISO} is an expansion or explosion, which may be a confined blast or rock bulking, while a negative M_{ISO} is a contraction or implosion. Implosion may indicate a pillar bursting, buckling, or rock ejecting into a void [24,32]. Isotropic components that are less than 10% of the whole moment tensor are generally deemed insignificant. The deviatoric tensor results in displacement with zero net volume change like the geological process of a fault dislocation. The general dislocation can be a mix of shear and normal dislocation [25]. To better understand the relative quantities of shear and normal displacements, the deviatoric component is divided into the DC and CLVD elemental sources, according to Knopoff and Randall [29]. The DC source, M_{DC} , is a pure shear mechanism. It is referred to as a double couple because there are two equal and opposite force couples, and the displacement pattern is the same for both force couples. As a result, there are two possible fault plane orientations that model the expected displacement equally well. Then, a pure DC source has two equal and opposite linear vector dipoles while the third dipole is zero [25,30]. This can be clearly illustrated in the elementary DC tensor in equation [3-4]. The CLVD, M_{CLVD} , source is a normal dislocation on a plane. The normal displacement from one linear vector dipole is compensated by opposing displacement from the other two linear vector dipoles, and thus, there is no net volume change. For a positive CLVD source, a single tensile dipole is compensated by two compressive dipoles and the inverse for a negative CLVD source [33]. That can be clearly portrayed in the elementary CLVD tensor in equation [3-4]. A pure CLVD source represents a Poisson's ratio of 0.5 [33], which has no geological meaning. However, it can make

sense for a mixed source event, such as an event with partial isotropic and CLVD components [34]. Microseismic events are normally represented by a combination of these three simple mechanisms. Thus, it is very important to decompose a seismic source event into standard forms of ISO, DC, and CLVD components to understand a complex event [35]. The moment tensor decomposition can be interpreted using the Hudson chart, which is a useful plot to display the moment tensor decomposition and to show the position of the source in the CLVD-ISO coordinate system. Figure 3-3 shows the Hudson chart, which is generated using mXrap software. It represents the relative proportions of ISO, DC and CLVD elemental sources. The vertical axis is the ISO component ranging from -100% (implosion) to +100% (explosion). The horizontal axis shows the CLVD component from +100 to -100%, which represents faulting on non-planar faults, with 100% DC at the center, which indicates pure shear faulting (0% ISO, 0% CLVD). The outer border of the chart is the 0% DC where pure tensile and compressive cracks are plotted [25,36].

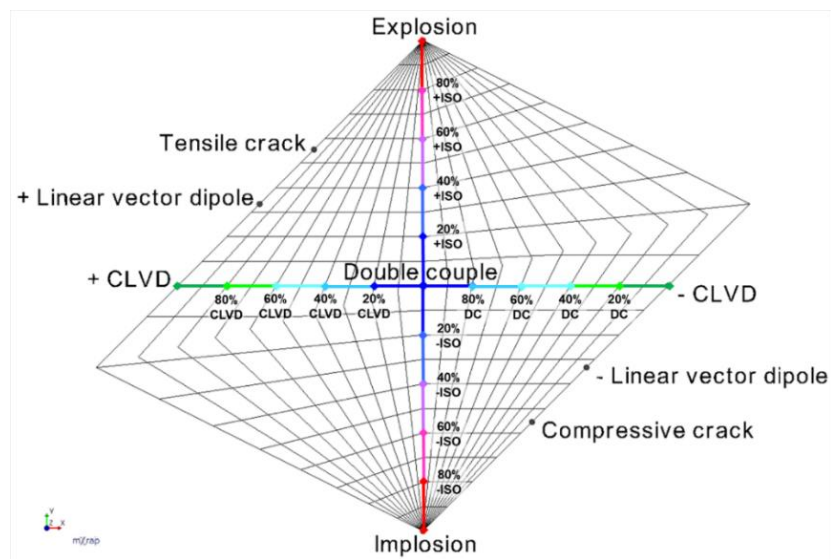


Figure 3-3. Hudson chart (after [37]).

3.3. Case study - Young-Davidson Mine

3.3.1 Mine location

Young-Davidson Mine is a gold mining operation located in northern Ontario near Matachewan town (Canada), as shown in Figure 3-4. The mine is owned and operated by Alamos Gold Inc. The orebody strike runs east-west with mineralization extending to depths of about 1,500 m [38].

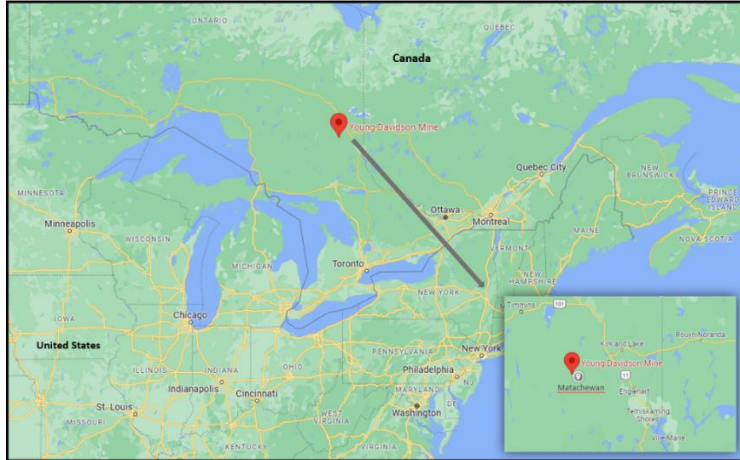


Figure 3-4. Location map of Young-Davidson Mine.

3.3.2 Mine geology

Young-Davidson property exists in the south-western part of the Abitibi Greenstone Belt. The mine lies within the Kirkland Larder Lake gold belt, which includes the world-class Kerr-Addison-Chesterville gold deposits and is intersected by the regional Larder Lake-Cadillac Fault Zone, known for its spatially associated gold camps. The property is hosted in a felsic intrusive syenite unit of about 1,420 m east-west by 470 m north-south. The Timiskaming Sediments are mainly the footwall rock type and are also found to be inter-bedded layers throughout the syenite rock mass. The hanging wall of the deposit is predominantly mafic volcanic, consisting of interbedded mafic flows and ultramafic flows. The gold mineralization is mostly related to quartz veins and disseminated pyrite mineralization, hosted in a felsic intrusive syenite unit. Several mineralized gold zones are hosted in the syenite. All lithologies are cut by late, generally northeast-trending Proterozoic diabase dikes, as shown in Figure 3-5 [38].

3.3.3 Site ESG seismicity monitoring system

As of December 2020, the seismic monitoring system used at the YD mine included 46 working sensors providing coverage for the production areas down to the 9305 level in the mine plan (1 km depth). The system includes 34 uniaxial sensors, eight triaxial sensors, three 4.5 Hz Strong Ground Motion (SGM) sensors underground, besides one 2.0 Hz SGM sensor on the surface. Instead of using a constant velocity model, a 3D Velocity Model that considers different lithology groups, paste-filled stopes and mined-out areas has been used and updated semi-annually since 2018. That

was very useful to improve source location accuracy. The mine consists of three main geological domains: host rock (Timiskaming sediments), diabase and syenite (ore), as shown in Figure 3-6.

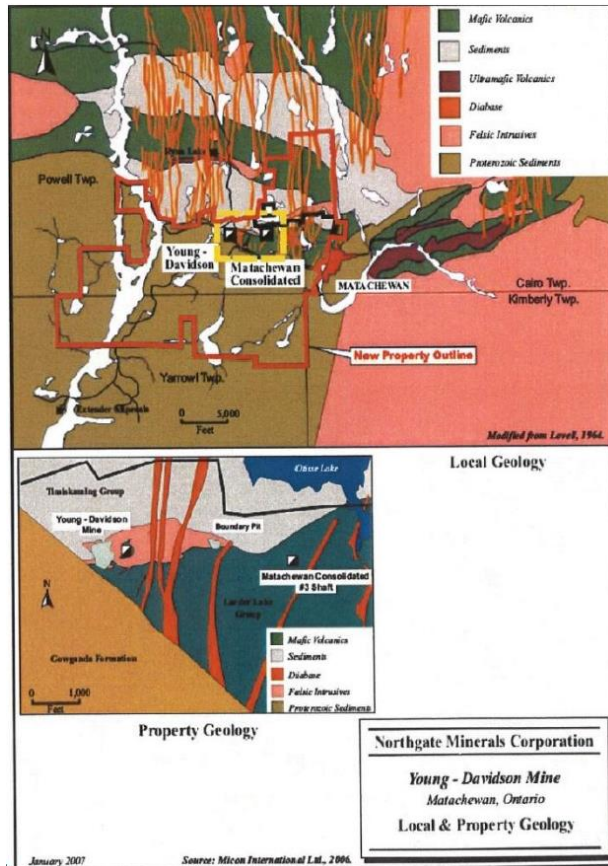


Figure 3-5. Local geology of the Young-Davidson Property [38].

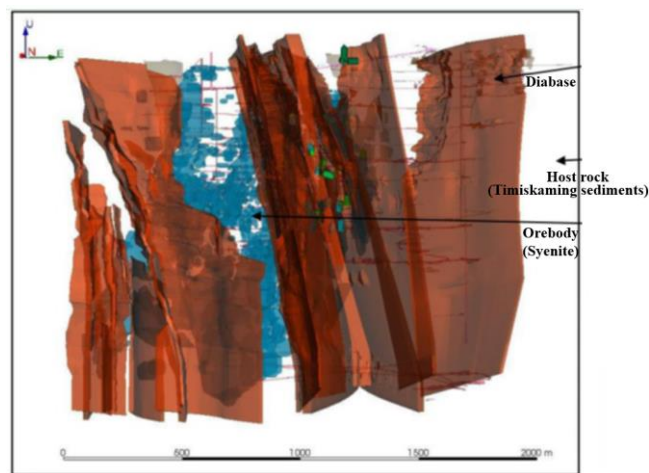


Figure 3-6. Three main geological domains in YD mine: Timiskaming sediments (host rock), diabase and syenite (ore) [39].

3.3.4 YD large events

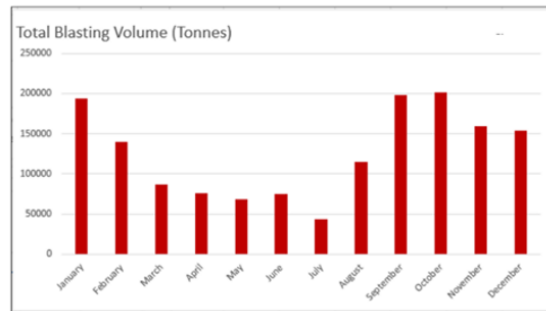
YD large events recorded from August 2018 to March 2021 are reported in Table 3-1. The large events are recorded by Canadian National Seismograph Network (CNSN) as the sensitivity and accuracy of the CNSN are relatively constant compared with the YD seismic monitoring system. This study will focus on $M_N 2+$ events YD mine experienced in 2020. As mentioned earlier, most large events occurred at depths of only 600-800 m below the surface. There is no apparent correlation between the increase of mining depth and seismic magnitude, which in turn suggests that those large events are likely driven by other factors like mining activities or geological structures, e.g., dykes intersecting the orebody.

Table 3-1. YD large events recorded by CNSN (2018.05-2021.03) [39].

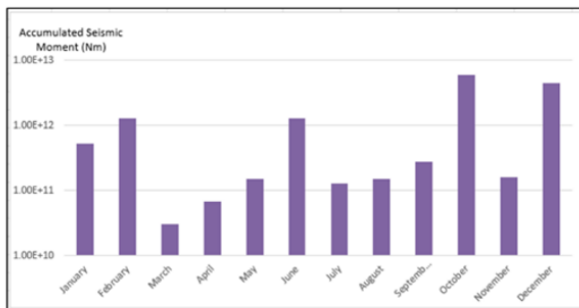
EST Time		Depth (Km)	Nuttli Magnitude, M_N
2018/08/12	19:40:34	0.8	1.6
2018/08/24	3:33:19	0.8	1.9
2018/09/10	16:44:54	0.5	2.2
2018/09/12	7:58:42	0.6	3.0
2018/09/12	10:02:07	0.6	2.2
2018/10/27	5:59:34	0.6	1.7
2018/11/12	12:01:50	0.5	1.9
2019/05/17	2:13:14	1.0	1.6
2019/09/19	4:53:20	0.7	2.6
2019/09/21	4:45:43	0.6	2.3
2020/02/20	7:09:32	0.3	2.2
2020/06/23	13:05:48	0.8	2.4
2020/10/21	16:31:29	0.8	1.7
2020/10/21	16:52:07	0.8	2.4
2020/10/30	12:44:04	0.8	2.2
2020/11/30	1:12:11	0.9	2.0
2020/12/02	17:38:26	0.6	2.4
2020/12/09	13:03:12	0.8	2.3
2020/12/18	5:37:02	0.7	2.0
2021/01/09	5:36:19	0.8	2.7
2021/01/19	6:03:04	0.8	2.5
2021/02/25	17:41:34	0.7	2.9
2021/03/03	4:11:08	0.9	2.3

3.4. Correlation between induced seismicity and mining production rate

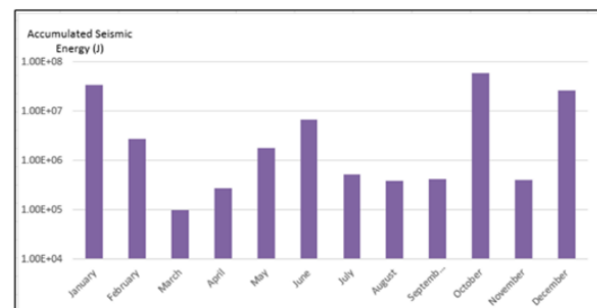
To identify the reasons beyond the large seismic events, the effect of the blasting volume on mine seismicity is analysed. Figure 3-7a shows the production blasting activity in 2020, where the blasting volume ranges from 40,000 to 200,000 tons per month, and the peak months are January, September, and October. Comparing the accumulated seismic moment represented in Figure 3-7b and accumulated seismic energy in Figure 3-7c with monthly blasting volume reveals that blasting affects the mine seismicity at some points as in January, October, and December. However, the peak accumulated seismic moment or energy does not always coincide with peak production blasting. In June, the low production rate is associated with a high seismic moment and high seismic energy, whereas in September, the high production rate resulted in relatively low seismic energy. Thus, it can be concluded that there is no apparent correlation between the accumulated seismic moment or energy and the monthly blasting volume in 2020.



(a)



(b)



(c)

Figure 3-7. Relation between mining production rate and recorded seismicity throughout 2020. (a) Total blasting volume. (b) Accumulated seismic moment. (c) Accumulated seismic energy.

3.5. b-value analysis

3.5.1 Variation in b-value with blasting distance from the dykes

To analyse the effect of the geological structures on seismicity, the variation in the b-value is investigated for the mining depth range of 700-900 m (levels 9600 to 9400). Figure 3-8 is a plan view showing the NE trending diabase dykes intersecting with the orebody at level 9470. Also, the four largest events that occurred around this depth level in 2020 are marked as yellow circles in Figure 3-8. The change in the b-value with the distance of the blasting from the dykes has been analysed in three different zones separated by two major dykes (dyke A and dyke B). The analysis is conducted separately in each zone as the stress conditions may be different. The b-values of blasting-induced seismicity west of dyke A are plotted in Figure 3-9a, whereas the b-values east of dyke B are shown in Figure 3-9b. The b-values recorded between dyke A and dyke B are plotted in Figure 3-9c. The dot colour on the charts indicates the blasting volume.

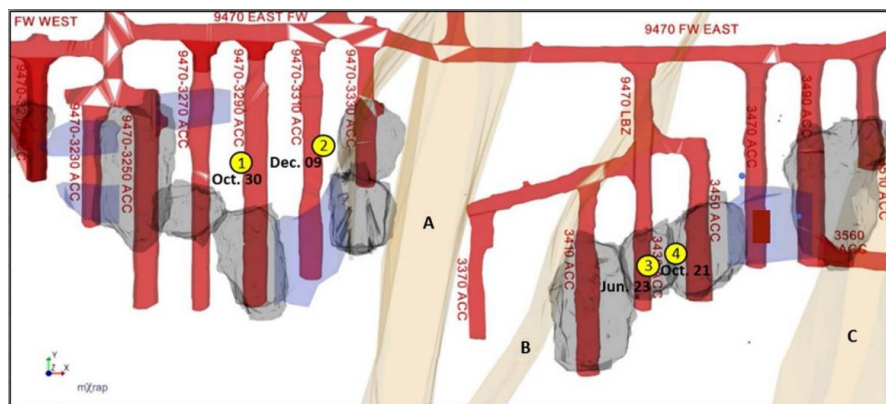


Figure 3-8. Plan view of level 9470 showing four largest events in 2020 between levels 9400 and 9600.

3.5.2 Discussion of b-value results

From Figure 3-9a, b-values close to dyke A are relatively high, with values greater than 1. This suggests that dyke A may not be the main contributor to the two large events (1) and (2) that occurred on October 30 and December 09 west of dyke A. Figure 3-9b shows that b-values are smaller east of dyke B, being lower than 1. This implies high stress condition and explains the occurrence of the two large events (3) and (4) on June 23 and October 21, respectively. Event (4) can be attributed to a large blast 10 m east dyke B with a corresponding b-value of 0.47. This is followed by another bigger blast on the same day 60 m east of dyke B that resulted in a significantly

higher b-value. Such high b-value may be explained by the stress relief due to rockmass damage that took place earlier after the first blast and triggered the large event (4). The low b-values 60 m east dyke B may be due to stoping activities causing local stress concentrations around the blasted areas after the December 22 and 26 blasts. Examining the influence of stope sequencing should provide more insight into the causative factors, however, it is not in the scope of the current work. Figure 3-9c shows that the zone between the two dykes is relatively stressed based on the low b-values obtained. It is noteworthy that the available database is not large enough to show definite trends based on b-values. Better representation of b-values would be achieved using more data from 2021 in the next step of this project.

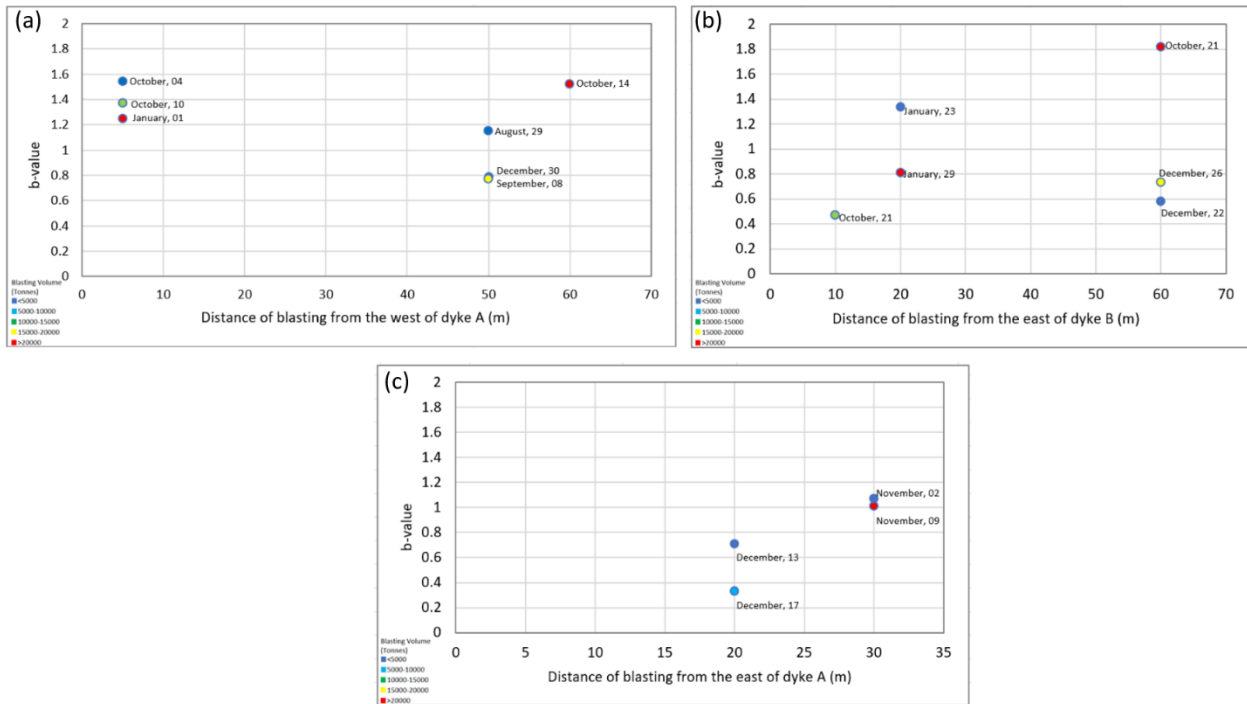


Figure 3-9. b-value results. (a) West of dyke A. (b) East of dyke B. (c) Between dyke A and dyke B.

3.6. Moment tensor inversion

3.6.1 Moment tensor inversion method

For the analysis of large events, moment tensor inversion is conducted using HybridMT software package developed in MATLAB for three events [40]. Full seismograms measured by the seismic acquisition system as well as accurate synthetic seismograms of the Earth (Green's function G) are

required for moment tensor inversion. Green's function computes the ground displacement recorded by the seismic sensor and describes all wave propagation effects, including the elastostatic response of the Earth. The ground motion response $u(t)$ at a station depends on $G(t)$. Thus, the moment tensor inversion is based on Equation [3-6]. When inverting this expression, the least-square method is often used for calculating the moment tensor as represented in Equation [3-7] [41].

$$U = G M \quad [3-6]$$

where M represents moment vector (6 x 1) composed of six independent components of the moment tensor, u is the (n x 1) vector representing observed amplitudes at sensors where n is the number of observed amplitudes for a given event, and G is the (n x 6) Green's function derivatives matrix, which represents the response of the medium from the source to the sensor. Equation [3-6] can be rearranged as follows:

$$M = (G^T G)^{-1} G^T u \quad [3-7]$$

The moment tensor inversion software Hybrid MT performs moment tensor inversion for earthquake data recorded by regional-to-local seismic networks. The algorithm inverts for unconstrained full, deviatoric, and double-couple constrained moment tensors using the first P-wave amplitudes. The amplitudes, rupture time, and polarity of the P-wave first motions are required as input data for the MT inversion. In addition, the location of the seismic network, as well as the velocity model, must be specified. The seismic parameters and graphical representations of the moment tensor are then calculated in the MATLAB environment [40].

3.6.2 Moment tensor inversion results

FMS results of each event decompose the seismic MT into its ISO and Deviatoric parts, including the CLVD and the DC components, following the decomposition introduced by Knopoff and Randall [29]. Also, the solution specifies the seismic moment and moment magnitude as well as the potential nodal planes of each event. The MT graphical representation (beach balls) is also generated, showing the best double-couple nodal lines, station locations on the focal sphere, and the location of pressure (P) and tension (T) axes [40]. The moment tensor decompositions in Table 3-2 show that the percentage of the DC component for the three events is less than 50%, indicating

that shear failure is not dominant in these events. On the other hand, the negative ISO components imply that the sources have encountered implosive deformation, a characteristic feature of compressional failure. As these events also show negative CLVD components, it is possible to infer that they are relevant to collapse. Table 3-2 shows that the source mechanisms are very close for the three events, and it is the most properly compressional failure, especially for events (1) and (2) where the deviatoric percentages are almost the same. Table 3-3 lists the resolved fault plane solutions derived from the DC component of the full moment tensor for the three events. Event (4) suggests a strike-slip fault that has nodal planes striking NNE-SSW and NNW-SSE, while events (1) and (2) suggest an oblique-thrust fault that has a reverse component of slip. Figures 3-10, 3-11, and 3-12 present the generated beachballs of the full, deviatoric, and double couple components for the events (1), (2), and (4), respectively.

Table 3-2. Moment tensor decompositions and source mechanisms reported for the three events.

Event	ISO%	CLVD%	DC%	M_w	Failure mechanism
Dec. 09	-19.9872	-42.9797	37.0331	2.4845	Compressional failure
Oct. 30	-19.0807	-42.2411	38.6782	2.4676	Compressional failure
Oct. 21	-23.9782	-53.5614	22.4604	2.0013	Compressional failure

Table 3-3. Fault plane solutions for the three events and corresponding fault types.

Event	Strike1	Dip1	Rake1	Strike2	Dip2	Rake2	Fault type
Dec. 09	100.92	63.89	129.39	219.11	46.06	37.68	Oblique-thrust fault
Oct. 30	100.19	67.21	131.84	213.58	46.62	32.20	Oblique-thrust fault
Oct. 21	134.66	83.78	-151.33	41.27	61.52	-7.08	Strike-slip fault

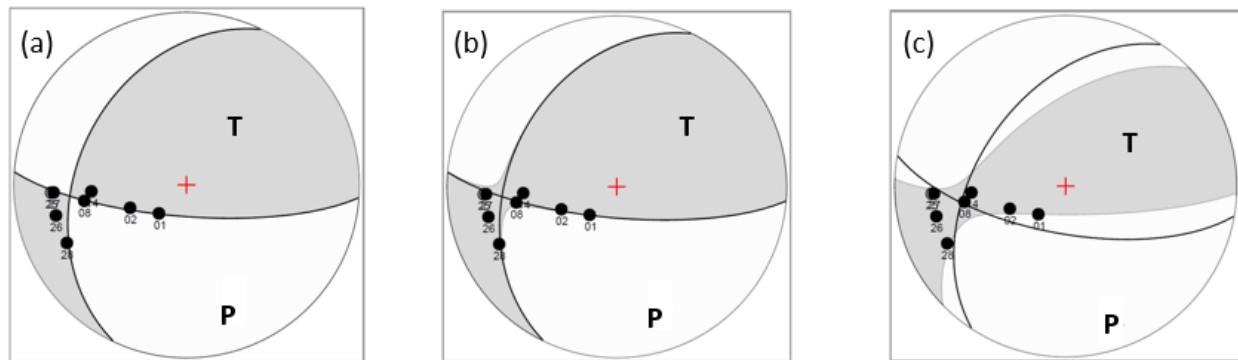


Figure 3-10. Generated beachballs from focal mechanism solution of the event (1). (a) DC component. (b) Deviatoric component. (c) Full tensor.

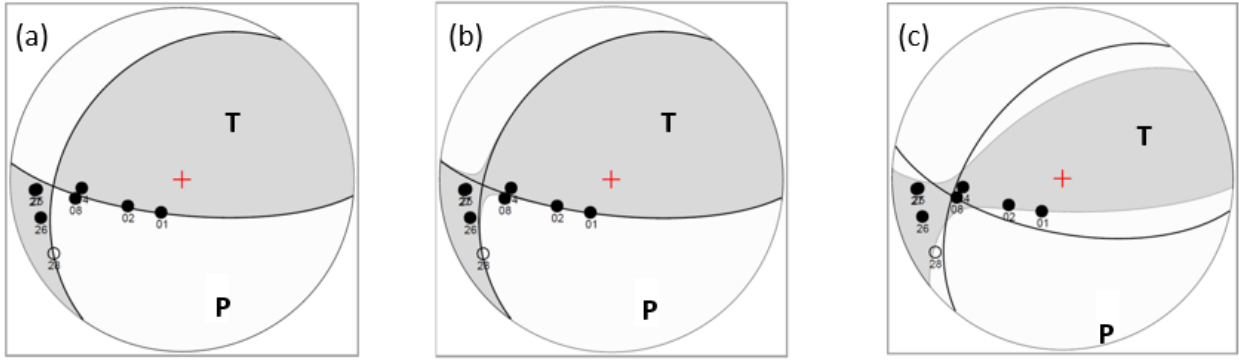


Figure 3-11. Generated beachballs from the focal mechanism solution of the event (2). (a) DC component. (b) Deviatoric component. (c) Full tensor.

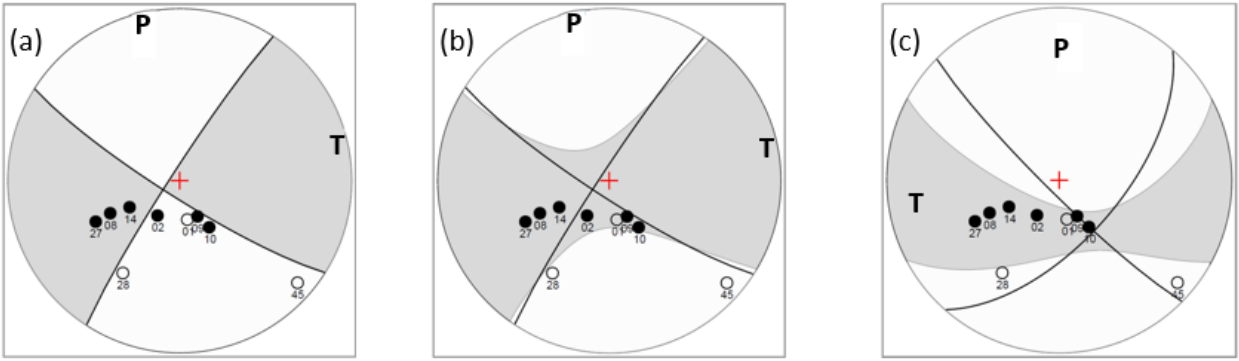


Figure 3-12. Generated beachballs from focal mechanism solution of the event (4). (a) DC component. (b) Deviatoric component. (c) Full tensor.

To further identify the source mechanisms of these events, the three seismic events are plotted on the Hudson source-type diagram, as shown in Figure 3-13. The events are clustered at the right-bottom quadrant of the Hudson diagram, and the locations indicate a compressional failure mechanism with a small part of shear. It is essential to point out that MT inversion is sensitive to the quality of the input data, sensor coverage and modelling assumptions. This includes polarity and amplitude reading biases for waveform data with low signal-to-noise ratios, synthetic waveform mismodeling due to a lack of insight into the medium (velocity model, rock anisotropy), and eventually site effects and sensor features (coupling, limited frequency band, polarity) [42]. Focal mechanism solutions help us better understand the root causes behind the large event, however, sensor coverage for the solved events cannot be considered ideal, as represented by the generated beachballs.

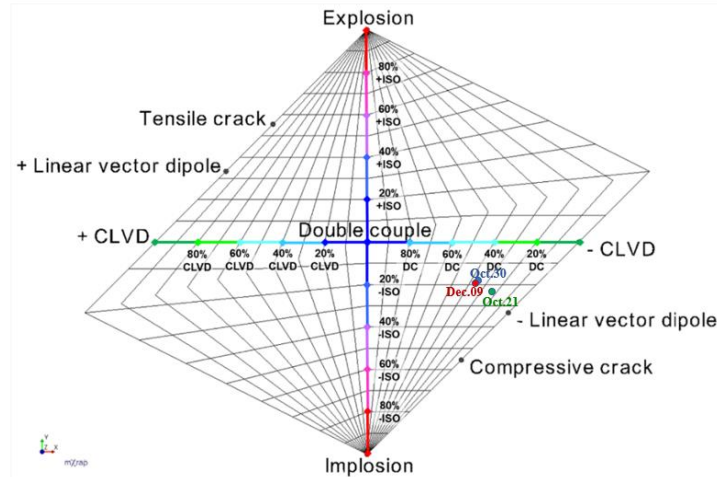


Figure 3-13. Hudson source-type plot of the three events 1, 2, and 4.

3.7. Effect of stoping sequence on the studied seismicity

To reveal the relation between induced seismic events and mining structure, the event locations and time with respect to stope sequencing have been analysed. Stope sequencing is bottom-up for each mining zone, and the plan calls for a 30 m sill pillar between mining zones. Late development on level 9560 (740 m below surface) due to low-grade material created a long sill pillar. Sill pillar recovery was implemented between levels 9590 and 9560. An increase in seismic activities was recorded during pillar recovery. Stopping breakthrough occurred at the 3330-easting, where stress can be re-distributed to the 3370-easting and outer abutments. The 9590 stopping progress is eastward. Figure 3-14 shows the planned stoping progression for the 9590 breakthrough [43]. Efforts were made to optimize stope sequencing to reduce significant stress redistribution after pillar yielding. However, the sequence was still accompanied by high seismic activities. Figure 3-15 shows four cross sections illustrating the stoping sequence in the studied level (9400e9600) toward the sill pillar, triggering large events (orange balls). Figure 3-15a depicts blasting in the period from October 21 to 30; it shows the location of the event (4). Figure 3-15b indicates that there was no blast from October 30 to November 02, yet it shows the occurrence of event (1). Figure 3-15c covers the sequence from November 02 to November 30. The last cross section (d) illustrates that there was no blast from November 30 until December 11 at this depth level, but a large event (2) occurred on December 09. It is worth noting that the analysed large events (1) and (2) happened while mining toward the sill pillar, which would explain the similar focal mechanism solutions for both events.

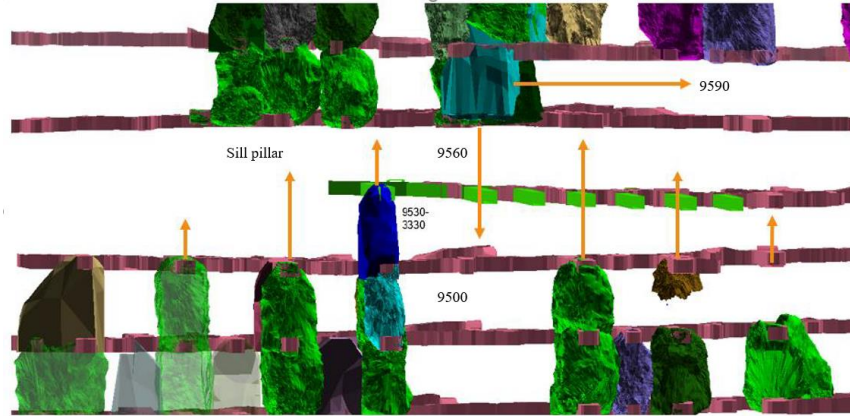


Figure 3-14. Planned stopping progression for the 9590 breakthrough [43].

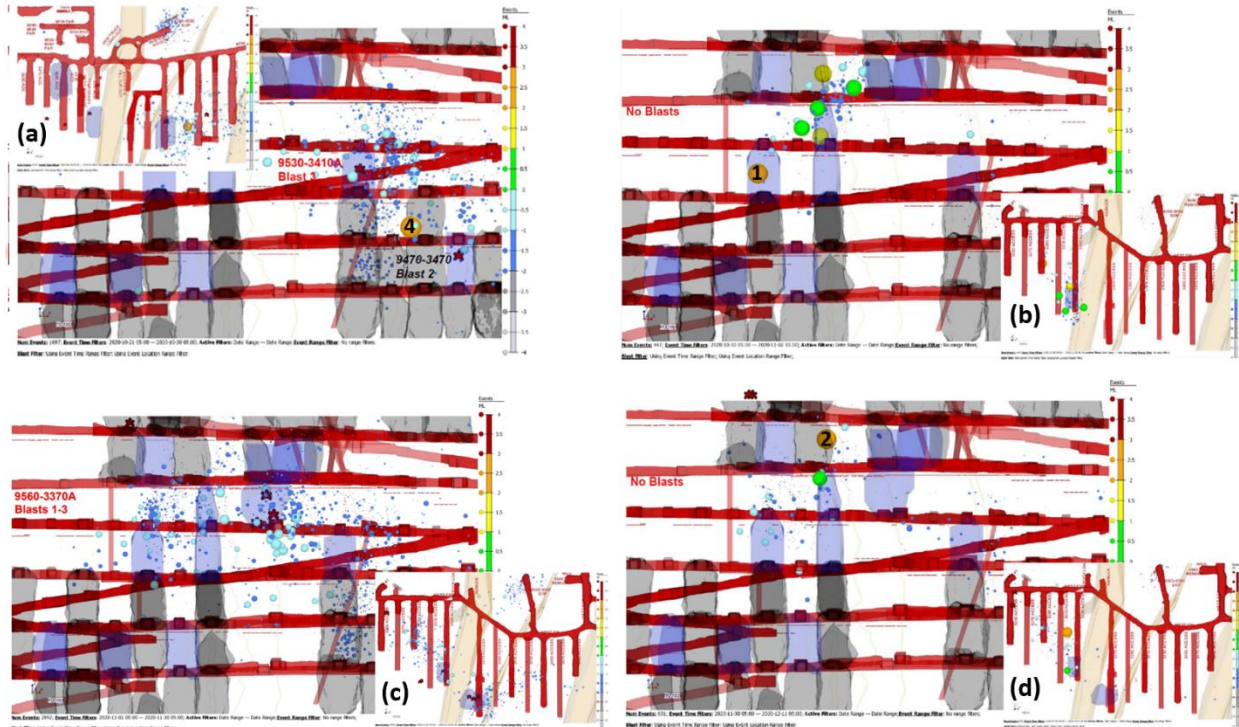


Figure 3-15. Mining sequence and large seismic events through levels 9400 to 9600 between October and December 2020. Note: Orange circles represent large events. (a) October 21 to 30 [event (4)]. (b) October 30 to November 02 [event (1)]. (c) November 02 to 30. (d) November 30 to December 11 [event (2)].

3.8. Conclusions

In this paper, a preliminary study of the micro-seismicity at the YD mine has been conducted to understand the root causes of the unusually strong seismic events recorded at shallow depths. The impact of blasting volume on accumulated seismic moment and energy was first investigated. It is

found that there is no apparent correlation between blasting volume and accumulated seismic moment or energy in the studied area. In addition, the stress regime of mining zones that intersected with regional dykes is studied by the b-value analysis through the mining levels 9400 to 9600. As for the zone east of dyke B, where two events (3) and (4) occurred, the analysis shows low b-values reflecting a highly stressed zone. Event (4) is likely triggered by large volume blasting, but more investigation is required to understand event (3) better. The b-values west of dyke A are quite high, indicating that the dyke is not the primary cause of the two major events (1) and (2). For further analysis, the moment tensor inversion was performed for three major events using HybridMT MATLAB code to reveal the event focal mechanisms. Focal mechanism solutions for three events, namely (1), (2), and (4), show almost the same failure mechanism, which is compressional failure. The percentage of DC components for the three events is less than 50%, indicating that shear failure is not prevalent in these events, whereas the negative ISO components indicate that the sources experienced implosive deformation, which is a characteristic feature of compressional failure. It is possible to infer that these events are relevant to collapse because they also show negative CLVD contributions. The possible mechanisms for the three events are further confirmed based on mining sequences. Events (1) and (2) occurred while mining toward the sill pillar, which demonstrates the consistency in their focal mechanism solutions. Thus, sill pillar recovery might be the main contributor to increased mining-induced seismicity. Studying the FMS for more events in future can provide additional information about the slip plane and help predict the trend of seismic hazards, which will be very useful in future mine planning and mine safety. While the findings from this research are specific to the case study of the YD Mine, they could be used to shed light on the causes of induced seismicity at other mines with similar conditions.

Ethical statement

The authors state that the research was conducted according to ethical standards.

Funding body

This research was funded by Natural Sciences and Research Engineering Council of Canada (NSERC), fund number 223079.

Conflict of interest

The authors declare no conflict of interest.

Acknowledgments

This work is financially supported by Natural Sciences and Research Engineering Council of Canada (NSERC) - Discovery Program Grant by Natural Sciences and Research Council of Canada. The authors wish to thank Alamos Gold Inc. for the co-operation and the support with the data of Young-Davidson Mine for this study.

References

- [1] Li T, Cai MF, Cai M. A review of mining-induced seismicity in China. *Int J Rock Mech Min Sci* 2007 Dec 1;44(8):1149e71. <https://doi.org/10.1016/j.ijrmms.2007.06.002>.
- [2] He S, Chen T, Vennes I, He X, Song D, Chen J, et al. Dynamic modelling of seismic wave propagation due to a remote seismic source: a case study. *Rock Mech Rock Eng* 2020 Nov; 53(11):5177e201.
- [3] Brown LG, Hudyma MR. Mining induced seismicity in Canada: a 2017 update. In: 52nd US rock mechanics/geomechanics symposium. OnePetro; 2018 Jun 17.
- [4] Lovchikov AV. Review of the strongest rockbursts and mining-induced earthquakes in Russia. *J Min Sci* 2013 Jul; 49(4):572e5.
- [5] Zhou XP, Qian QH, Yang HQ. Rock burst of deep circular tunnels surrounded by weakened rock mass with cracks. *Theor Appl Fract Mech* 2011 Oct 1;56(2):79e88. <https://doi.org/10.1016/j.tafmec.2011.10.003>.
- [6] Blake W, Hedley DG. Rockbursts: case studies from North American hard-rock mines. SME; 2003.

- [7] Ilieva M, Rudzinski Ł, Pawłuszek-Filipiak K, Lizurek G, Kudłacik I, Tondas D, et al. Combined study of a significant mine collapse based on seismological and geodetic data 29 January 2019, Rudna Mine, Poland. *Rem Sens* 2020 Jan; 12(10):1570. <https://doi.org/10.3390/rs12101570>.
- [8] Si G, Cai W, Wang S, Li X. Prediction of relatively high-energy seismic events using spatial-temporal parametrisation of mining-induced seismicity. *Rock Mech Rock Eng* 2020 Nov;53(11):5111e32.
- [9] He S, Song D, Mitri H, He X, Chen J, Li Z, et al. Integrated rockburst early warning model based on fuzzy comprehensive evaluation method. *Int J Rock Mech Min Sci* 2021 Jun 1; 142:104767.
- [10] Lurka A. Spatio-temporal hierarchical cluster analysis of mining-induced seismicity in coal mines using Ward's minimum variance method. *J Appl Geophys* 2021 Jan 1;184: 104249.
- [11] He S, Chen T, Song D, He X, Chen J, Li Z, et al. A new methodology for the simulation of tunnel rockburst due to far-field seismic event. *J Appl Geophys* 2022 Jul 1; 202:104651.
- [12] Wang J, Apel DB, Pu Y, Hall R, Wei C, Sepehri M. Numerical modeling for rockbursts: a state-of-the-art review. *J Rock Mech Geotech Eng* 2021 Apr 1;13(2):457e78.
- [13] Gibowicz SJ, Kijko A. An introduction to mining seismology. *Int Geophys Ser* 1994;55. iex.
- [14] Holub K. Predisposition to induced seismicity in some Czech coal mines. In: *Seismicity Associated with Mines, Reservoirs and Fluid Injections*. Basel: Birkhauser; 1997. p. 435 € e50. <https://doi.org/10.1007/s000240050086>.
- [15] Brown LG. Quantification of seismic responses to mining using novel seismic response parameters (Doctoral dissertation. Laurentian University of Sudbury); 2018.

- [16] Leake MR, Conrad WJ, Westman EC, Afrouz SG, Molka RJ. Microseismic monitoring and analysis of induced seismicity source mechanisms in a retreating room and pillar coal mine in the Eastern United States. *Undergr Space* 2017 Jun 1;2(2): 115e24. <https://doi.org/10.1016/j.undsp.2017.05.002>.
- [17] Gutenberg B, Richter CF. Frequency of earthquakes in California. *Bull Seismol Soc Am* 1944;34(4):185e8.
- [18] Hudyma MR. Analysis and interpretation of clusters of seismic events in mines. University of Western Australia; 2008 Nov.
- [19] Yu Q, Zhao D, Xia Y, Jin S, Zheng J, Meng Q, et al. multi-variate early warning method for rockburst monitoring based on microseismic activity characteristics. *Front Earth Sci* 2022 Jan 25:19. <https://doi.org/10.3389/feart.2022.837333>.
- [20] Xu NW, Dai F, Zhou Z. Study of characteristics of b value for microseismic events in high rock slope. *Chin J Rock Mech Eng* 2014;33(S1):3368e74.
- [21] Legge NB, Spottiswoode SM. Fracturing and microseismicity ahead of a deep gold mine stope in the pre-remnant and remnant stages of mining. In: 6th ISRM Congress. OnePetro; 1987 Aug 30.
- [22] Hudyma MR. Seismicity at Brunswick mining. In *Proceedings Quebec mining association ground control colloque*. Quebec: Val D'Or; 1995.
- [23] Cronin V. A draft primer on focal mechanism solutions for geologists. Texas. Baylor University; 2004. p. 14.
- [24] Ma J, Dong L, Zhao G, Li X. Focal mechanism of mining-induced seismicity in fault zones: a case study of yongshaba mine in China. *Rock Mech* 2019 Sep;52(9):3341e52. <https://doi.org/10.1007/s00603-019-01761-4>.

- [25] Dahm T, Krüger F. Moment tensor inversion and moment tensor interpretation. In New Manual of Seismological Observatory Practice vol. 2 (NMSOP-2) 2014 (pp. 1-37). Deutsches GeoForschungsZentrum GFZ. DOI:10.2312/ GFZ.NMSOP-2_IS_3.9.
- [26] Eyre ST, Van Der Baan M. Introduction to moment tensor inversion of microseismic events. GeoConvention 2015 May. <https://doi.org/10.1190/tle34080882.1>.
- [27] Julian BR, Miller AD, Foulger GR. Non-double-couple earthquakes 1. Theory. Rev Geophys 1998 Nov;36(4):525e49. <https://doi.org/10.1029/98RG00716>.
- [28] Sîlený J, Milev A. Source mechanism of mining induced seismic events resolution of double couple and non-double couple models. Tectonophysics 2008 Aug 1;456(1e2):3e15. <https://doi.org/10.1016/j.tecto.2006.09.021>.
- [29] Knopoff L, Randall MJ. The compensated linear-vector dipole: a possible mechanism for deep earthquakes. J Geophys Res 1970 Sep 10;75(26):4957e63. <https://doi.org/10.1029/JB075i026p04957>.
- [30] Vavrycuk V. Moment tensor decompositions revisited. J Seismol 2015 Jan;19(1):231e52. <https://doi.org/10.1007/s10950-014-9463-y>.
- [31] Tape W, Tape C. A geometric setting for moment tensors. Geophys J Int 2012 Jul 1;190(1):476e98. <https://doi.org/10.1111/j.1365-246X.2012.05491.x>.
- [32] Malovichko D, van Aswegen G, Clark R. Mechanisms of large seismic events in platinum mines of the Bushveld Complex (South Africa). J S Afr Inst Min Metall 2012 Jun; 112(6):419e29.
- [33] Lay T, Wallace TC. Modern global seismology. Elsevier; 1995 May 18.
- [34] Eaton DW. Microseismic focal mechanisms: a tutorial, vol. 20. Calgary, Alberta: CREWES Research Report; 2008. p. 1. 1.

- [35] Krieger L, Heimann S. MoPaD-moment tensor plotting and decomposition: a tool for graphical and numerical analysis of seismic moment tensors. *Seismol Res Lett* 2012 May 1;83(3):589e95. <https://doi.org/10.1785/gssrl.83.3.589>.
- [36] Tierney S. Moment tensors e a practical guide, blog post, 2019. Perth, Western Australia: Australian Centre for Geomechanics, The University of Western Australia; 2015. Figure generated by Harris, PH & Wesseloo, J, mXrap soft-ware, version 5, <https://mxrap.com/moment-tensors-a-practical-guide>. <https://mxrap.com>.
- [37] Hudson JA, Pearce RG, Rogers RM. Source type plot for inversion of the moment tensor. *J Geophys Res Solid Earth* 1989 Jan 10;94(B1):765e74. <https://doi.org/10.1029/JB094iB01p00765>.
- [38] Alamos Gold Inc. Mines and projects. Retrieved September 14th, 2015, from Alamos Gold: <http://www.alamosgold.com/mines-and-projects/producing-mine/Young-Davidson/>.
- [39] Alamos Gold Inc. Seismic risk management plan. 2021.
- [40] Kwiatek G, Martínez-Garzon P, Bohnhoff M. HybridMT: a MATLAB/shell environment package for seismic moment tensor inversion and refinement. *Seismol Res Lett* 2016 Jul 1; 87(4):964e76. <https://doi.org/10.1785/0220150251>.
- [41] Ren Y, Vavrycuk V, Wu S, Gao Y. Accurate moment tensor inversion of acoustic emissions and its application to Brazilian splitting test. *Int J Rock Mech Min Sci* 2021 May 1; 141:104707. <https://doi.org/10.1016/j.ijrmms.2021.104707>.
- [42] Sellers EJ, Kataka MO, Linzer LM. Source parameters of acoustic emission events and scaling with mining-induced seismicity. *J Geophys Res Solid Earth* 2003 Sep;108(B9). <https://doi.org/10.1029/2001JB000670>.
- [43] Alamos Gold Inc. Ground control management plan. 2020.

Bridging text between manuscripts

In the first part of the study, reported in Chapter 3, the causes behind large seismic events that occurred at shallow depths in YD mine are discussed. At such shallow depth, it is unlikely that the intersecting dyke is the main reason for the addressed events. On the other hand, the location of the seismic events as well as their moment tensor solutions proved that the sill pillar is the main contributor to the mine seismicity leading to high stress environment. The three events had high negative ISO and CLVD components indicating that the sources have experienced implosive deformation.

It is necessary to discuss the uncertainty of the resultant moment tensor solutions. Uncertainty can be estimated by two methods namely the normalized root mean square (RMSERROR) and the bootstrap resampling test. RMSERROR describes the error between the observed (U^{obs}) and predicted (U^{th}) amplitudes at the available N sensors as follows (Stierle et al., 2014; Kwiatek et al. 2016; Gnyp and Malytskyy, 2021).

$$RMS = \sqrt{\frac{\sum_{i=1}^N (U_i^{obs} - U_i^{th})^2}{\sum_{i=1}^N (U_i^{obs})^2}} \quad [B2-1]$$

Table B2.1 below shows the values of the calculated RMSERROR of the three studied events discussed in chapter 3.

Table B2-1. RMSERROR values of Dec 09, Oct 30, and Oct 21 seismic events.

Event	RMSERROR
Oct 30, 2020	0.4468
Dec 09, 2020	0.2477
Oct 21, 2020	0.3395

In the bootstrap resampling test with MATLAB, a certain percentage of randomly selected polarities is reversed as if such polarities were wrongly picked (Kwiatek et al. 2016). Thus, 100 resampling tests of the original data were performed while 1% of the input polarity is reversed. Figures B2.1, B2.2, and B2.3 show the bootstrap resampling test results for the events Oct 30, Dec 09, and Oct 21, 2020, respectively.

The error estimated from both methods and poorly constrained solutions can be attributed to limitations of the input data. Optimal solution requires sufficient sensor coverage around the source, however, YD mine needs to expand the current sensor network in the western and lower parts of the mine for better coverage and more satisfactory results. In underground mines, drift (tunnel) locations are dictated by the shape and proximity to the orebody. For these reasons as well as budgetary constraints, complete sensor coverage is difficult to achieve sometimes. Besides, low quality data from some sensors was discarded due to the lack of assurance in the polarity. Therefore, we could only use a minimum number of eight phases in the inversion for the three events.

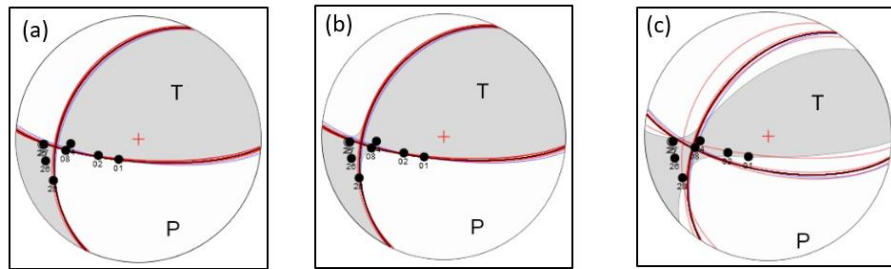


Figure B2-1. Result of the bootstrap resampling test for event Oct 30, 2020. (a) DC component. (b) Deviatoric component. (c) Full tensor.

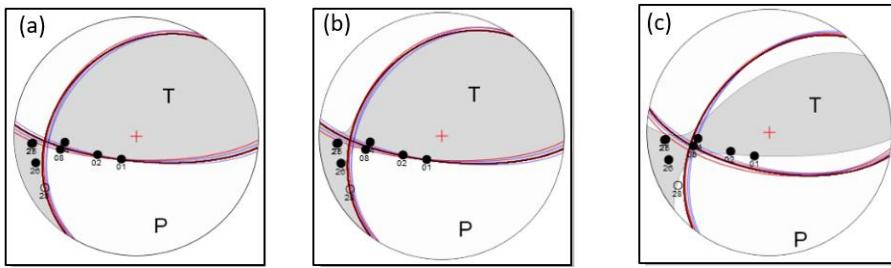


Figure B2-2. Result of the bootstrap resampling test for event Dec 09, 2020. (a) DC component. (b) Deviatoric component. (c) Full tensor.

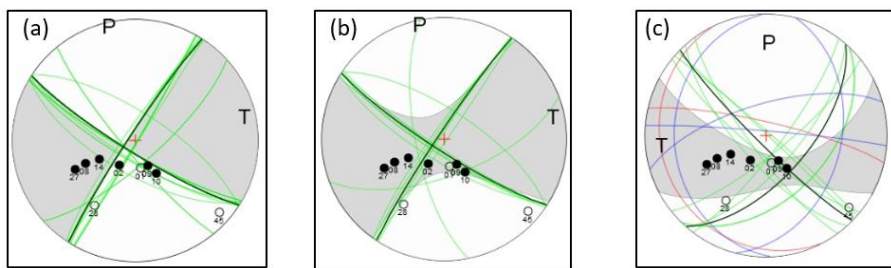


Figure B2-3. Result of the bootstrap resampling test for event Oct 21, 2020. (a) DC component. (b) Deviatoric component. (c) Full tensor.

More information regarding the performed steps to calculate b-value and moment tensor solutions can be found in Appendix A.

The second step of the study focuses on analyzing the root causes behind large seismic events that occurred in the lower mine zone with mining advance. Given the low confidence in HybridMT results, due to limitations in the available data, ESG HSS software was used for moment tensor inversion in subsequent analysis (Chapter 4). Moreover, a 3D numerical model has been generated with finite difference software FLAC3D considering the intersecting dykes, to simulate the induced stress distribution according to the mining sequence. Qualitative assessment has been conducted using Hoek-Brown compressional safety factor, brittle shear ratio, and burst potential index. All results are compared to the seismic source locations and mechanisms to better understand the seismic behavior in the lower mine zone.

Erratum: In Section 3.6.1, the term “rupture time” should read “rise time”.

Chapter 4 – Analysis of Seismicity in Lower Mine Zone

4.1 Introduction

In this chapter, a mine-wide numerical model is constructed in finite difference software FLAC3D of Itasca Ltd (Itasca, 2009). The model takes into consideration the northeast-trending diabase dykes to simulate mining-induced stress distribution per the mine plan of primary and secondary stope extraction. In-situ stress measurement previously conducted at the mine are analyzed and used to generate the model. Assessment of stress distribution, brittle shear ratio, and strain energy as well as comparison with seismic source location, magnitude, and mechanism are presented. Moment tensor inversion of seismic events of magnitude M_w 2.0+ that have been observed in the deeper mine zone is carried out to identify the mechanisms of rock failure using HSS Advanced software. This helps understand the influence of mining activities and geological structures on seismicity as mentioned before. This work involves mining, geologic, geotechnical, and seismic data collection and analysis as well as 3D mine-wide numerical modelling.

4.2 Numerical modelling

Mining activity and ore extraction in underground mines provide a high stress environment that may lead to drastic rock failure in the mining area. As computer technology advances with time, numerical simulation analysis has become affordable and crucial to analyze the behavior of rock damage brought on by stress redistribution and blasting activities in underground mines (Chen et al., 2017 and Yang et al., 2015). It can be used to determine whether a sill pillar in a tabular orebody has the potential to undergo rockburst (Castro et al., 2012).

4.3.1 Methodology

A mine-wide numerical model is generated in FLAC3D considering the diabase dykes and in-situ stress measurements. FLAC3D is an explicit finite difference algorithm for numerical simulation of the mechanical behavior of continuous, deformable media with different material types, structures, and complex geometries (Itasca, 2009). The raw mining geometry, surveyed stope geometry, and dykes, are initially fixed and simplified using the Rhino 3D CAD software to

produce the FLAC3D model geometry. Rhino feeds its output CAD file to Griddle^{2.0}, Itasca's grid generation plug-in software, to refine and merge overlapped meshes into a conforming one. Mesh refinement is needed to generate user-defined mesh sizes. Within the regions of interest, a denser mesh is used, and it gets less dense away from the orebody towards the model boundaries. Figure 4-1 shows the 3D volumetric mesh generated using Griddle^{2.0} for FLAC3D^{7.0}. Figure 4-2 shows the model layout. It contains 770,229 grid points, 4,554,815 zones and 1,404 zone groups.

Linear elastic analysis is conducted. The results are examined in terms of compressive stress factor of safety (FS), brittle shear ratio (BSR), and burst potential index (BPI). A qualitative analysis is carried out to assess mining induced seismicity in the lower-mine zone.

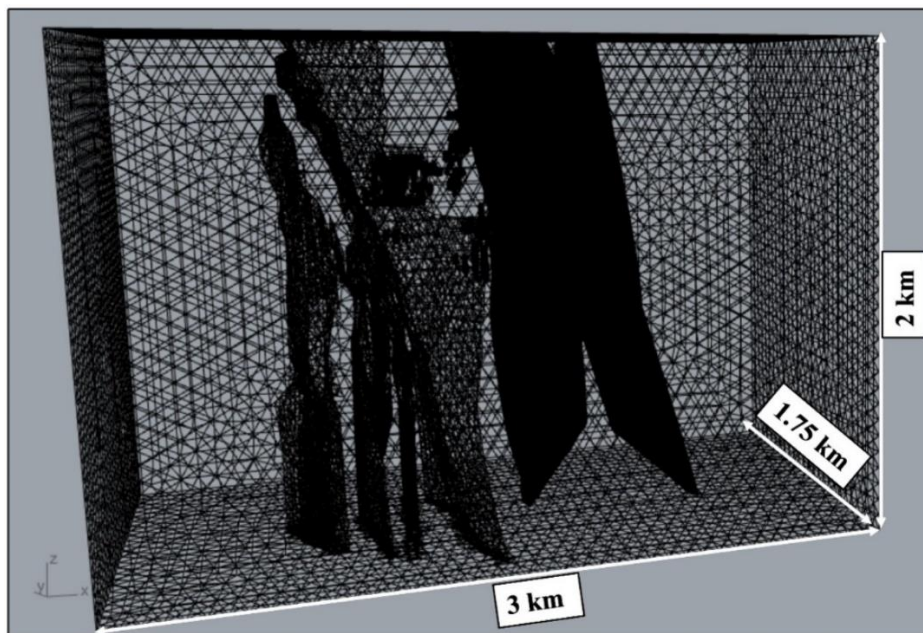


Figure 4-1. 3D volumetric mesh generated using Griddle2.0 for FLAC3D7.0. All excavations and dykes mesh are fixed, merged, and refined with the appropriate size.

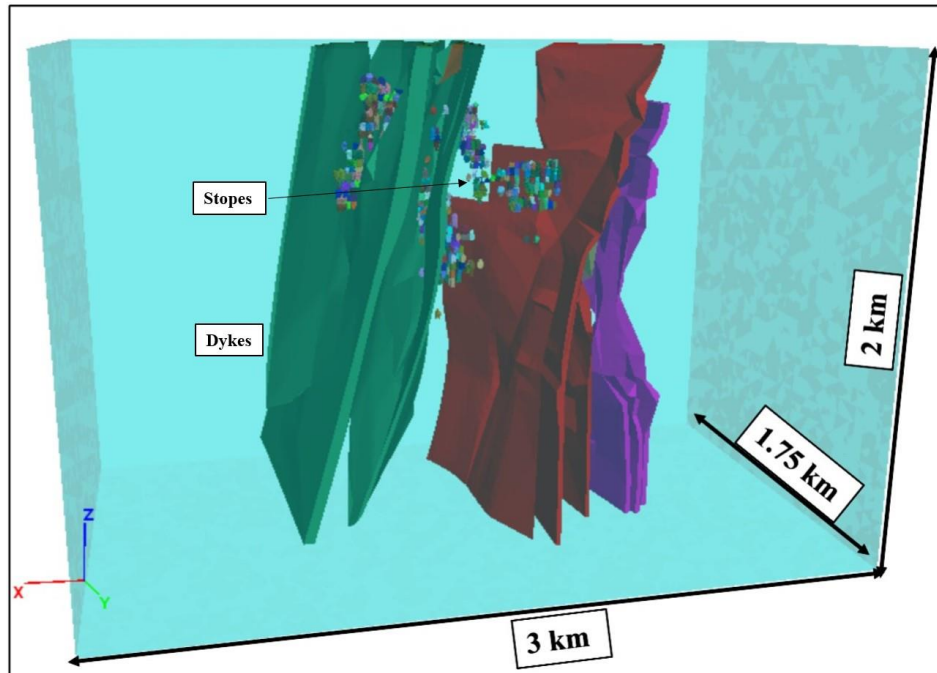


Figure 4-2. FLAC3D Model Layout.

4.3.2 Mining Sequence

The general sequence plan in YD mine includes three critical areas namely stoping blocks below 9440 (lower mine zone), west mining zone 9590-9800 (upper mine and upper mid mine zones), and the 9440-9590 central/eastern stoping blocks (lower mid mine zone) (Alamos Gold Inc., 2020). The model includes the three zones of the mining sequence: upper, mid, and lower mine. The area of interest in this analysis is the lower mine zone from level 9440 (around 900 m) to level 9095 (1200 m) where events of magnitude M_w 2.0+ have been observed. Mining blocks below 9440 starts from 9305 in the last half of 2020. All mined stopes before the lower mine zone have been excavated in one step to accelerate modelling calculations. Then, the lower mine zone is mined step by step according to the mining sequence of YD Mine from August 12th, 2020, to April 22nd, 2022, considering the stopes mined out during this period in the lower mid-mine zone. Mining and backfilling are simulated in 82 stages (Figure 4-3).

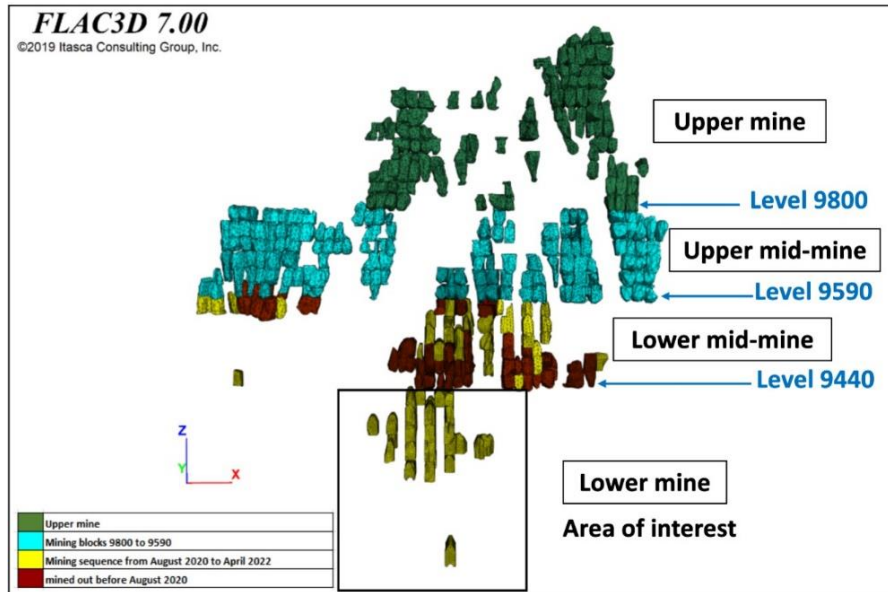


Figure 4-3. The general sequence in YD mine includes the three critical zones, stoping blocks below 9440, west mining zone 9590-9800, and the 9440-9590 central/eastern stoping blocks.

4.3.3 Rockmass properties

As mentioned in chapter 3, the Timiskaming sediments are mainly the footwall rock type and are also found to be inter-bedded layers throughout the syenite rock mass. The hanging wall of the deposit is predominantly mafic volcanic consisting of inter-bedded mafic flows and ultramafic flows. Several mineralized gold zones hosted in the syenite and all lithologies are cut by northeast-trending diabase dikes (Alamos Gold Inc., 2015).

The Rock Quality Designation index (RQD), introduced by Deere in 1964, is used to assess the quality of rocks in the mining industry. It is estimated as the percentage of core runs made of intact pieces exceeding 10 cm (Abzalov, 2016). Rock Mass Rating (RMR) (Bieniawski, 1973, 1976) and Rock Quality Index (Q-index) (Barton et al. 1974) are the most common methods used for rockmass classification. When calculating the Q index, in situ factors including RQD, the number of joint sets, joint condition, groundwater, and stress state are considered.

$$Q = \frac{RQD}{J_n} \times \frac{J_r}{J_a} \times \frac{J_w}{SRF} \quad [4-1]$$

Where: J_n = the number of joint sets, J_r = joint roughness number, J_a = joint alteration number, J_w = joint water factor and SRF = stress reduction factor.

The geological strength index (GSI) proposed by Hoek et al. (2000) can be estimated from the Q index of Barton et al. (1974) as follows.

$$GSI = 9 \ln Q + 44 \quad [4-2]$$

where Q is calculated by assuming J_w and SRF are equal to 1 (Zhang, 2017; Hoek et al., 2000). These assumptions are reasonable when applying the classification system to the numerical design since SRF equal to 1 means that the rockmass is somewhat clamped but not too stressed so in situ stress can be addressed. Also, J_w equal to 1 represents dry condition which is most common in underground mining.

Table 4-1 presents a summary of the RQD observed at Young-Davidson, joint sets number, and joint condition (Alamos Gold Inc., 2020). Rockmass characterization systems; GSI and Q index, are then used to delineate rockmass properties for numerical modelling using RSData software by RocScience (Table 4-2). To simplify model geometry, TSED, SYN, and MAFIC units have been combined as one material to be referred to as YD_{ave} and the average parameters per each domain used as the input parameters in the model (Table 4-3).

Table 4-1. Summary of the RQD observed at Young-Davidson, joint sets number, joint condition (Alamos Gold Inc., 2020), and the calculated Q index and GSI.

Domain	RQD	J_n	J_r	J_a	Q	GSI
TSED (FW)	84	12	1.7	1.1	10.8	65.41
SYN (Ore)	88	15	1.7	1.3	7.67	62.33
MAFIC (HW)	80	12	1.5	1.3	7.69	62.35
DIA (All)	74	12	1.3	1.3	6.16	60.36

Table 4-2. Summary of Rock Unit Properties (Alamos Gold Inc., 2020), and the calculated rockmass parameters using RSDData software by RocScience.

Domain	GSI	UCS (MPa)	Poisson's ratio	Young's modulus E_i (MPa)	Unit weight (MN/m ³)	m_i	m_b	s	a
TSED (FW)	65.41	155	0.25	69000	0.02730	5.5	1.599	0.0214	0.502
SYN (Ore)	62.33	142	0.27	70000	0.02696	7.5	1.953	0.0152	0.502
MAFIC (HW)	62.35	99	0.26	70000	0.02925	4.9	1.277	0.0152	0.502
DIA (All)	60.36	175	0.24	91000	0.02955	5.0	1.214	0.0122	0.503

Table 4-3. The average rock material properties (after MD Eng report, 2017).

Domain	UCS (MPa)	Density (Kg/m ³)	Poisson's ratio	Young's modulus E_r (GPa)	m_b	s	a
YD _{ave}	150	2760	0.26	40	1.61	0.0173	0.502
DIA	175	2980	0.24	48	1.214	0.0122	0.503
FILL	-	1600	0.25	250	-	-	-

4.3.4 In-situ Stress

To build a calibrated model, a series of numerical simulations was performed based on previous in-situ stress measurements and estimation of in-situ stress magnitude and orientation that has been done by McGill using diametrical core deformation technique (DCDT) (Li, 2021; Li and Mitri, 2022). In-situ stress measurements were conducted at Young-Davidson on four levels: 9800 (556 m) and 9590 (766 m) by Mirarco Mining in 2012 and further measurements were taken at 9740 (616 m) and 9440 (916 m) in 2016. Table 4-4 presents a summary of the in-situ stress measurements done in YD mine (MD Eng., 2017). Core deformation technique is conducted on level 9130 (around 1170 m) where rock samples were extracted from two boreholes for stress analysis.

Figure 4-4a reveals that the vertical stress exerted by gravitational loading generally agrees with the measured minor principal stress (σ_3). In situ stress data from the nearby Macassa Mine, where testing has been completed at depths greater than at Young-Davidson, shows quite high horizontal

to vertical stress ratios compared to empirical data (Alamos Gold Inc., 2020) as shown in Figure 4-4b. McKinnon and Lebric (2006) found that in the region the stress is rotated 035° (Figure 4-5). The core deformation analysis suggests high differential stress ($\sigma_1 - \sigma_3$) at level 9130 which agrees with the stress measurements done at level 9440 and the in-situ stress data from Macassa Mine as well. It also confirmed the stress orientation as well as McKinnon and Labrie (2006).

The average stress orientation of YD Mine measurements has been used in this study; however, the three principal stresses are observed to not be perpendicular to one another (Figure 4-6a). The major principal stress was found to be in the northeast trend which agrees with the regional stress orientation and core deformation analysis results. Thus, the averaged orientation of the major principal ought to be consistent and then, in accordance, the intermediate and minor principal stresses are adjusted (Figure 4-6b). The average in-situ stress values that are used in this study can be represented as follows (Li, 2024).

$$\sigma_1 = -0.065 X + 677.84 \quad [4-3]$$

$$\sigma_2 = 0.0028 X + 6.39 \quad [4-4]$$

$$\sigma_3 = 0.0028 X - 47.72 \quad [4-5]$$

Where σ_1 , σ_2 , and σ_3 are the major, intermediate, and minor principal stresses at level X. Averaged principal stress orientations of σ_2 and σ_3 were adjusted to become mutually orthogonal with σ_1 . As the adjusted in-situ stress orientations are not parallel to the cartesian frame of reference of the FLAC3D model, in-situ stress transformation was needed (Li, 2024). The resulting in-situ stress field was then initialized in FLAC3D.

Table 4-4. Stress measurements at Young-Davidson Mine (after Mine Design Engineering, 2017).

P. Stress	9800 Level		9740 Level		9590 Level		9440 Level	
	Magnitude	Orientation/ Incline	Magnitude	Orientation/ Incline	Magnitude	Orientation/ Incline	Magnitude	Orientation/ Incline
σ_1	43±10	041/15	51±7	063/25	35±9	001/16	74±3	331/57
σ_2	30±16	133/06	41±5	079/-17	27±4	270/02	35±4	183/29
σ_3	18±5	245/74	29±3	152/-32	20±7	173/74	20±1	085/15

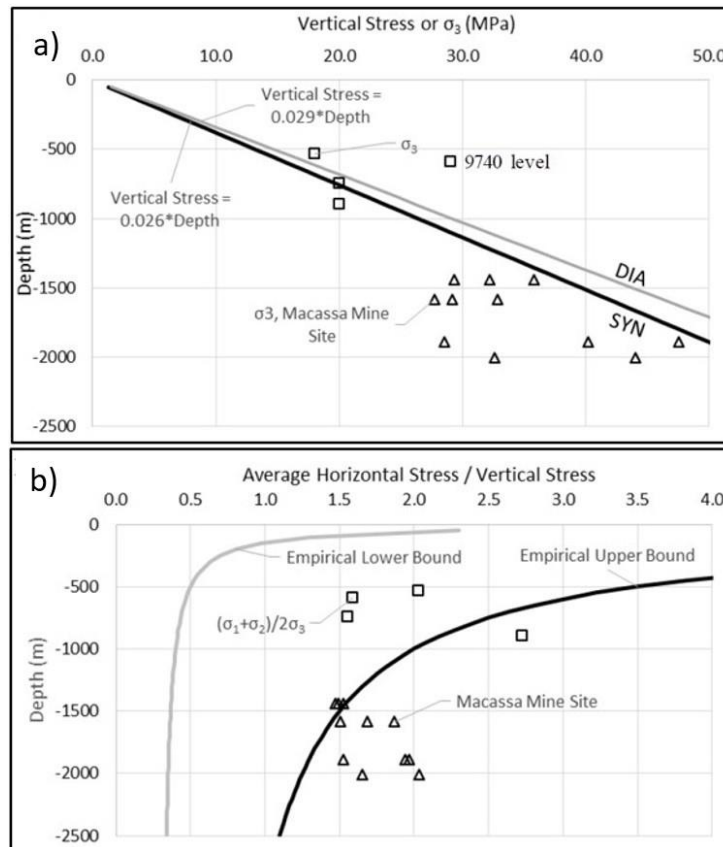


Figure 4-4. Stress conditions at YD Mine (MD Eng., 2017- b) after Hoek and Brown 1980).

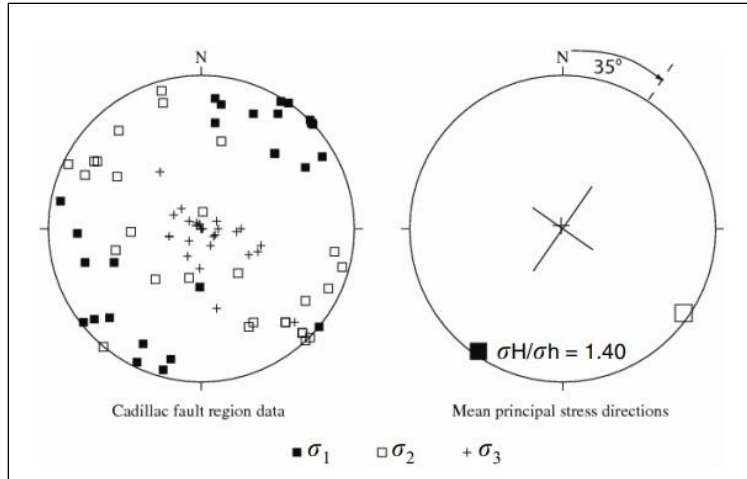


Figure 4-5. Principal stress axes from Cadillac Fault mine database (McKinnon and Lebric, 2006).

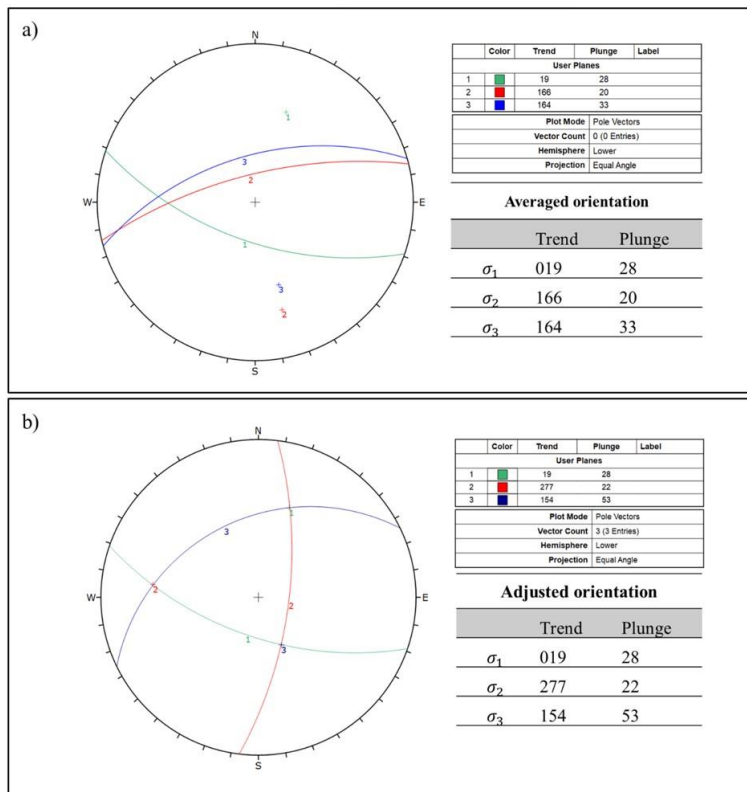


Figure 4-6. In-situ stress orientation in YD mine where a) and b) represent the measurements' averaged and adjusted orientations respectively.

4.3.5 Results and Discussion

As mentioned in section 5.2.2, the three mining zones: upper, middle, and lower mine zones, are included in the model with the intersecting dykes. Lower mine zone starting from level 9440 is the

focus of this investigation. All stopes mined before the lower mine zone have been excavated in one step then the mining sequence was adopted step by step. Mining and backfilling are simulated in 82 stages. Qualitative analysis is carried out to analyze mining seismicity in the deeper mine zone using the maximum compressive stress, brittle shear ratio (BSR), and burst potential index (BPI).

4.2.5.1 Maximum compressive stress

Mining activities affect the induced stresses in the mining vicinity and create stress concentration zones which affect the stability of the stopes, and the ore blocks that will be mined as mining progresses. Figure 4-7 shows a plan view at level 9360 representing the maximum compressive stress values around excavations mined out at stages 9, 16, 22, 33, 36, 47, 51, 60, and 73. In FLAC3D, compression is negative, and tension is positive. The maximum principal stress is observed to be aligned with NE-SW direction which compares very well with the stress measurements discussed in section 4.2.4. As a result, the maximum compressive stress values are found to reach 90 MPa at the NW and SE excavation corners (Mitri et al., 2000) and stress concentration zones can be observed in the transverse pillars, i.e., future secondary stopes.

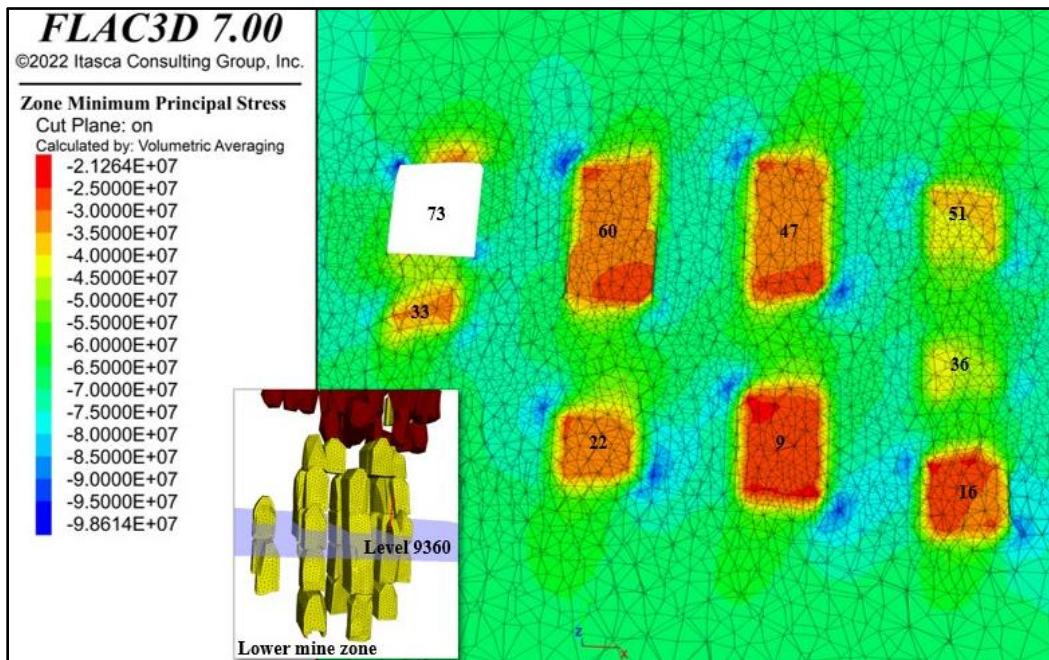


Figure 4-7. Plan view at level 9360 including the maximum compressive stress values around excavations mined out at stages 9, 16, 22, 33, 36, 47, 51, 60, and 73.

As mentioned above stress concentration areas are more prone to decrease stability. If the mining zone is under compression, potential of compressional failure can be evaluated using the Hoek–Brown safety factor (SF). Hoek–Brown compressive safety factor can be determined by dividing the value of Hoek–Brown maximum principal stress at failure (Hoek et al, 2002) by the maximum principal induced stress at each zone in the model (Heidarzadeh et al., 2020).

$$SF = \frac{\sigma_3 + \sigma_{ci} \left(m_b \frac{\sigma_3}{\sigma_{ci}} + s \right)^a}{\sigma_1} \quad [4-6]$$

Where, m_b , s , and a are rock mass material constants, σ_{ci} is the uniaxial compressive strength of the intact rock material. A more realistic estimate of the safety factor can be obtained by calculating strength and applied stress from the hydrostatic line where $\sigma_1 = \sigma_3$. In the present analysis, it is simplified by subtracting the value of the minimum principal induced stress from the Hoek–Brown maximum principal stress at failure and from the maximum principal induced stress at each zone in the model (Figure 4-8) as follows.

$$SF = \frac{\left[\sigma_3 + \sigma_{ci} \left(m_b \frac{\sigma_3}{\sigma_{ci}} + s \right)^a \right] - \sigma_3}{\sigma_1 - \sigma_3} \quad [4-7]$$

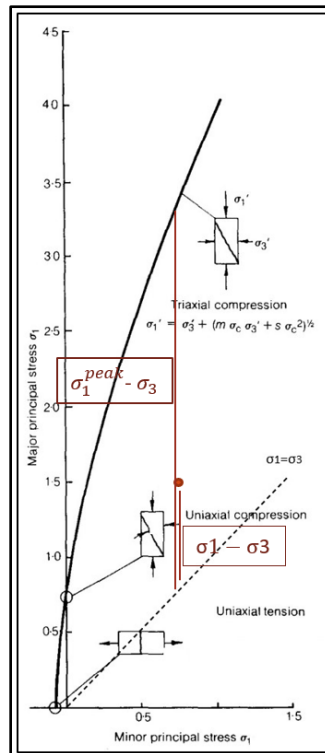


Figure 4-8. Relationship between major and minor principal stresses for Hoek-Brown. The dashed line represents $\sigma_1 = \sigma_3$ (After Hoek, 1983).

The minimum principal induced stress for each model zone is retrieved by a built-in FISH-language program (Itasca, 2013) to determine if the zone is subjected to compression or tension then calculate the safety factor (Heidarzadeh et al., 2020). Figure 4-9 reveals the safety factor values around the excavations 9, 16, 22, 33, 36, 47, 51, 60, and 73. Safety factor values less than 1 is noticed in the zones between those excavations which may draw attention to probability of compressional failure due to stress concentration increase in these zones (transverse pillars) as mining advances.

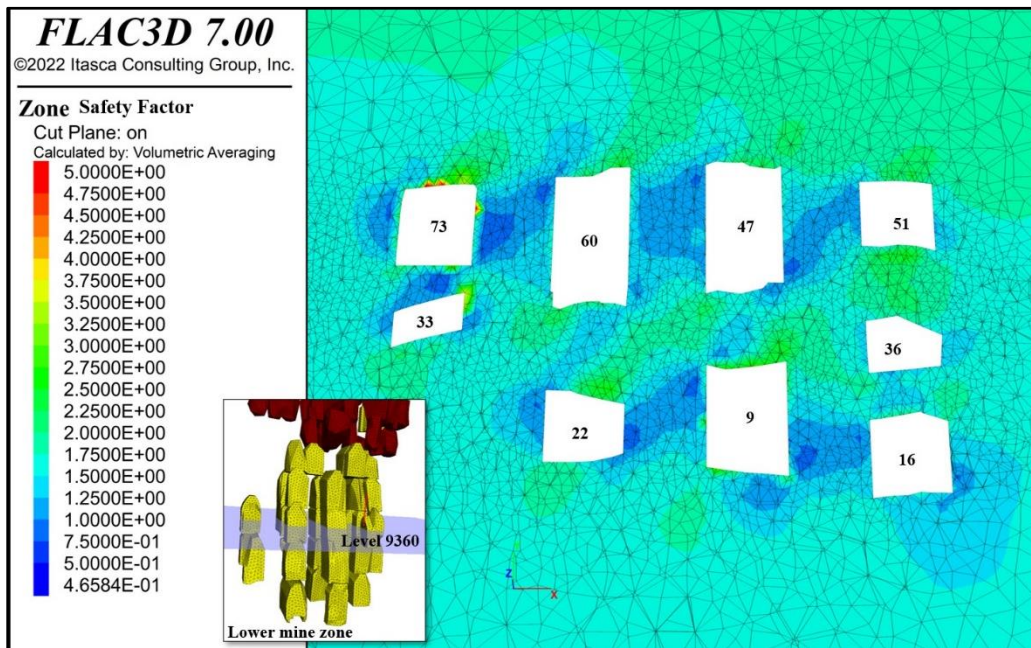


Figure 4-9. Safety factor values around the excavations 9, 16, 22, 33, 36, 47, 51, 60, and 73.

4.2.5.2 Brittle shear ratio

Castro et al. (2012) proposed the brittle shear ratio (BSR), which is used to assess the rockburst potential in underground mines (Heidarzadeh et al., 2020; Shnorhokian et al., 2015; Vennes et al., 2020; Sainoki et al., 2021). BSR is defined as the ratio of the differential stress to the uniaxial compressive strength (UCS) of rock mass.

$$BSR = \frac{\sigma_1 - \sigma_3}{UCS_{int}} \quad [4-8]$$

where σ_1 and σ_3 are the major and minor principal induced stresses. Thus, the change in BSR reveals how the differential stress of each zone varies with mining progress. The ranges of BSR

were defined along with the rockmass damage level by Castro et al. (2012) (Table 4-5). According to Castro et al. 2012, when BSR exceeds 0.7, the zone is predicted to undergo major seismic activity and is more likely to fail. Damage is initiated when BSR is between 0.3 and 0.4 in hard rock mines.

Table 4-5. Level of rockmass damage based on BSR (after Castro et al., 2012).

BSR	Rockmass Damage	Potential of strainburst
0.35	No to minor	No
0.35-0.45	Minor (e.g., surface spalling)	No
0.45-0.6	Moderate (e.g., breakout formation)	Minor
0.6-0.7	Moderate to Major	Moderate
>0.7	Major	Major

BSR is calculated for each model zone using the built-in FISH-language code (Itasca, 2013). Figure 4-10 shows BSR contours obtained from the numerical model at each mining stage through level 9360. BSR values are found to align with NE-SW direction, and the peak values are found to be at the NW and SE corners of the excavations which is consistent with the results of the maximum compressive stress. The red dot on Figure 4-10I represents point X which is selected at this level to monitor the change in BSR value with mining sequence. Figure 4-11 presents the change in BSR values at point X with mining progress between stages 9, 16, 22, 33, 36, 47, 51, 60, 73, and 76. As mining proceeds, BSR values are found to increase from around 0.29 to 0.42 which may imply a potential of damage initiation. BSR contours are also shown for each mining stage in the pillar at level 9440 (Figure 4-12). Point X is selected in the center of the pillar to examine the change in BSR value with different mining stages 14, 43, 56, and 78. BSR values are observed to increase from around 0.31 to 0.37, which may indicate a possibility of damage initiation as well (Figure 4-13). However, according to the BSR results at different stages, major rockmass damage or brittle failure would not occur under the current situation as the highest BSR does not surpass the failure limit of 0.7.

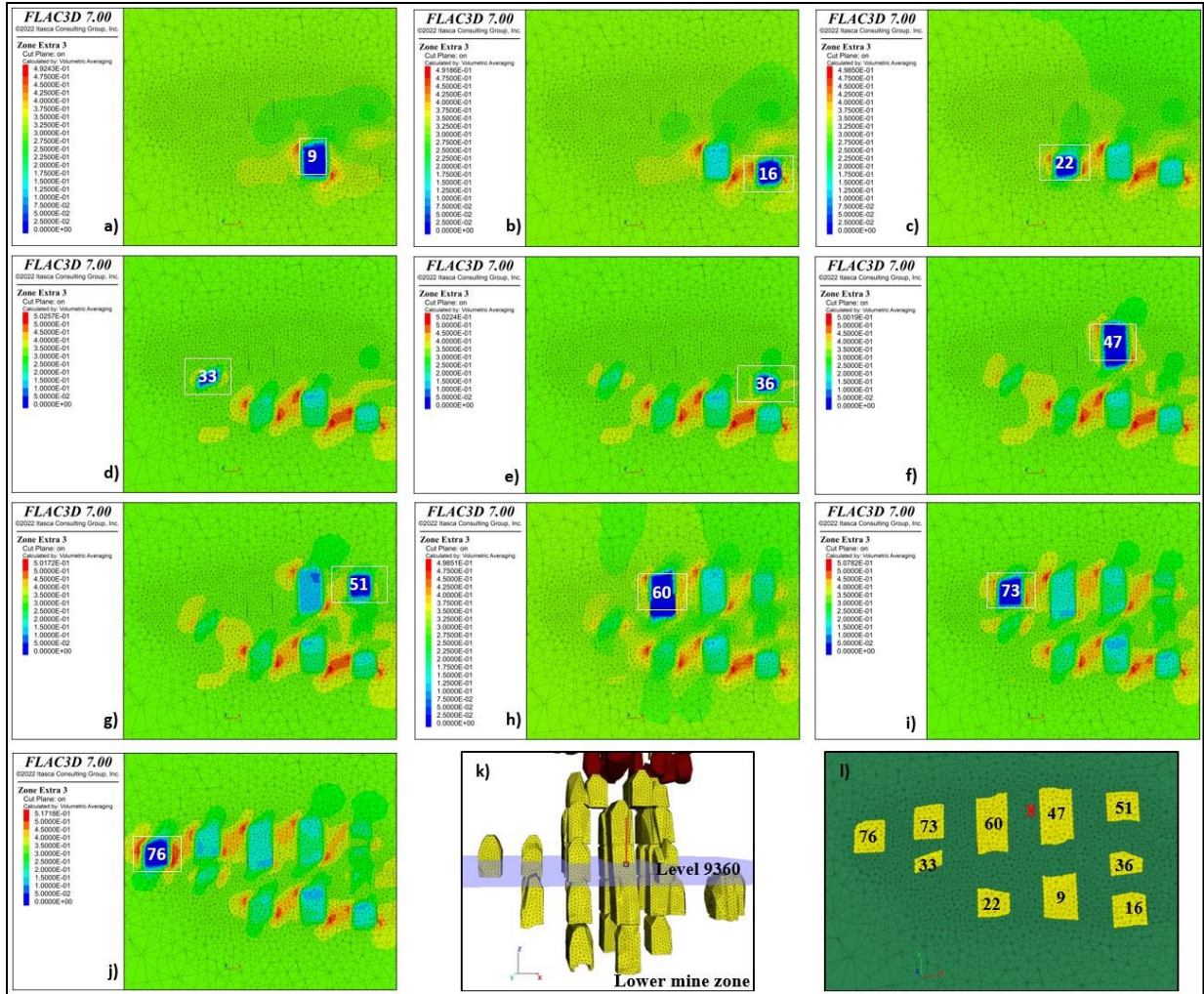


Figure 4-10. BSR contours on level 9360. a) to j) Plan views show BSR values at mining stages 9, 16, 22, 33, 36, 47, 51, 60, 73, and 76 respectively. l) The mining sequence through the level and the red point X is used to monitor the change in BSR value with mining advance.

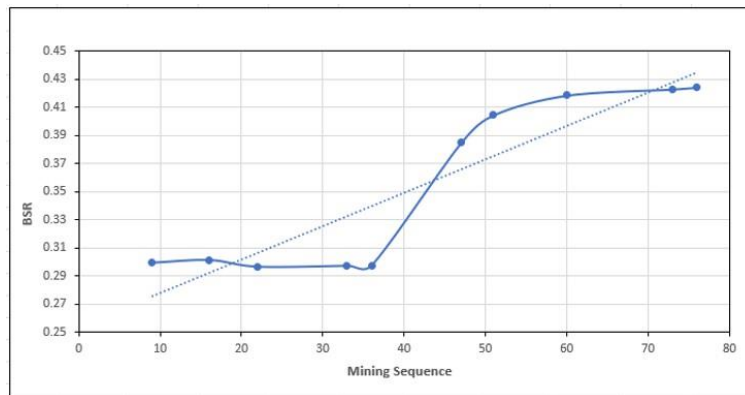


Figure 4-11. Change in BSR values at point X with mining sequence between stages 9, 16, 22, 33, 36, 47, 51, 60, 73, and 76 at level 9360.

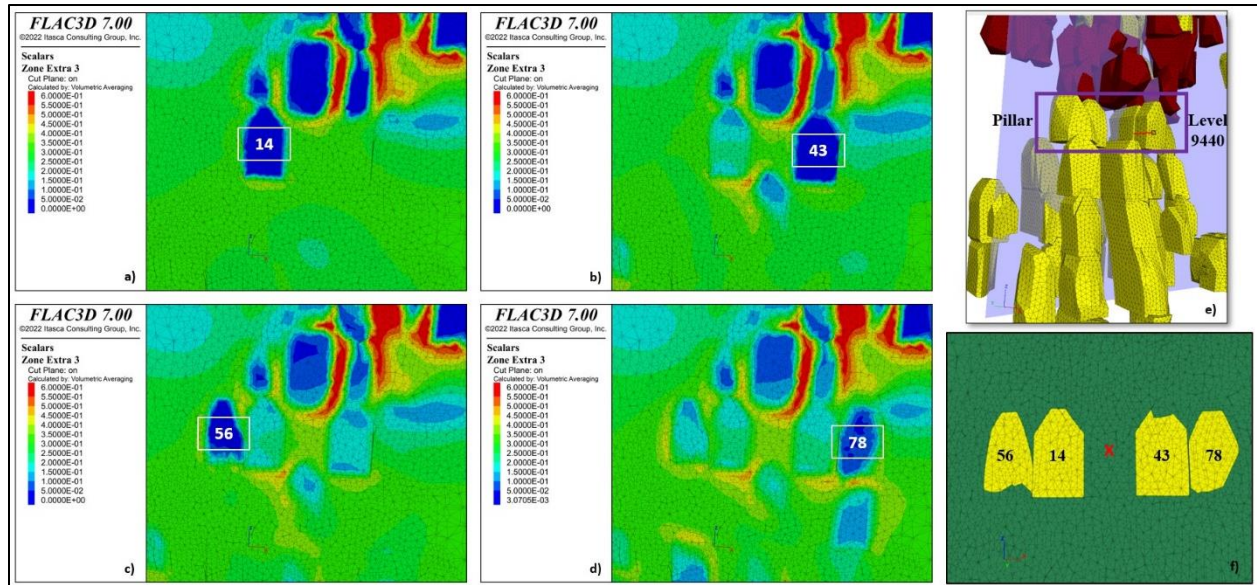


Figure 4-12. BSR contours around the pillar on level 9440. a) to d) Cross sections showing BSR values at mining stages 14, 43, 56, and 78 respectively. f) The mining sequence through the pillar and the red point X is used to monitor the change in BSR value with mining sequence.

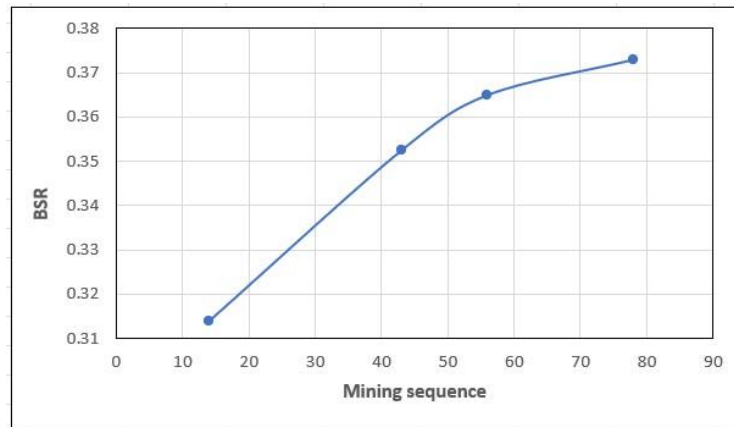


Figure 4-13. Change in BSR values at point X with mining sequence between stages 14, 43, 56, and 78 through the pillar at level 9440.

4.2.5.3 Burst Potential Index

The burst potential index (BPI) was developed to evaluate the pillar or face burst potential based on the amount of strain energy accumulated in the rock because of mining operations (Mitri et al., 1999). BPI relates the energy storage rate of the rock (ESR), the total energy stored in the rockmass due to mining, to its critical strain energy (e_c), the maximum strain energy the rockmass can withstand before failure. BPI of 100% initially denotes high risk of rockburst.

$$BPI = \frac{ESR}{e_c} \quad [4-9]$$

Since the model is loaded with stress initialization method, the ESR at each zone is calculated as follows.

$$ESR = \int \{\sigma\} d\varepsilon = \frac{1}{2} \{\varepsilon\}^T [D] \{\varepsilon\} + \{\varepsilon\}^T \{\sigma^o\} \quad [4-10]$$

Where σ and ε and are the induced stress and strain, σ^o is the in-situ stress, and [D] is the elasticity matrix. The advantage of the BPI as instability indicator is that it depends on the coupled effect of stress and stiffness or strain (Mitri, 2007).

In 2D applications, Mitri et al. (1999) proposed that e_c be evaluated from the elastic energy stored in a uniaxially loaded rock sample to the point of peak strength. For 3D applications, Vennes et al. (2020) proposed to calculate the critical strain energy using Hoek-Brown criterion. The rock strength under triaxial loading condition is estimated as the peak principal stress, σ_1^{peak} for a given σ_3 is calculated as follows:

$$\sigma_1^{peak} = \sigma_3 + \sigma_{ci} \left[m_b \frac{\sigma_3}{\sigma_{ci}} + s \right]^a \quad [4-11]$$

Where σ_{ci} is the uniaxial compressive strength of the intact rock material and m_b, s , and a are material constants. Then, Hooke's law is applied to determine the axial and radial strain at failure under triaxial loading, assuming that $\sigma_{11} = \sigma_1$, $\sigma_{12} = \sigma_{23} = \sigma_{13} = 0$, and $\sigma_{22} = \sigma_{33} = \sigma_r$. ESR of the specimen at failure can then be estimated analytically and regarded as the critical strain energy of the rock under triaxial conditions.

$$\begin{aligned} e_c &= \frac{1}{2} (\sigma_1, \sigma_3, \sigma_3)^T (\varepsilon_1, \varepsilon_3, \varepsilon_3) \\ &= \frac{1}{2E} (\sigma_1^{peak 2} + 2\sigma_3^2 - 2\nu(2\sigma_1^{peak} \sigma_3 + \sigma_3^2)) \end{aligned} \quad [4-12]$$

Equation [4-12] is used to calculate e_c and then BPI value is calculated for each zone in the model. It is set to 0 for zones in low stress regime where $\sigma_3 < 0$ since BPI is only applicable in compressive zones where brittle shear failure is expected. Figure 4-14 presents BPI contours around excavations 9, 16, 22, 33, 36, 47, 51, 60, 73, and 76 at level 9360. BPI values are found to increase with mining advance from around 65 to 100% at stages 73 and 76. High BPI at the boundaries of specific stopes

may indicate potential of local failure. BPI contours around openings 14, 43, 56, and 78 inside the pillar at level 9440 are also presented in Figure 4-15. BPI values are observed to increase around the openings from about 40% at stage 14 to 95% at stage 78. Increase in BPI values suggest increase in the energy stored in the rockmass and in turn potential burst failure.

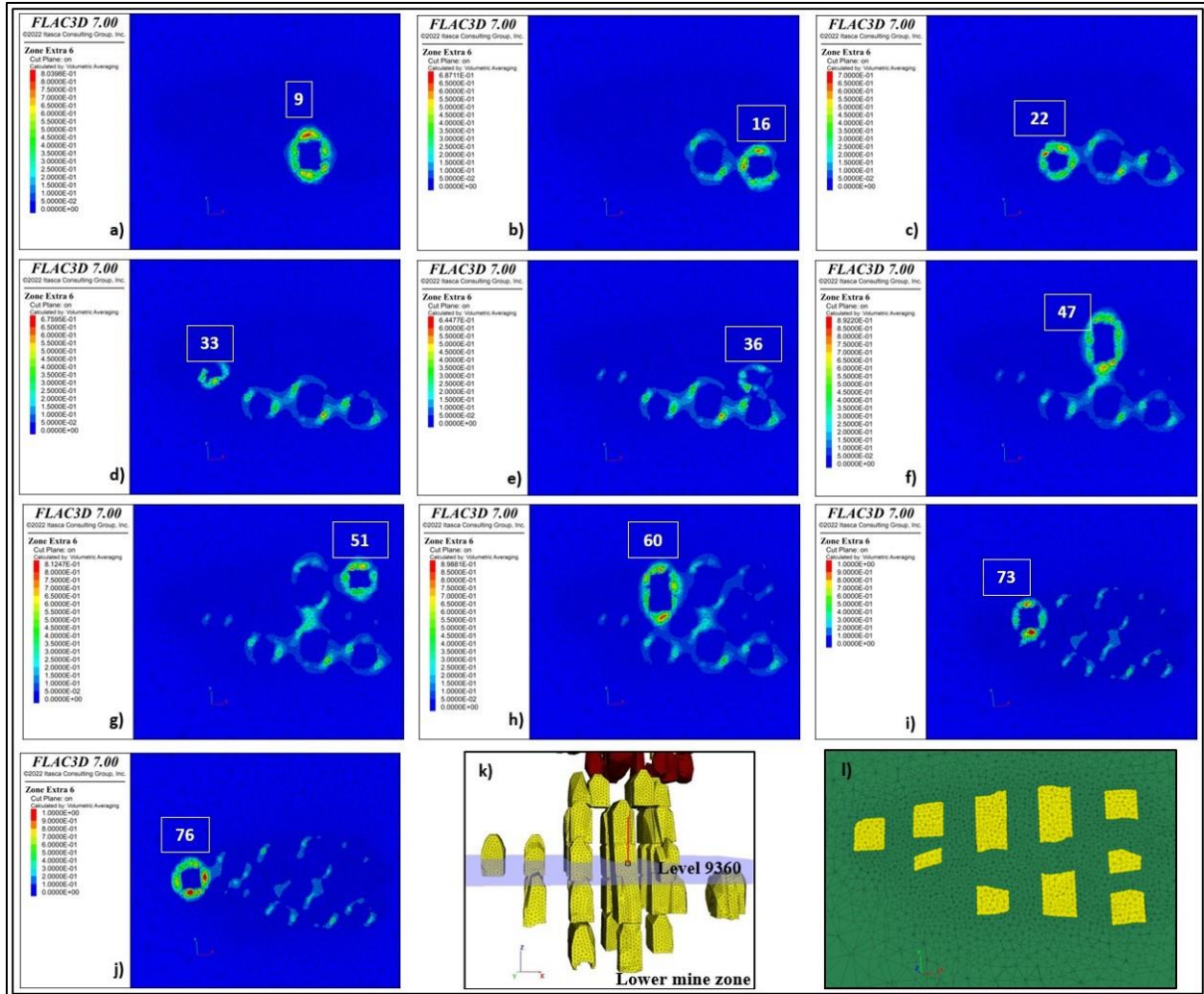


Figure 4-14. BPI contours on level 9360. a) to j) Plan views show BPI values around excavations 9, 16, 22, 33, 36, 47, 51, 60, 73, and 76 respectively. l) The mining sequence through the level.

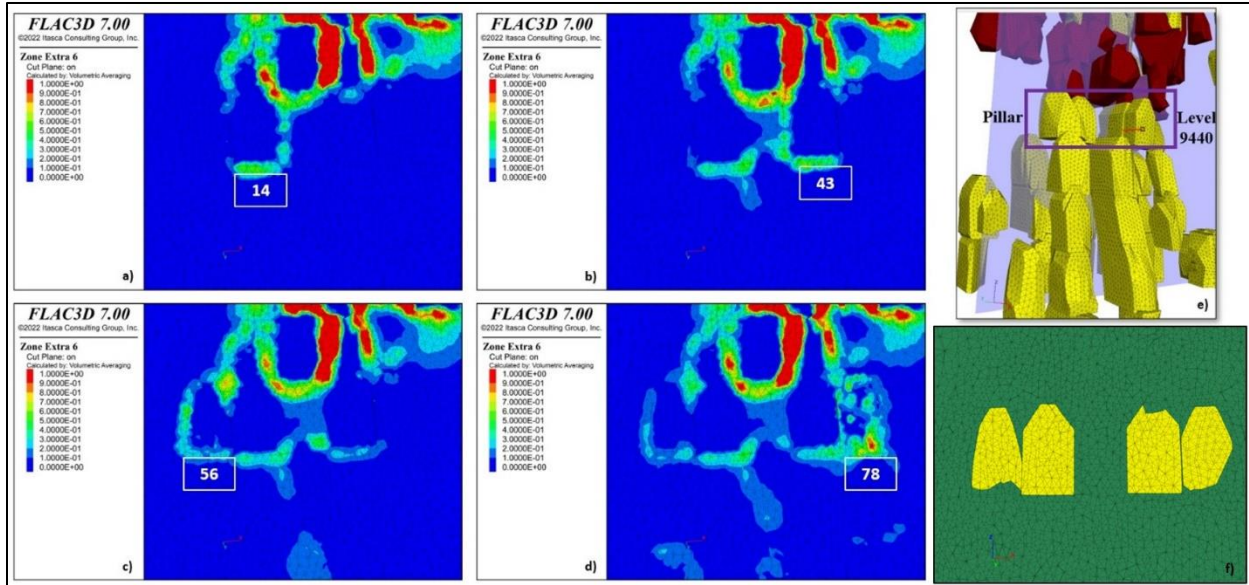


Figure 4-15. BPI contours around the pillar on level 9440. a) to d) Cross sections show BPI values around excavations 14, 43, 56, and 78 respectively. f) The mining sequence through the pillar.

4.2.5.4 Correlation between induced seismicity and instability indicators

As was previously noted, seismic events of magnitude M_w 2.0+ have been observed in the deeper mine zone (Figure 4-16). To better understand the seismic behavior at this zone, the relation between the large seismic events and the compressive safety factor (SF), brittle shear ratio (BSR), and burst potential index (BPI) has been analyzed.

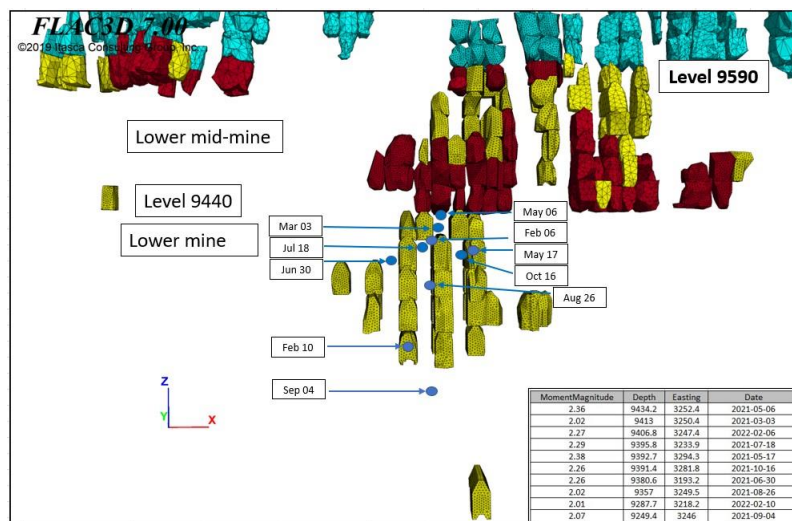


Figure 4-16. Seismic events of magnitude M_w 2.0+ in the lower-mine zone.

Examples of four of the significant events that were investigated in the lower mine zone are shown in Figure 4-17, with the corresponding SF, BSR, and BPI values. Table 4-6 provides a summary of the values for all addressed events. In accordance with the BPI, the values at the large events didn't exceed 14% which may exclude the strainburst probability of the addressed large events even for event Feb. 10, 2022, where BPI reaches 40% at stage 71. Compressive SF values didn't correlate with the large events as well since all the values are more than 1. According to BSR, the values at the large events are between 0.3 to 0.43, the damage initiation threshold. This could be used to set 0.3 as a threshold for potential microseismicity in YD mine specially in stress concentration zones. However, under the current situation there's no apparent correlation between those large events and the instability indicators which could be attributed to the continuum modelling approach adopted in the study. The model treats the rockmass as a homogenous, isotropic material. This type of modelling would suppress stress concentration that normally occurs as at the contact between rock blocks.

Table 4-6. large events in the lower mine zone with the corresponding SF, BSR, and BPI.

Event	SF	BSR	BPI	M _w	Depth-Easting
03/03/2021	2	0.25	0	2.02	9413-3250
06/05/2021	1.15	0.38	0.12	2.36	9434-3252
17/05/2021	1.68	0.30	0	2.39	9393-3294
30/06/2021	1.4	0.32	0	2.27	9381-3193
18/07/2021	1.1	0.43	0.14	2.30	9396-3234
04/09/2021	1.49	0.34	0	2.07	9249-3246
16/10/2021	1.57	0.31	0	2.27	9391-3282
10/02/2022	1.2	0.40	0.41	2.02	9288-3218

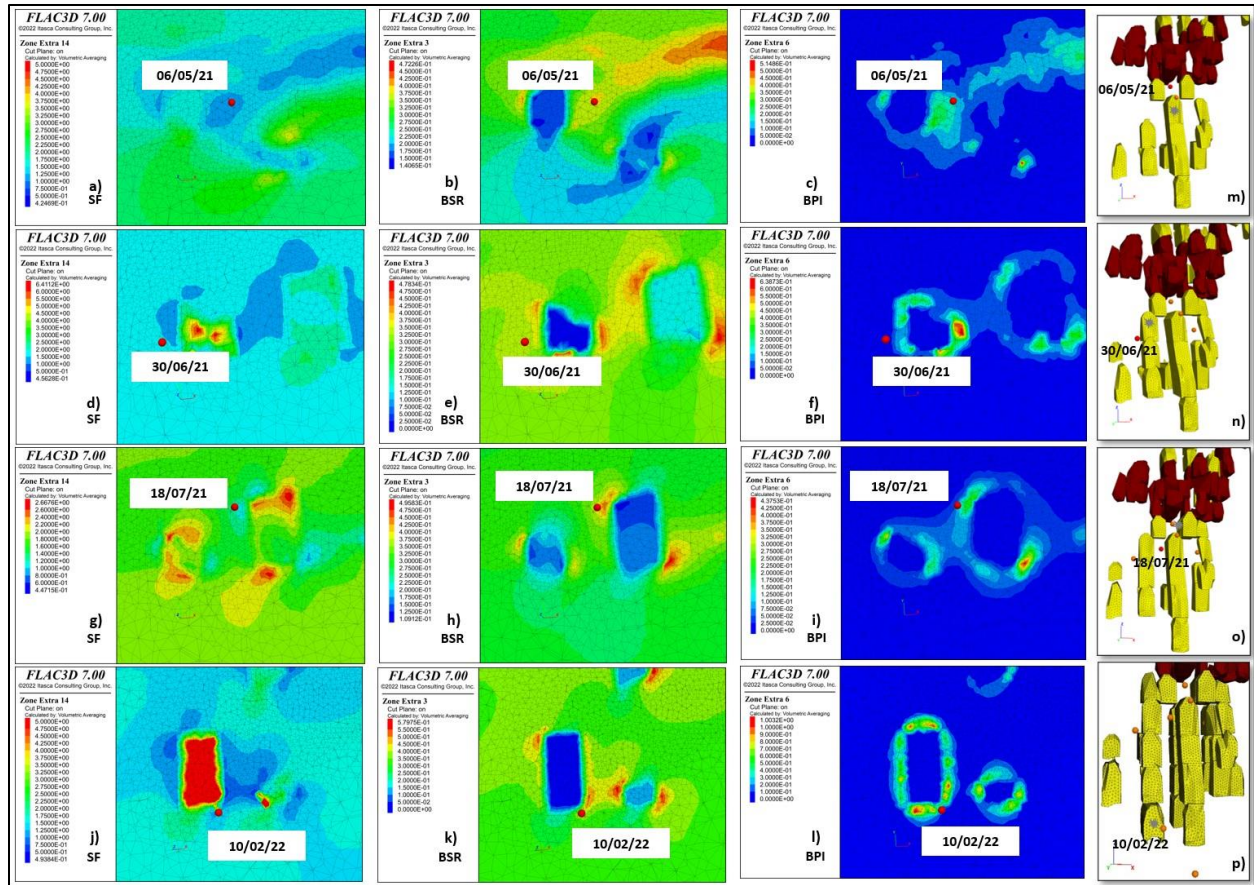


Figure 4-17. Instability indicators values at the locations of four large events. a) to l) Plan views show the SF, BSR, and BPI values at the location of the large events of May 06, 21, Jun. 30, 21, Jul. 18, 21, and Feb. 10, 22 respectively. m) to p) The large events locations with respect to the mining sequence and the grey star represents the last excavation before the triggered event.

4.3 Moment tensor inversion

To understand the root causes behind the large events, moment tensor inversion (MTI) is conducted using ESG HSS advanced software (ESG Solutions, 2020). As discussed in chapter 2, analyzing seismic wave forms, generated by the seismic events, and recorded by the monitoring system at YD mine, will help understand the rock fracturing process and the influences of mining activities or geological structures on seismic occurrence (Cronin, 2004). Focal mechanism solution (FMS) results of each event decompose the seismic MT into its isotropic (ISO), double-couple (DC), compensated linear vector dipole (CLVD) components, following the decomposition introduced by Knopoff and Randall (1970).

4.3.1 Methodology

HSS software uses the maximum likelihood approach to analyze the components of the moment tensor from low frequency plateaus of displacement amplitude spectra (Aki and Richards, 1980). It requires the sensor and event locations, amplitudes of the spectral displacement plateau, and the polarity of the first motion. The first arrival times were manually picked from the available records for each studied event. Then, all available signals are modeled separately using the displacement spectrum type. The amplitude spectrum of a selected seismic signal is fitted by Brune model (1970).

$$\Omega(f) = \frac{\Omega_0 e^{-\frac{\pi ft}{Q}}}{\left(1 + \left(\frac{f}{f_c}\right)^{\gamma n}\right)^{\frac{1}{\gamma}}} \quad [4-13]$$

Where Ω_0 is the low frequency plateau below the corner frequency f_c , f is frequency, t is travel time, n is the high frequency fall-off rate ($n = 2$), γ is the sharpness of the corner in the source spectra ($\gamma = 1$), and Q is a quality factor; it represents the seismic wave attenuation and can be determined using the spectral decay technique based on the deviation of the displacement spectrum slope from a value of -2 beyond the corner frequency. This latter slope was identified by Brune (1970) as a model of a non-attenuated displacement spectra for a shear failure. In underground mines, Q -values can range from 20 (higher attenuation and higher correction applied) to 1000. A constant Q -value is assumed for all the studied events ($Q = 100$). A homogenous velocity model is used in this software as well where $V_p = 6020$ m/s and $V_s = 3240$ m/s. Figure 4-18 shows an example of the spectral analysis graph.

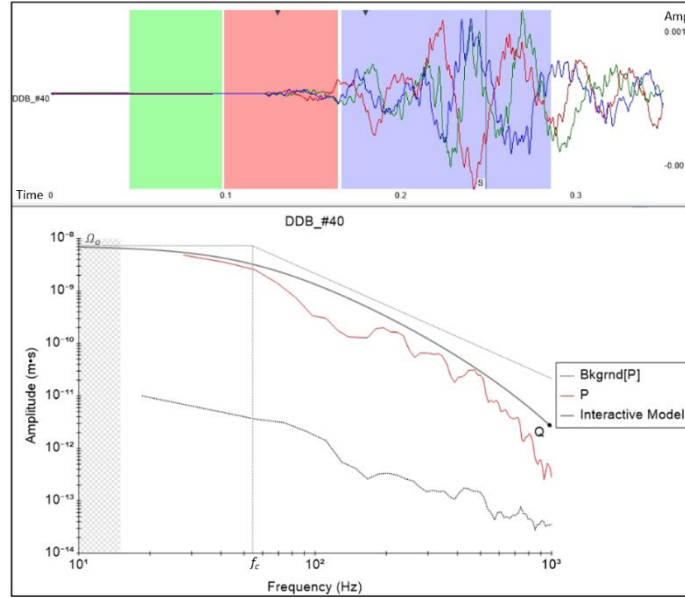


Figure 4-18. Example of the spectral analysis graph of a selected waveform at sensor 16 recording event of Mar 03, 2021. Ω_0 represents the low-frequency displacement spectrum level, f_c is the corner frequency, and Q is the attenuation factor.

4.3.2 Results and discussion

The moment tensor decompositions for five of the analyzed events of magnitude M_w 2.0+ in the lower mine zone are represented in Table 4-7 and the graphical representations of the moment tensors are shown in Figure 4-19. Moment tensor decompositions reveal that for the analyzed events, the percentage of the DC component is higher than 50%, suggesting the shear failure prevalent in those events. The negative ISO components, on the other hand, show that these sources have experienced implosive deformation, which is a core feature of compressional failure. These events are likely relevant to collapse because they also exhibit negative CLVD contributions. The source mechanisms of the five events are very close, and it is most probably shearing failure / compressional failure. According to locations and time of those events, it is worth noting that, the analyzed events happened while mining toward the pillar which would explain the results of the focal mechanism solutions.

Table 4-7. Moment tensor decompositions and source mechanisms reported for five events of magnitude M_w 2.0+ in the lower-mine zone.

Event	ISO%	DC%	CLVD%	Failure mechanism
03/03/2021	-19.2	70.4	-10.5	Shear failure / Compressional failure
06/05/2021	-20.6	61.7	-17.7	Shear failure / Compressional failure
18/07/2021	-23.5	60.7	-15.8	Shear failure / Compressional failure
16/10/2021	-15.2	67.8	-17	Shear failure / Compressional failure
06/02/2022	-11.1	73.1	-15.7	Shear failure / Compressional failure

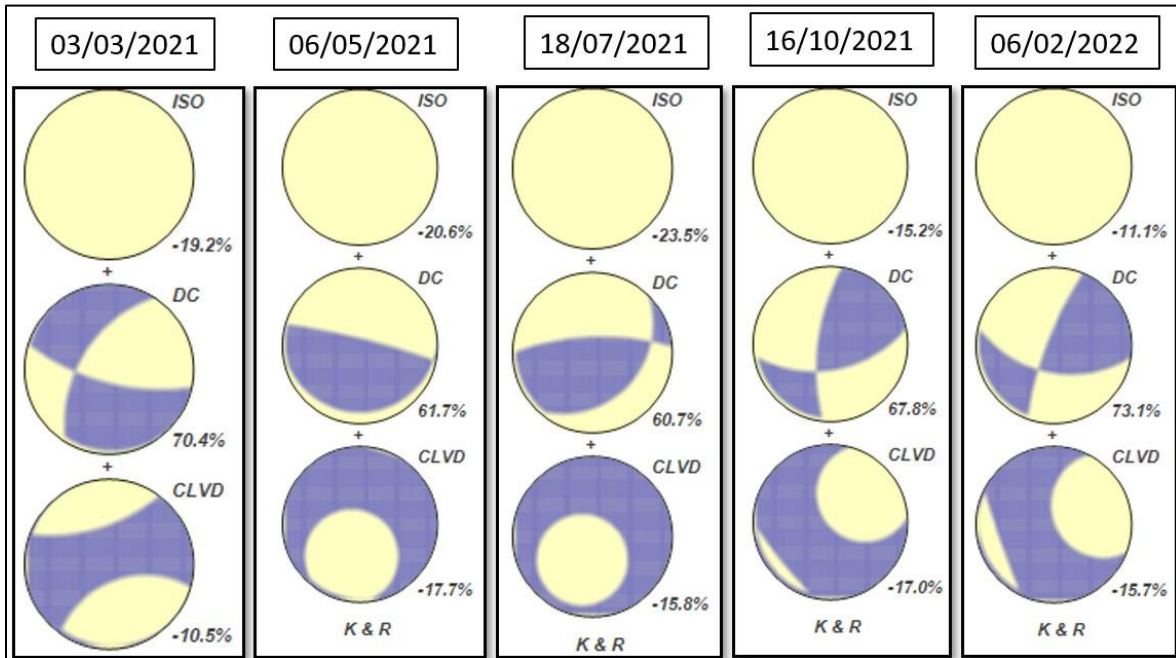


Figure 4-19. Focal mechanism solution beach balls of the analyzed events, representing the ISO, DC, and CLVD tensors respectively.

The uncertainty of the results of the five addressed events is determined using the normalized root mean square and the condition number (CN). The condition number represents the ratio between the square root of the largest eigenvalue to the smallest eigenvalue of the generalized inversion (Dahm and Krüger, 2014). It is a measure of how the solution will be sensitive to changes in the solution inputs. Table 4-8 shows RMSERROR and CN values for the five events analyzed. The results of the uncertainty measures are considered satisfactory especially for events Mar 03, 2021, and Feb 06, 2022, where both RMSERROR and CN are relatively low. However, despite the increase in the number of observations using HSS software, the increase in the condition number for the other three events indicates lower confidence in the solution which can be attributed to the limitations of the input data as discussed earlier.

Table 4-8. RMSERROR and CN values of the resultant solution for the five studied events.

Event	RMSERROR	CN
03/03/2021	0.232	33
06/05/2021	0.383	46
18/07/2021	0.222	46
16/10/2021	0.215	51
06/02/2022	0.113	18

4.4 Conclusion

A mine-wide numerical model is generated in FLAC3D considering the three mining zones: upper, middle, and lower mine zones with the diabase dykes and calibrated based on in-situ stress measurements. A qualitative investigation is conducted to assess mining seismicity in the lower-mine zone using Hoek-Brown compressive SF, BSR, and BPI. Comparison with seismic source location, magnitude, and mechanisms is presented. The study's findings are summarized as follows.

Mining activities on the same level affect the induced stresses in the mining vicinity and stress buildup zones in the mining blocks representing future secondary stopes. The maximum principal stress is observed to be aligned with NE-SW direction which concurs with the stress measurements in the YD mine. Thus, the maximum compressive stress values are found to reach 90 MPa at the NW and SE stope corners and stress concentration zones are apparent in the transverse pillars. The

observed SF values in these zones are less than 1 which may call attention to the possibility of compressional failure because of stress concentration.

The BSR values align with NE-SW direction, and the peak values are found to be at the NW and SE corners of the excavations which is congruent with the results of the maximum compressive stress. As mining proceeds, BSR values are found to increase to 0.42 at the same level which may imply a potential of damage initiation. However, brittle failure would not occur in the current circumstance, as the highest BSR value never exceeds the failure limit of 0.7. BPI values are found to increase with mining advance from around 65 to 100% at the latest addressed stages. Increase in BPI values indicates an increase in the energy stored in the rockmass and in turn potential of local failure with future mining activity.

In terms of the correlation between the large seismic events in lower-mine zone and the studied instability indicators, BPI values are below 14% for all the analyzed events and reaches 40% for only event of Feb. 10, 2022, at stage 71, which could rule out the possibility of strainburst as a cause for those large events. The compressive SF values do not correspond with the major events since all the values are more than 1. BSR values at the large events are between 0.3 to 0.43, the damage initiation threshold, which could be utilized to designate 0.3 as a threshold for potential microseismicity in YD mine specially in stress concentration zones. However, under the current situation there's no apparent correlation between those large events and the instability indicators which might be attributed to the continuum modelling approach adopted in the study.

FLAC3D is a continuum model that does not explicitly model discontinuities. The model treats the rockmass as a homogenous, isotropic material. This type of modelling would suppress stress concentration that normally occurs as at the contact between rock blocks. Thus, one of the recommendations for future work is to consider modeling the main discontinuities in the mine domain. Mine wide modeling combined with discontinuum modelling can give more accurate representations to the studied indicators. It is also worth noting that BSR and BPI results are dependent on the strength of the rockmass. A slight decrease in the strength parameters (UCS, m , s) would result in higher BSR and BPI.

Moment tensor decompositions reveal higher than 50% of DC component, negative ISO components, and negative CLVD components. The generated solution suggests that the shear failure is dominant in these sources with implosive deformation, and they are likely relevant to collapse. The source mechanisms of the analyzed events are most properly shearing failure / compressional failure. It is important to consider that the analyzed events occurred while mining towards the pillar which is comparable with their FMS results and their locations and times.

Chapter 5 – Conclusion

5.1 Summary of conclusions

Underground mining activities affect the field stresses in the vicinity and could create stress concentration zones in the ore blocks representing future stopes. Mining induced seismicity occurs frequently due to stress redistribution in the mining area. Strong seismic events could cause damage to drifts and stopes resulting in production delays and increase of the risk of accidents in mining operations. Thus, it is crucial to analyze the root causes of induced seismicity to help find mitigation measures and provide a safer work environment. This could also be useful for mine planning.

This thesis reports the analysis results of a case study of Young-Davidson (YD) mine in northern Ontario, a gold mining operation using sublevel stoping method with delayed backfill. The research aims to conduct a comprehensive study of the microseismic database to understand the causes of large micro-seismic events. Although strong seismic activities are normally expected to be associated with deep excavations, seismic events of magnitude $M_n 2.0+$ have been observed at mining depths of only 600 m to 800 m below surface in 2020. Large seismic events were also observed in the lower-mine zone in 2021 and 2022 with mining advance.

The occurrence of large events at shallow depth is the focus of the first part of this study. The impact of blasting volume on accumulated seismic moment and energy was first investigated. In addition, the stress regime of mining zones that intersected with regional dykes is studied by the b-value analysis through this mining level. Moment tensor inversion for three large seismic events is carried out using HybridMT MATLAB code to determine the failure mechanisms and understand the influence of mining activities and geological structures on seismicity. The effect of mining sequence on the seismic response is also investigated.

The findings are summarized as follows.

1. There is no apparent correlation between blasting volume and accumulated seismic moment or energy in the studied area.
2. The analysis of b-values differentiates the stressed from non-stressed zones. Low b-value

towards the east reflects highly stressed zone and explains the occurrence of two large events. High b -values close to the main intersecting dyke indicate that the dyke is not the primary cause of the near major events.

3. Focal mechanism solutions of the analyzed events show almost the same failure mechanism, which is compressional failure. The percentage of DC components indicate that shear failure is not prevalent, whereas the negative ISO and CLVD components indicate that the sources experienced implosive deformation, which is a characteristic feature of compressional failure.
4. Despite the uncertainty in the resultant solutions due to the lack of sensor coverage in the studied zone, the possible mechanisms can be confirmed based on mining sequences since these events occurred while mining towards the sill pillar, which demonstrates the consistency in their focal mechanism solutions.

In the second part of the study, analysis of seismic events of magnitude M_w 2.0+, that were observed in the lower-mine, is conducted. A mine-wide numerical model is constructed in finite difference software FLAC3D. The model considers the three mining zones in YD mine: upper, middle, and lower with the intersecting northeast-trending diabase dykes to simulate mining-induced stress distribution per the YD mine plan of primary and secondary stope extraction. To build a calibrated model, a series of numerical simulations was performed based on previous in-situ stress measurements in the mine and estimation of in-situ stress magnitude and orientation that was done by McGill Mine Design Lab using diametrical core deformation technique. Rockmass characterization systems GSI and Q are used to estimate rockmass properties for numerical modelling using RSDData software. A qualitative analysis is conducted to assess mining seismicity in the lower-mine zone using Hoek-Brown compressive SF, BSR, and BPI, as well as comparison with seismic source location, magnitude, and mechanism are discussed. Moment tensor inversion of five large events is carried out to identify the rock failure mechanisms using ESG HSS-Advanced seismic analysis software.

The findings are summarized as follows.

1. The maximum principal stress orientation (NE-SW) agrees with the stress measurements in the YD mine and the maximum values are found to reach 90 MPa at the NW and SE corners of the mined stopes.

2. Stress concentration zones are apparent in the transverse pillars and the compressional SF values in these zones are less than 1 which may call attention to the possibility of compressional failure with mining advance.
3. The peak BSR values are congruent with the maximum compressive stress results. As mining proceeds, BSR values are found to reach the damage initiation threshold. However, brittle failure would not occur in the current situation as the highest BSR value does not exceed the failure limit.
4. BPI values are found to reach 100% with mining advance. Increased BPI values signify more energy being stored in the rock which increases the risk of local failure with future mining operations.
5. Regarding the relationship between the significant seismic occurrences in the lower-mine zone and the examined instability indicators, the conclusions are as follows.
 - Low BPI values for all the analyzed events could exclude the strainburst probability as a cause for those events.
 - Compressive SF values larger than 1 do not correspond with the major events.
 - BSR values at the large events could be used to set 0.3 as a threshold for potential microseismicity in YD mine specially in stress concentration zones.
 - Due to the continuum modelling approach used in the study, there does not appear to be a correlation between those significant occurrences and the instability indicators.
6. The generated focal mechanism solution suggests that shear failure is dominant in these sources, unlike the events in the above zone, with implosive deformation. The source mechanisms of the analyzed events are most likely shearing failure / compressional failure.
7. It is important to consider that the analyzed events occurred while mining towards the pillar which is comparable to their FMS results and their locations and times. The is the same as the events analyzed in the zone above.
8. Thus, sill pillar recovery at different levels in YD mine might be the main contributor to increased mining-induced seismicity under the current circumstances leading to high mining-induced stress.

Although the results of this study are specific to YD Mine, they may be applicable to other mines with similar conditions.

5.2 Suggestions for future research

The slip plane can be further examined by looking at the FMS for further occurrences in the future. This may also assist predict the trend of seismic hazards, which will be very helpful for mine planning and safety consideration in the future.

As a continuum model, FLAC3D treats the rockmass as a homogeneous, isotropic material and does not explicitly model discontinuities. The stress concentration that typically develops at the contact surface between rock blocks would not be detected by this form of modelling. Thus, considering modelling the fracture network that consists of the main discontinuity sets in the seismic event locations could yield more accurate representations to the studied indicators. Such hybrid approach would still require FLAC3D model to obtain the field stress in the area to be further discretized with discrete element modelling software like 3DEC of Itasca Ltd.

References

Abzalov, M. (2016). Applied mining geology (Vol. 12). Switzerland: Springer International Publishing.

Aki, K. (1965). Maximum likelihood estimate of b in the formula $\log N = a - bM$ and its confidence limits. Bull. Earthquake Res. Inst., Tokyo Univ., 43, 237-239.

Aki, K. and P. G. Richards (1980). Quantitative seismology, W.H. Freeman & Co.

Alamos Gold Inc. (2015). Mines and Projects: <http://www.alamosgold.com/mines-and-projects/producing-mine/Young-Davidson/>.

Alamos Gold Inc. (2020). Ground Control Management Plan.

Alamos Gold Inc. (2021). Seismic Risk Management Plan.

Amitrano, D. (2003). Brittle-ductile transition and associated seismicity: Experimental and numerical studies and relationship with the b value. Journal of Geophysical Research: Solid Earth, 108(B1).

Andrews, D. J. (1986). Objective determination of source parameters and similarity of earthquakes of different size. Earthquake source mechanics, 37, 259-267.

Barton, N., Lien, R., & Lunde, J. J. R. M. (1974). Engineering classification of rock masses for the design of tunnel support. Rock mechanics, 6, 189-236.

Bieniawski, Z. T. (1973). Engineering classification of jointed rock masses. Civil Engineering=Siviele Ingenieurswese, 1973(12), 335-343.

Bieniawski, Z. T. (1976). Rapid site appraisal for dam foundations by the geomechanics classification. Commission internationale des grands barrages.

Blake, W., & Hedley, D. G. (2003). Rockbursts: case studies from North American hard-rock mines. SME.

Boettcher, M. S., McGarr, A., & Johnston, M. (2009). Extension of Gutenberg-Richter distribution to $M_w - 1.3$, no lower limit in sight. *Geophysical Research Letters*, 36(10).

Brown, E. T. (1980). *Underground excavations in rock*. CRC Press.

Brown, L. G. (2018). Quantification of seismic responses to mining using novel seismic response parameters (Doctoral dissertation, Laurentian University of Sudbury).

Brown, L. G., & Hudyma, M. R. (2018, June). Mining induced seismicity in Canada: a 2017 update. In 52nd US Rock Mechanics/Geomechanics Symposium. OnePetro.

Brown, L., & Hudyma, M. (2017). Identification of stress change within a rock mass through apparent stress of local seismic events. *Rock Mechanics and Rock Engineering*, 50(1), 81-88.

Brune, J. (1971). Correction [to “Tectonic stress and the spectra, of seismic shear waves from earthquakes”]. *Journal of Geophysical Research*, 76(20), 5002-5002.

Brune, J. N. (1970). Tectonic stress and the spectra of seismic shear waves from earthquakes. *Journal of geophysical research*, 75(26), 4997-5009.

Caputa, A., Rudziński, Ł., & Cesca, S. (2021). How to Assess the Moment Tensor Inversion Resolution for Mining Induced Seismicity: A Case Study for the Rudna Mine, Poland. *Frontiers in Earth Science*, 9, 671207.

Caputa, A., Talaga, A., & Rudziński, Ł. (2015). Analysis of post-blasting source mechanisms of mining-induced seismic events in Rudna copper mine, Poland. *Contemporary Trends in Geoscience*, 4.

Castro, L. A. M., Bewick, R. P., & Carter, T. G. (2012). An overview of numerical modelling applied to deep mining. *Innovative numerical modelling in geomechanics*, 393-414.

Chen, J., Liu, X., & Xu, Q. (2017). Numerical simulation analysis of damage mode of concrete gravity dam under close-in explosion. *KSCE Journal of Civil Engineering*, 21, 397-407.

Collins, D. & Hosseini, Z. (2013). Harnessing microseismic monitoring. https://www.esgsolutions.com/sites/esgsolutions.com/files/resource/2013_march_mining_magazine_-_microseismic_monitoring_for_caving_operations.pdf.

Cronin, V. (2004). A draft primer on focal mechanism solutions for geologists. Texas. Baylor University, 14.

Dahlen, F. A. (1977). The balance of energy in earthquake faulting. *Geophysical Journal International*, 48(2), 239-261.

Dahm, T., & Krüger, F. (2014). Moment tensor inversion and moment tensor interpretation. In *New Manual of Seismological Observatory Practice 2 (NMSOP-2)* (pp. 1-37). Deutsches GeoForschungsZentrum GFZ.

Deere, D. U. (1964). Technical description of rock cores for engineering purpose. *Rock Mechanics and Engineering Geology*, 1(1), 17-22.

Dreger, D. S., Ford, S. R., & Walter, W. R. (2008). Source analysis of the Crandall Canyon, Utah, mine collapse. *Science*, 321(5886), 217-217.

Eaton, D. W. (2008). Microseismic focal mechanisms: A tutorial. Calgary, Alberta: CREWES Research Report, 20, 1-11.

Eaton, D. W., & Forouhideh, F. (2010). Microseismic moment tensors: The good, the bad and the ugly. CSEG Recorder, 35(9), 45-49.

ESG Hyperion Software Suite Version 16.0 User's Guide, Volume 1. ESG Solutions, Kingston, Ontario.

ESG Hyperion Software Suite Version 16.0 User's Guide, Volume 2. ESG Solutions, Kingston, Ontario.

ESG SOLUTIONS (2020) Seismic Software Suite (HSS). <https://www.environmental-expert.com/software/esg-windows-based-hyperion-seismic-software-suite-hss-605490>.

Eyre, T. S., & van der Baan, M. (2015). Overview of moment-tensor inversion of microseismic events. The Leading Edge, 34(8), 882-888.

Ge, M. (2005). Efficient mine microseismic monitoring. International Journal of Coal Geology, 64(1-2), 44-56.

Geiger, L. (1912). Probability method for the determination of earthquake epicentres from the arrival time only. Bull. St. Louis Univ., 8, 60.

Gibowicz, S. (1990). The mechanism of seismic events induced by mining.

Gibowicz, S.J., and A. Kijko (1994) An introduction to mining seismology. 1st ed. San Diego: Academic Press.

Giles D. (2013) Magnitude Measures. In: Bobrowsky P.T. (eds) Encyclopedia of Natural Hazards. Encyclopedia of Earth Sciences Series. Springer, Dordrecht. https://doi.org/10.1007/978-1-4020-4399-4_225.

Gnyp, A., & Malytskyy, D. (2021). Differential and source terms locations of the 2015 Teresva (East Carpathians) series and their tectonic implications. *Acta Geophysica*, 69(6), 2099-2112.

Godano, C., Lippiello, E., & De Arcangelis, L. (2014). Variability of the b value in the Gutenberg–Richter distribution. *Geophysical Journal International*, 199(3), 1765-1771.

Guha S.K. (2000) Mining Induced Seismicity. In: Induced Earthquakes. Springer, Dordrecht. https://doi.org/10.1007/978-94-015-9452-3_5.

Gulia, L., & Wiemer, S. (2010). The influence of tectonic regimes on the earthquake size distribution: A case study for Italy. *Geophysical Research Letters*, 37(10).

Gutenberg, B. (1945). Amplitudes of surface waves and magnitudes of shallow earthquakes. *Bulletin of the Seismological Society of America*, 35(1), 3-12.

Gutenberg, B., & Richter, C. F. (1944). Frequency of earthquakes in California. *Bulletin of the Seismological society of America*, 34(4), 185-188.

Hanks, T. C., & Kanamori, H. (1979). A moment magnitude scale. *Journal of Geophysical Research: Solid Earth*, 84(B5), 2348-2350.

Hasegawa, H. S., Wetmiller, R. J., & Gendzwill, D. J. (1989). Induced seismicity in mines in Canada—an overview. *Pure and Applied Geophysics*, 129(3), 423-453.

Heal, D., Hudyma, M., & Potvin, Y. (2006, June). Evaluating rockburst damage potential in underground mining. In *Golden Rocks 2006, The 41st US Symposium on Rock Mechanics (USRMS)*. OnePetro.

Hedley, D. G. (1992). Rockburst handbook for Ontario hardrock mines (Vol. 92, No. 1). Canmet.

Heidarzadeh, S., Saeidi, A., & Rouleau, A. (2020). Use of probabilistic numerical modeling to evaluate the effect of geomechanical parameter variability on the probability of open-stope failure: a case Study of the Niobec Mine, Quebec (Canada). *Rock Mechanics and Rock Engineering*, 53, 1411-1431.

Hoek, E. (1983). Strength of jointed rock masses. *Geotechnique*, 33(3), 187-223.

Hoek, E., Carranza-Torres, C., & Corkum, B. (2002). Hoek-Brown failure criterion-2002 edition. *Proceedings of NARMS-Tac*, 1(1), 267-273.

Hoek, E., Kaiser, P. K., & Bawden, W. F. (2000). *Support of Underground Excavations in Hard Rock*. CRC Press.

Holub, K. (1997). Predisposition to induced seismicity in some Czech coal mines. In *Seismicity Associated with Mines, Reservoirs and Fluid Injections* (pp. 435-450). Birkhäuser, Basel.

Horner, RB, & Hasegawa, HS (1978). The seismotectonics of southern Saskatchewan. *Canadian Journal of Earth Sciences*, 15 (8), 1341-1355.

Hudson, J. A., Pearce, R. G., & Rogers, R. M. (1989). Source type plot for inversion of the moment tensor. *Journal of Geophysical Research: Solid Earth*, 94(B1), 765-774.

Hudyma, M. R. (1995). Seismicity at Brunswick mining. In *Proceedings Quebec Mining Association Ground Control Colloque*. Val D'Or, Quebec.

Hudyma, M. R. (2008). *Analysis and interpretation of clusters of seismic events in mines*. University of Western Australia.

Hudyma, M. R., Frenette, P., & Leslie, I. (2010). Monitoring open stope caving at Goldex Mine. *Mining Technology*, 119(3), 142-150.

Hudyma, M., & Potvin, Y. H. (2010). An engineering approach to seismic risk management in hardrock mines. *Rock mechanics and rock engineering*, 43, 891-906.

Ilieva, M., Rudziński, Ł., Pawłuszek-Filipiak, K., Lizurek, G., Kudłacik, I., Tondaś, D., & Olszewska, D. (2020). Combined Study of a Significant Mine Collapse Based on Seismological and Geodetic Data—29 January 2019, Rudna Mine, Poland. *Remote Sensing*, 12(10), 1570.

Itasca, F. (2009). *Fast Lagrangian analysis of continua in 3 dimensions, Version 4.0*. Minneapolis, Minnesota, Itasca Consulting Group, 438.

Itasca, F. (2013). *Fast lagrangian analysis of continua in 3 dimensions. Online Manual*, 175-180.

Jost, M. U., & Herrmann, R. B. (1989). A student's guide to and review of moment tensors. *Seismological Research Letters*, 60(2), 37-57.

Julian, B. R., Miller, A. D., & Foulger, G. R. (1998). Non-double-couple earthquakes 1. Theory. *Reviews of Geophysics*, 36(4), 525-549.

Kaiser, P. (2009). Failure mechanisms and rock Support aspects. *Int. Consultation Report for the Key Technology of Safe and Rapid Construction for Jinping II Hydropower Station High Overburden and Long Tunnels, Jinping II*, 62-71.

Kaiser, P. K. (1993). Support of tunnels in burstprone ground--Toward a rational design methodology. 3rd Int. In *Symposium on Rockburst and Seismicity in Mines*, Kingston, 15p.

Kaiser, P. K., McCreath, D. R., & Tannant, D. D. (1996). *Canadian rockburst support handbook*. Geomechanics Research Center.

Kanamori, H. (1981). The nature of seismicity patterns before large earthquakes. *Earthquake prediction: An international review*, 4, 1-19.

Knopoff, L., & Randall, M. J. (1970). The compensated linear-vector dipole: A possible mechanism for deep earthquakes. *Journal of Geophysical Research*, 75(26), 4957-4963.

Krieger, L., & Heimann, S. (2012). MoPaD—Moment tensor plotting and decomposition: A tool for graphical and numerical analysis of seismic moment tensors. *Seismological Research Letters*, 83(3), 589-595.

Kwiatek, G., Martínez-Garzón, P., & Bohnhoff, M. (2016). HybridMT: A MATLAB/shell environment package for seismic moment tensor inversion and refinement. *Seismological Research Letters*, 87(4), 964-976.

Lay, T., & Wallace, T. C. (1995). *Modern global seismology*. Elsevier.

Leake, M. R., Conrad, W. J., Westman, E. C., Afrouz, S. G., & Molka, R. J. (2017). Microseismic monitoring and analysis of induced seismicity source mechanisms in a retreating room and pillar coal mine in the Eastern United States. *Underground Space*, 2(2), 115-124.

Legge, N. B., & Spottiswoode, S. M. (1987, August). Fracturing and microseismicity ahead of a deep gold mine stope in the pre-remnant and remnant stages of mining. In 6th ISRM Congress. OnePetro.

Li, T., Cai, M. F., & Cai, M. (2007). A review of mining-induced seismicity in China. *International Journal of Rock Mechanics and Mining Sciences*, 44(8), 1149-1171.

Li, Y. (2021). *Determination of Mining-Induced Stresses Using Diametrical Rock Core Deformation Measurement and Finite Element Modelling*. McGill University (Canada).

Li, Y. (2024). Determination of mining-induced stresses using diametrical rock core deformation. McGill University (Canada). In Progress.

Li, Y., & Mitri, H. S. (2022). Determination of mining-induced stresses using diametral rock core deformations. *International Journal of Coal Science & Technology*, 9(1), 80.

Lizurek, G., & Wiejacz, P. (2011). Moment tensor solution and physical parameters of selected recent seismic events at Rudna Copper Mine. *Geophysics in mining and environmental protection*, 11-19.

Ma, J., Dong, L., Zhao, G., & Li, X. (2019). Focal mechanism of mining-induced seismicity in fault zones: a case study of yongshaba mine in China. *Rock Mechanics and Rock Engineering*, 52(9), 3341-3352.

Ma, T., Lin, D., Tang, C. A., Yadav, K. P., Feng, Z., & Ma, K. (2020). Microseismic monitoring, positioning principle, and sensor layout strategy of rock mass engineering. *Geofluids*, 2020.

Ma, X., Westman, E., Slaker, B., Thibodeau, D., & Counter, D. (2018). The b-value evolution of mining-induced seismicity and mainshock occurrences at hard-rock mines. *International Journal of Rock Mechanics and Mining Sciences*, 104, 64-70.

Malovichko, D., van Aswegen, G., & Clark, R. (2012). Mechanisms of large seismic events in platinum mines of the Bushveld Complex (South Africa). *Journal of the Southern African Institute of Mining and Metallurgy*, 112(6), 419-429.

McGarr, A. (1971). Violent deformation of rock near deep-level, tabular excavations—seismic events. *Bulletin of the seismological society of America*, 61(5), 1453-1466.

McGarr, A. (1971). Violent deformation of rock near deep-level, tabular excavations—seismic events. *Bulletin of the Seismological Society of America*, 61(5), 1453-1466.

McGarr, A. (1992). Moment tensors of ten Witwatersrand mine tremors. *pure and applied geophysics*, 139, 781-800.

McKinnon, S. D., & Labrie, D. (2006, June). Interpretation of Stresses adjacent to the Cadillac Fault assuming marginal large-scale rock mass stability. In *Proceedings of the International Symposium on In-situ Rock Stresses*, Taylor & Francis, Balkema (pp. 409-417).

MDEng. (2017). Geomechanical Review of Young-Davidson Life of Mine Extraction Plan. Mine Design Engineering Report #1015-R1606-01.

Mendecki, A. J., Van Aswegen, G., & Mountfort, P. (1999). A guide to routine seismic monitoring in mines. *A handbook on rock engineering practice for tabular hard rock mines*, 35.

Mignan, A., & Woessner, J. (2012). Estimating the magnitude of completeness for earthquake catalogs. *Community Online Resource for Statistical Seismicity Analysis*, 1-45.

Mine Design Engineering. (2015). Assessment of Stope Performance at the Young-Davidson Mine, Matachewan, Ontario, Canada.

Mirarco Mining Innovation 2012. In Situ Stress Determination. File name: YPrint@alamosgold.com_20160601_135335.

Mitri, H. S. (2007). Assessment of horizontal pillar burst in deep hard rock mines. *International Journal of Risk Assessment and Management*, 7(5), 695-707.

Mitri, H., Tang, B., Vicenzi, I. (2000) Modeling of tunnel face stresses in bedded rock. The 53rd Canadian Geotechnical Conference, Montreal.

Mitri, HS*, Tang, B.* & Simon, R. (1999). FE modelling of mining-induced energy release and storage rates. *Journal of the Southern African Institute of Mining and Metallurgy*, 99(2), 103-110.

Mosher, S. G., & Audet, P. (2020). Automatic detection and location of seismic events from time-delay projection mapping and neural network classification. *Journal of Geophysical Research: Solid Earth*, 125(10), e2020JB019426.

Moss, A., & Kaiser, P. K. (2021). An operational approach to ground control in deep mines. *Journal of Rock Mechanics and Geotechnical Engineering*.

Nelder, J. A., & Mead, R. (1965). A simplex method for function minimization. *The computer journal*, 7(4), 308-313.

Ortlepp, W. D. (1992). The design of support for the containment of rockburst damage in tunnels: an engineering approach. In *International symposium on rock support* (pp. 593-609).

Owen, M., Hudyma, M., & Potvin, Y. (2002). Risk analysis for mining induced seismicity. In *5th North American Rock Mechanics Symposium and the 17th Tunnelling Association of Canada Conference: NARMS-TAC* (pp. 1079-1086).

Rafferty, J. P. (2020). Richter scale. *Encyclopedia Britannica*.
<https://www.britannica.com/science/Richter-scale>.

Ren, Y., Vavryčuk, V., Wu, S., & Gao, Y. (2021). Accurate moment tensor inversion of acoustic emissions and its application to Brazilian splitting test. *International Journal of Rock Mechanics and Mining Sciences*, 141, 104707.

Richter, C. F. (1935). An instrumental earthquake magnitude scale. *Bulletin of the seismological society of America*, 25(1), 1-32.

Sainoki, A., Mitri, H. S., Yao, M., & Chinnasane, D. (2016). Discontinuum modelling approach for stress analysis at a seismic source: case study. *Rock Mechanics and Rock Engineering*, 49(12), 4749-4765.

Sainoki, A., Schwartzkopff, A. K., Jiang, L., & Mitri, H. S. (2021). Numerical Modeling of Complex Stress State in a Fault Damage Zone and Its Implication on Near-Fault Seismic Activity. *Journal of Geophysical Research: Solid Earth*, 126(7), e2021JB021784.

Scholz, C. H. (1968). The frequency-magnitude relation of microfracturing in rock and its relation to earthquakes. *Bulletin of the seismological society of America*, 58(1), 399-415.

Schorlemmer, D., Wiemer, S., & Wyss, M. (2005). Variations in earthquake-size distribution across different stress regimes. *Nature*, 437(7058), 539-542.

Scognamiglio, L., Magnoni, F., Tinti, E., & Casarotti, E. (2016). Uncertainty estimations for moment tensor inversions: the issue of the 2012 May 20 Emilia earthquake. *Geophysical Journal International*, 206(2), 792-806.

Sellers, E. J., Kataka, M. O., & Linzer, L. M. (2003). Source parameters of acoustic emission events and scaling with mining-induced seismicity. *Journal of Geophysical Research: Solid Earth*, 108(B9).

Shnorhokian, S., Mitri, H. S., & Moreau-Verlaan, L. (2015). Stability assessment of stope sequence scenarios in a diminishing ore pillar. *International Journal of Rock Mechanics and Mining Sciences*, 74, 103-118.

Si, G., Cai, W., Wang, S., & Li, X. (2020). Prediction of Relatively High-Energy Seismic Events Using Spatial–Temporal Parametrisation of Mining-Induced Seismicity. *Rock Mechanics and Rock Engineering*, 53(11), 5111-5132.

Šílený, J., & Milev, A. (2008). Source mechanism of mining induced seismic events—Resolution of double couple and non-double couple models. *Tectonophysics*, 456(1-2), 3-15.

SMITH, R. B., WINKLER, P. L., ANDERSON, J. G. and SCHOLZ, C. H. (1974), Source mechanisms of microearthquakes associated with underground mines in eastern Utah, *Bull. Seism. Soc. Am.* 64, 1295–1317.

Stec, K., & Drzewiecki, J. (2012). Mine tremor focal mechanism: An essential element for recognising the process of mine working destruction. *Acta Geophysica*, 60, 449-471.

Stein, S., & Wysession, M. (2009). *An introduction to seismology, earthquakes, and earth structure*. John Wiley & Sons.

Stierle, E., Vavryčuk, V., Šílený, J., & Bohnhoff, M. (2014). Resolution of non-double-couple components in the seismic moment tensor using regional networks—I: a synthetic case study. *Geophysical Journal International*, 196(3), 1869-1877.

Tape, W., & Tape, C. (2012). A geometric setting for moment tensors. *Geophysical Journal International*, 190(1), 476-498.

Tierney S. (2019). Moment tensors e a practical guide, blog post. Perth, Western Australia: Australian Centre for Geomechanics, The University of Western Australia; 2015. Figure generated by Harris, PH & Wesseloo, J, mXrap software, version 5, <https://mxrap.com/moment-tensors-apractical-guide>. <https://mxrap.com>.

Trifu, C. I., & Urbancic, T. I. (1996). Fracture coalescence as a mechanism for earthquakes: observations based on mining induced microseismicity. *Tectonophysics*, 261(1-3), 193-207.

Urbancic, T. I., & Trifu, C. I. (2000). Recent advances in seismic monitoring technology at Canadian mines. *Journal of Applied Geophysics*, 45(4), 225-237.

Urbancic, T. I., & Trifu, C. L. (1995). Remote triggering of large seismic events in mines: Evidence based on the spatial and temporal migration of microseismic events along increasing stress gradients. In *Earthquakes Induced by Underground Nuclear Explosions* (pp. 353-374). Springer, Berlin, Heidelberg.

Urbancic, T. I., Trifu, C. I., Mercer, R. A., Feustel, A. J., & Alexander, J. A. G. (1996). Automatic time-domain calculation of source parameters for the analysis of induced seismicity. *Bulletin of the Seismological Society of America*, 86(5), 1627-1633.

Urbancic, T., Wuestefeld, A., & Baig, A. (2013). Black box recording of passive seismicity: Pitfalls of not understanding your acquisition instrumentation and its limitations. CSPG Geoconvention. <https://www.esgsolutions.com/sites/esgsolutions.com/files/resource/2013-cseg-black-box-recording-of-passive-seismicity.pdf>.

Utsu, T. (1965). A method for determining the value of b in a formula $\log n = a - bM$ showing the magnitude frequency relation for earthquakes. *Geophys. Bull. Hokkaido Univ.*, 13, 99-103.

Vavryčuk, V. (2015). Moment tensor decompositions revisited. *Journal of Seismology*, 19(1), 231-252.

Vavryčuk, V., & Kühn, D. (2012). Moment tensor inversion of waveforms: a two-step time-frequency approach. *Geophysical Journal International*, 190(3), 1761-1776.

Vennes, I., Mitri, H., Chinnasane, D. R., & Yao, M. (2020). Large-scale destress blasting for seismicity control in hard rock mines: a case study. *International Journal of Mining Science and Technology*, 30(2), 141-149.

Verdecchia, A., Onwuemeka, J., Liu, Y., & Harrington, R. M. (2022). Depth-Dependent Crustal Stress Rotation and Strength Variation in the Charlevoix Seismic Zone (CSZ), Québec, Canada. *Geophysical Research Letters*, 49(22), e2022GL100276.

Wamboldt, L. R. (2012). An automated approach for the determination of the seismic moment tensor in mining environments. Queen's University (Canada).

Wang, B., Harrington, R. M., Liu, Y., Kao, H., & Yu, H. (2020). A study on the largest hydraulic-fracturing-induced earthquake in Canada: Observations and static stress-drop estimation. *Bulletin of the Seismological Society of America*, 110(5), 2283-2294.

Wiemer, S., & Wyss, M. (2000). Minimum magnitude of completeness in earthquake catalogs: Examples from Alaska, the western United States, and Japan. *Bulletin of the Seismological Society of America*, 90(4), 859-869.

Woessner, J., & Wiemer, S. (2005). Assessing the quality of earthquake catalogues: Estimating the magnitude of completeness and its uncertainty. *Bulletin of the Seismological Society of America*, 95(2), 684-698.

Xu, N. W., Dai, F., & Zhou, Z. (2014). Study of characteristics of b value for microseismic events in high rock slope. *Chinese Journal of Rock Mechanics and Engineering*, 33(S1), 3368-3374.

Yang, J., Lu, W., Hu, Y., Chen, M., & Yan, P. (2015). Numerical simulation of rock mass damage evolution during deep-buried tunnel excavation by drill and blast. *Rock Mechanics and Rock Engineering*, 48, 2045-2059.

Yu, H., Liu, Y., Harrington, R. M., & Lamontagne, M. (2016). Seismicity along St. Lawrence Paleorift faults overprinted by a meteorite impact structure in Charlevoix, Québec, Eastern Canada. *Bulletin of the Seismological Society of America*, 106(6), 2663-2673.

Yu, Q., Zhao, D., Xia, Y., Jin, S., Zheng, J., Meng, Q., ... & Zhao, J. (2022). Multivariate early warning method for rockburst monitoring based on microseismic activity characteristics. *Frontiers in Earth Science*, 19.

Zhang, H., Eaton, D. W., Li, G., Liu, Y., & Harrington, R. M. (2016). Discriminating induced seismicity from natural earthquakes using moment tensors and source spectra. *Journal of Geophysical Research: Solid Earth*, 121(2), 972-993.

Zhang, L. (2017). *Engineering Properties of Rocks (Second Edition)*, Pages 137-171, <https://doi.org/10.1016/B978-0-12-802833-9.00005-5>.

Zhou, X. P., Qian, Q. H., & Yang, H. Q. (2011). Rock burst of deep circular tunnels surrounded by weakened rock mass with cracks. *Theoretical and Applied Fracture Mechanics*, 56(2), 79-88.

Appendix A

The information in this section is provided to support the thesis work and provide detailed description of the methodology adopted in Chapter 3.

A.1 Magnitude measures at YD mine

Moment Magnitude (M_w) is used in the database generated from YD mine ESG monitoring system. Nuttli Magnitude (M_n) is used for the data obtained from the Canadian National Seismograph Network (CNSN). YD mine also uses Richter Magnitude (M_R) obtained from the Matachewan-Kirkland Lake Regional Seismic network (RSN) since it has been proven to be a trusted supplement to both networks for monitoring large seismic events. The approximate relations between these magnitudes are as follows (Alamos Gold Inc., 2021).

$$M_N \approx M_R + 0.3 \quad [A-1]$$

$$M_N \approx M_w + 0.5 \sim 0.6 \quad [A-2]$$

$$M_R \approx M_w + 0.2 \sim 0.3 \quad [A-3]$$

A.2 3DVM of Young Davidson mine

The 3D velocity model (3DVM) used for the seismic monitoring system at Young Davidson mine to obtain the seismicity catalog for this study:

Table A-1. 3DVM of Young Davidson Mine (Alamos Gold Inc., 2020).

	Vp (m/s)	Vs (m/s)	Vp/Vs
Host Rock	6057	3501	1.73
Ore	5596	3144	1.78
Diabase	6125	3582	1.71
Stopes / Voids	361	360	1.00

A.3 Seismic moment and seismic energy

Waveform amplitude, frequency, and duration characteristics are used to calculate the source parameters. Thus, the YD mine microseismic system uses equations [2-1] and [2-2] to calculate the seismic energy and seismic moment respectively.

In Section 3.4, the cumulative seismic moment and cumulative energy have been identified monthly through the year 2020 from the seismic database, then the effect of blasting volume on the induced seismicity has been analyzed. Figure A-1 shows an example of the cumulative seismic moment and energy in October 2020 due to blasting volume of about 200,000 tons; refer to Fig 3-7a. The blasting data is provided by the mine.

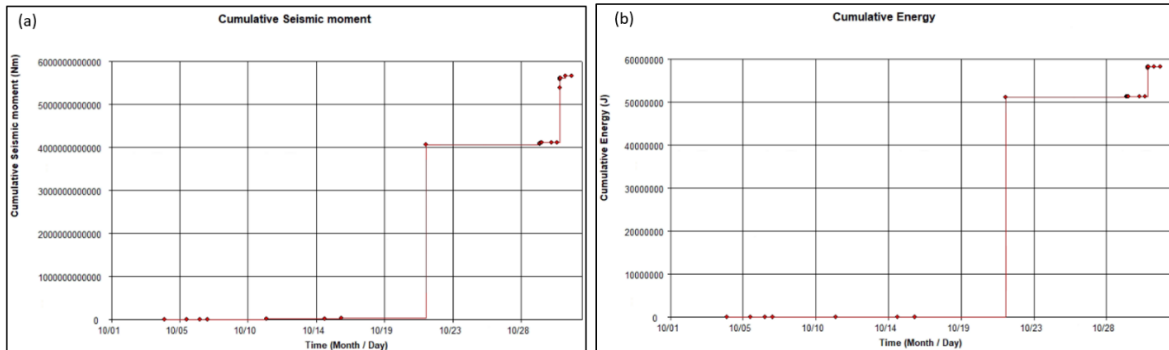


Figure A-1. (a) Accumulated seismic moment and (b) accumulated energy in Oct 2020 at YD mine.

A.4 Analysis of b-value

b-value is calculated from a number of events in the catalog from the seismic monitoring system in YD mine. After each blast has occurred in the depth range 700-900 m (level 9600 to 9400) in 2020, the b-value was obtained from a cluster of induced microseismic events in a two-day window following the blast. Figure A-2 shows an example of how the b-value is estimated for the seismic cluster induced by a blast on Aug 29. Figure A-2 (a) shows a blasting information table according to the mine site and the corresponding b-values. The induced seismic events in a two-day window following the blast of Aug 29 can be seen in Figure A-2 (b). Figure A-2 (d) is the magnitude-frequency chart that represents all the induced events in Figure A-2 (c) which represents the cluster of the events at the location of the blast. The total number of events used to calculate b-value in this example is 211 events. The slope of the red line in the magnitude-frequency chart is b-Value. Also, the seismic system sensitivity is revealed by the resulting graph. The SeisVis graph uses the non-cumulative distribution to determine the peak in the data and define M_{min} (Figure A-3). The magnitude of completeness is considered the minimum magnitude at which 100% of the events are detected (Woessner and Wiemer, 2005). Thus, the magnitudes below this value are not used in b-value calculation. According to ESG Solutions

software manual, the b-value is calculated using Utsu-Aki method (1965); see Equation [2-7]. All the b-values results in this study are obtained following the same procedure. The estimated b-values are analyzed with respect to the blasting distance from the intersecting dykes as discussed in Section 3.5 of the thesis. Table A-2 below shows the number of events induced by each blast and used to estimate each b-value. The number of events run b-value analysis is suggested to be more than 52 according to the manual of ESG software.

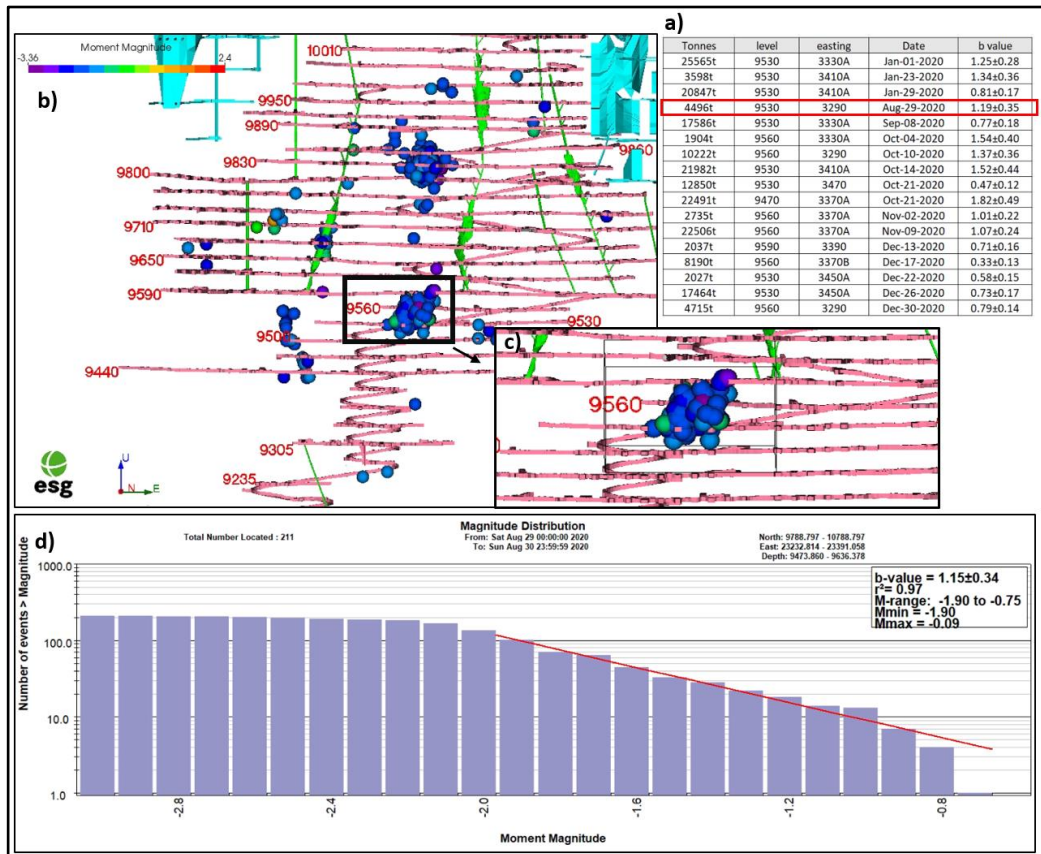


Figure A-2. Example of b-value estimation steps for the seismic cluster induced by a blast on Aug 29, 2020 (a) Blasting information table. (b) The induced seismic events in a two-day window following the blast of Aug 29. (c) Cluster of the microseismic events at the location of the blast. (d) Magnitude distribution graph.

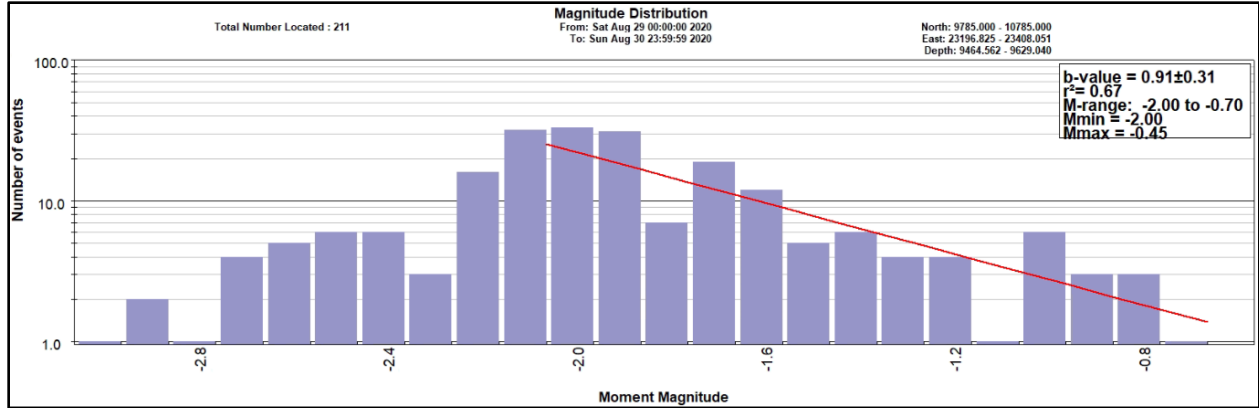


Figure A-3. Frequency distribution with moment magnitude of seismic events at the location of the blast.

Table A-2. Number of events used to estimate b-value after each blast.

Blast event	Number of events for b-value	Blast event	Number of events for b-value
Jan-01-2020	515	Oct-22-2020	301
Jan-23-2020	559	Nov-02-2020	201
Jan-29-2020	540	Nov-09-2020	424
Aug-29-2020	211	Dec-13-2020	59
Sep-08-2020	395	Dec-17-2020	87
Oct-04-2020	374	Dec-22-2020	229
Oct-10-2020	627	Dec-26-2020	343
Oct-14-2020	519	Dec-30-2020	1028
Oct-21-2020	527		

A.5 Moment tensor inversion

In chapter 3, moment tensor inversion is conducted using HybridMT software package developed in MATLAB. According to Kwiatek et al. (2016), the software package takes 1-D velocity model as input. Therefore, in the present study, a 1-D velocity model was used. Considering the limited depth range of the mine case study, it is deemed appropriate to use a constant velocity model. An average value of $V_p = 6020$ m/s was adopted for this study.

The integral of the first P-wave ground-displacement pulse, which is proportional to the seismic moment, is the main program input for each sensor. The first pulse is identified with positive or negative polarity. The acceleration waveform is converted in displacement-time domain as shown in the example of Figure A-4. The area (A) below the first pulse is calculated and reported with

the sign information in the input file. The data of some sensors has been discarded due to low confidence of the polarity.

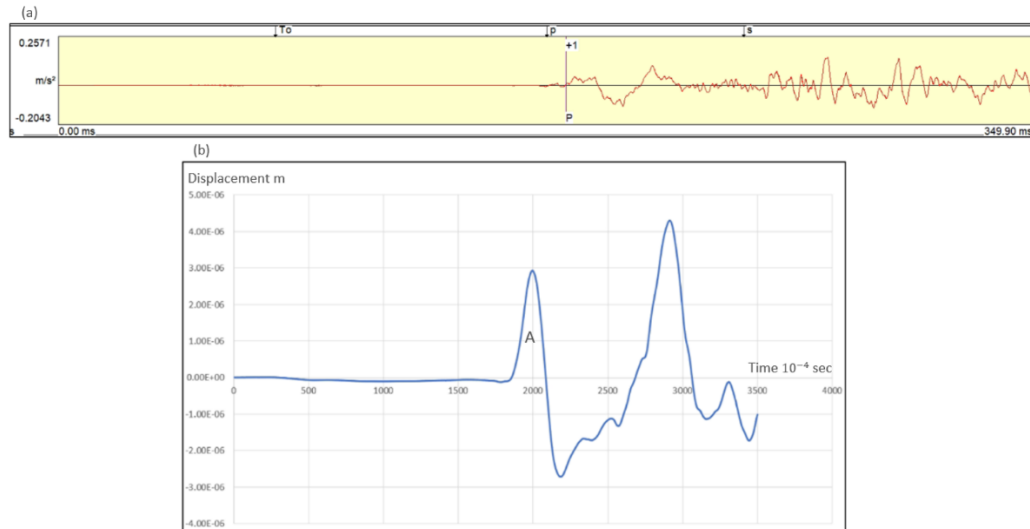


Figure A-4. Example of one waveform for the event Oct 21, 2020, that is converted from acceleration to displacement domain. (a) The waveform in acceleration-time domain. (b) The waveform in displacement time domain.

The input data is provided in a form of ASCII (American Standard Code for Information Interchange) file as required. The top line of each input file is the event line containing information about the seismic event, starting with event ID, number of phases, location of earthquake in local cartesian coordinate system (Northing, Easting, and Z), and the rock density. This event line is followed by several phase lines, corresponding to the number of available stations. Each line reports the station ID, component, phase type, area below the first pulse calculated with sign information, and location of the station in cartesian coordinate system. Then, MT inversion is performed by executing the "focimt" command line using this input file and the 1-D velocity model (Kwiatek et al. 2016). Tables A-3, A-4, and A-5 show the input data used in the MT inversion for the events on Dec 09, Oct 30, and Oct 21 respectively.

Table A-3. The input ASCII file of event Dec 09.

2020120913031213 08 10395 23325.6 -688.3 2773.75						
01	Z P	1.87E-08	10519.5	23406.2	-244.5	
02	Z P	1.01E-08	10500.7	23544.2	-248.3	
08	Z P	2.76E-08	10461.3	23699.8	-402.9	
14	Z P	4.40E-08	10417.0	23587.3	-461	
25	Z P	6.20E-09	10419.9	23700.4	-579.6	
26	Z P	4.93E-08	10477.5	23633.9	-598.3	
27	Z P	3.01E-08	10413.9	23592.8	-616.5	
28	Z P	-7.77E-09	10527.6	23557.0	-617.5	

Table A-4. The input ASCII file of event Oct 30.

2020103013440397 08 10396.7 23286.5 -750.7 2773.75						
01	Z P	1.86E-08	10519.5	23406.2	-244.5	
02	Z P	1.01E-08	10500.7	23544.2	-248.3	
08	Z P	2.78E-08	10461.3	23699.8	-402.9	
14	Z P	4.41E-08	10417.0	23587.3	-461	
25	Z P	-1.02E-08	10419.9	23700.4	-579.6	
26	Z P	4.93E-08	10477.5	23633.9	-598.3	
27	Z P	3.02E-08	10413.9	23592.8	-616.5	
28	Z P	1.35E-08	10527.6	23557.0	-617.5	

Table A-5. The input ASCII file of event Oct 21.

2020102117520776 09 10340.4 23441.4 -784.2 2773.75						
01	Z P	-6.61E-08	10520	23406	-244	
02	Z P	3.65E-08	10501	23544	-248	
08	Z P	3.51E-08	10461	23700	-403	
09	Z P	1.56E-08	10475	23374	-344	
10	Z P	3.67E-08	10482	23351	-443	
14	Z P	6.37E-08	10417	23587	-461	
27	Z P	1.09E-07	10414	23593	-617	
28	Z P	-1.49E-08	10528	23557	-618	
45	Z P	-3.11E-08	10443.1	23321.6	-756.3	